

Prediction of belt conveyor idler performance

Liu, Xiangwei

DOI

[10.4233/uuid:e813298e-93d8-4a76-a7ab-72b327bcde4b](https://doi.org/10.4233/uuid:e813298e-93d8-4a76-a7ab-72b327bcde4b)

Publication date

2016

Document Version

Final published version

Citation (APA)

Liu, X. (2016). *Prediction of belt conveyor idler performance*. [Dissertation (TU Delft), Delft University of Technology]. TRAIL Research School. <https://doi.org/10.4233/uuid:e813298e-93d8-4a76-a7ab-72b327bcde4b>

Important note

To cite this publication, please use the final published version (if applicable). Please check the document version above.

Copyright

Other than for strictly personal use, it is not permitted to download, forward or distribute the text or part of it, without the consent of the author(s) and/or copyright holder(s), unless the work is under an open content license such as Creative Commons.

Takedown policy

Please contact us and provide details if you believe this document breaches copyrights. We will remove access to the work immediately and investigate your claim.

Prediction of Belt Conveyor Idler Performance

Prediction of Belt Conveyor Idler Performance

Proefschrift

ter verkrijging van de graad van doctor
aan de Technische Universiteit Delft,
op gezag van de Rector Magnificus Prof. ir. K.C.A.M. Luyben,
voorzitter van het College voor Promoties,
in het openbaar te verdedigen op maandag 12 september 2016 om 10:00 uur

door

Xiangwei LIU

Master of Science in Mechanical Engineering,
Wuhan University of Technology, Wuhan, P.R. China
geboren te Rizhao, P.R. China.

This dissertation has been approved by the promotor:

Promotor: Prof. dr. ir. G. Lodewijks

Copromotor: Dr. ir. Y. Pang

Composition of the doctoral committee:

Rector Magnificus,	chairperson
Prof. dr. ir. G. Lodewijks,	Delft University of Technology, promotor
Dr. ir. Y. Pang,	Delft University of Technology, copromotor

independent members:

Prof. W. Li	Wuhan University of Technology (P.R. China)
Prof. Dr. -Ing. A. Katterfeld	Otto von Guericke Universität Magdeburg (Germany)
Dr. M. Cincera	Rulmeca Holding S.p.A (Italy)
Prof. ir. J.J. Hopman	Delft University of Technology
Prof. dr. R. Curran	Delft University of Technology

dependent member:

Dr. C. Wheeler,	The University of Newcastle (Australia)
-----------------	---

The research described in this dissertation is fully supported by the Chinese Scholarship Council under grant 201206950027, Delft University of Technology, and partially supported by Rulmeca Holding S.p.A, Rizhao Port Group Co., Ltd, and Rizhao Changyun Industry Transport Equipment Co., Ltd.

TRAIL Thesis Series T2016/14, the Netherlands TRAIL Research School

P.O. Box 5017

2600 GA Delft, the Netherlands

Phone: +31 (0) 15 278 6046

Email: info@rstrail.nl

Keywords: bulk material, belt conveyor, idler, reliability, condition monitoring, maintenance

Printed and distributed by: Xiangwei Liu

Email: xiangweiliu@yahoo.com

Copyright © 2016 by Xiangwei Liu

All rights reserved. No part of the material protected by this copyright notice may be reproduced or utilized in any form or by any means, electronic or mechanical, including photocopying, recording or by any information storage and retrieval system, without written permission of the author.

ISBN 978-90-5584-207-0

Printed in the Netherlands

To my mother

ACKNOWLEDGEMENTS

The pursuit of my doctorate at Delft University of Technology in the Netherlands during the past four years was an amazing journey. Many people provided me support, to whom I want to express my deep gratefulness.

Above all, I sincerely appreciate the Chinese Scholarship Council to provide the funding to support my Ph.D research.

Secondly, I would like to give my great gratitude to my promoters Prof. Gabriel Lodewijks and Dr. Yusong Pang. Gabriel, I would like to thank you for your availability, inspiring discussions, critical comments, and your effort to improve my manuscript. Particularly, I would like to thank you for applying 3mE faculty funding to support my experimental research. To Yusong, thank you for your enlightening guidance, patient supervision, and the effort to train my research skills. Specially, your half Chinese half Dutch supervision style gave me both intense support and independence. I have learned a lot from you two about both research and life.

Furthermore, my sincere thank goes to the people who provided support for my work. To Craig Wheeler, thank you for providing me the opportunity to conduct experiments at The University of Newcastle, Australia. It was great experience in Newcastle. To Marco Cincera from Rulmeca Holding S.p.A, thank you for supporting my experimental research as well as the informative discussions. To Wenjun Zhang, thank you for giving me the opportunity to conduct tests at Rizhao Port Group Co., Ltd. I would also like to thank Rizhao Changyun Industry Transport Equipment Co., Ltd for providing me tests. Within M&TT Department, I sincerely thank Jozephina, Patty, Dineke, Ed Stok and Freek for their excellent support to me. A particularly big thank to Dick Mensch for proof checking of the manuscript and mathematical help in my research. To all my colleagues in TEL Section, thank you for inspiring discussions about work. Special thank goes to Maria Zamiralova, Alireza Alemi and Daijie He for sharing their research knowledge with me. I would also like to thank master students Kristel Thieme, Emiel van Bodegom, and Vincent Sikkes for their contribution to this research. It was great experience to work in TEL Section.

In addition, I would like to thank my friends in Delft for their sharing and encouraging. To the communities of ISC Delft, Jessehof, 3mE PhD Council and Rock'n Delft, it was my pleasure to be involved. The Chinese folks in TEL Section helped me a lot in my daily life. My thank also goes to Giorgio Faedo, Clarrisse Wu, Adri Ana, Gonzalo Duro, Alida Alves, Jiaxiu Cai, Patri Guerrero, Mari Posa, Diego Riste, and Ruben Abellon. To Jie Mei, thank you for sharing research experience and encouraging me to complete

my PhD on time. To Henk van der Vaart, I cannot thank you more for your family-like guidance, understanding, wisdom, and those Sunday lectures. To Maria Clemens, I deeply appreciate your encouragement and support to my work, particularly the help with graphics and proof checking of this dissertation.

In the end, I also would like to thank my friends and family in China. I know your support is always there for me. My deepest appreciation to my parents, they educate me into who I am, and they sacrifice themselves to give me the freedom of choice.

I really enjoyed my PhD career in Delft.

Xiangwei Liu

Halle(Saale), 2016.07.28

CONTENTS

1	Introduction	1
1.1	Aim of the research.	4
1.2	Research methodology	5
1.3	Outline of the thesis	6
2	Idler performance	9
2.1	Reliability of belt conveyors	9
2.2	Belt conveyor components	10
2.2.1	The belt	11
2.2.2	The pulleys.	13
2.2.3	The drive unit	13
2.2.4	The idlers	14
2.3	Idler selection	15
2.3.1	Idler selection criteria	15
2.3.2	Idler selection procedures.	17
2.4	Idler roll failure analysis	19
2.5	Prediction of idler roll failures	23
2.6	Summary.	25
3	Stress discontinuity model for bulk load determination	27
3.1	Derivation of the roll load	27
3.2	Related earth pressure theories	30
3.2.1	Coulomb's earth pressure theory	30
3.2.2	Rankine's earth pressure theory.	32
3.2.3	Sokolovski's stress discontinuity method	34
3.3	Review on bulk and belt models	36
3.3.1	Models for the bulk load	37
3.3.2	Model for the belt load	40
3.3.3	Coupled model for the bulk and belt load	42
3.4	Development of the SD model	44
3.4.1	Dynamic movement of bulk materials.	44
3.4.2	Active stress state analysis	45
3.4.3	Passive stress state analysis	49
3.4.4	Derivation of the bulk load	50

3.5	Comparisons with the KH model	50
3.6	The roll bearing load	59
3.7	Conclusions	61
4	Experimental determination of bulk load	63
4.1	Background	63
4.2	Experimental setup	65
4.2.1	Belt conveyor facility	65
4.2.2	Tekscan measurement system	66
4.2.3	Independent instruments	67
4.3	Experimental procedures	67
4.4	Results and discussion	67
4.4.1	Re-arrangement of preliminary results	68
4.4.2	Post-process scheme	71
4.4.3	Comparisons of experimental and theoretical results	78
4.5	Conclusions	83
5	Experimental condition monitoring of idler rolls	85
5.1	Condition monitoring of the idlers	85
5.1.1	Human sensory inspection and interpretation	86
5.1.2	Sensor assisted inspection and human interpretation	86
5.1.3	Automated inspection and interpretation	87
5.2	Laboratory idler experiments	90
5.2.1	Design of the test rig	90
5.2.2	Inducement of bearing defects and damages	90
5.2.3	Sensor selection	91
5.2.4	Sensor installation	95
5.2.5	Experimental procedures	96
5.2.6	Results and discussion	97
5.3	In-situ idler experiments	113
5.3.1	Experimental setup	113
5.3.2	Results and discussion	116
5.4	Conclusions	118
6	Integrated maintenance decision making	121
6.1	Introduction	121
6.2	Framework of integrated maintenance decision making	123
6.3	Case study	127
6.4	Conclusions	131
7	Conclusions and recommendations	133
7.1	Conclusions	133
7.2	Recommendations	135
	Bibliography	137
	Appendix	149
	Glossary	165
	Summary	169

Samenvatting	171
Curriculum Vitae	173

1

INTRODUCTION

Belt conveyor systems are widely utilized for continuous transport of dry bulk materials (i.e. coal, iron ore) over varying distances. A vast variety of industries like the mining, power sector, cement production, and bulk terminals (Figure 1.1) rely on the performance of belt conveyor systems. Compared with other bulk haulage modes like the trucking and railway, belt conveyor systems provide many advantages such as a higher capacity, lower cost, higher efficiency, less human involvement and proven reliability (Roberts, 1981; Smith and Spriggs, 1981). Along with the growing international trade in major bulk materials, there is an increasing demand for the transportation of bulk materials. Correspondingly, large-scale belt conveyor systems have been installed to meet the demand for higher capacity and longer distance application of continuous conveying of bulk materials (Harrison and Roberts, 1983; Lodewijks, 2011).



Figure 1.1: Part of a 1.5 km long belt conveyor system on a bulk terminal, figure courtesy of Rizhao Port Group Co., Ltd.

The reliability of belt conveyor systems is of major concern for the operators. High reliability of belt conveyor systems ensures the availability of the systems to achieve high

productivity of transportation of bulk materials. On contrary, breakdowns of belt conveyor systems result in downtime of the systems. The downtime of belt conveyor systems leads to stoppage of transportation of bulk materials, influencing subsequent material processing and production, and consequently causes serious financial loss. In a mining plant, for example, sixty percent of the plant downtime was attributed to conveyor problems (Steinberg, 1983). The downtime cost of belt conveyor systems may vary from one application to another. The financial loss due to the downtime of belt conveyor systems can be in a range of 100,000 to 200,000 Euro per hour, considering the loss of the revenue from material conveying, and shutdowns of subsequent material processing facilities (Lodewijks, 2015).

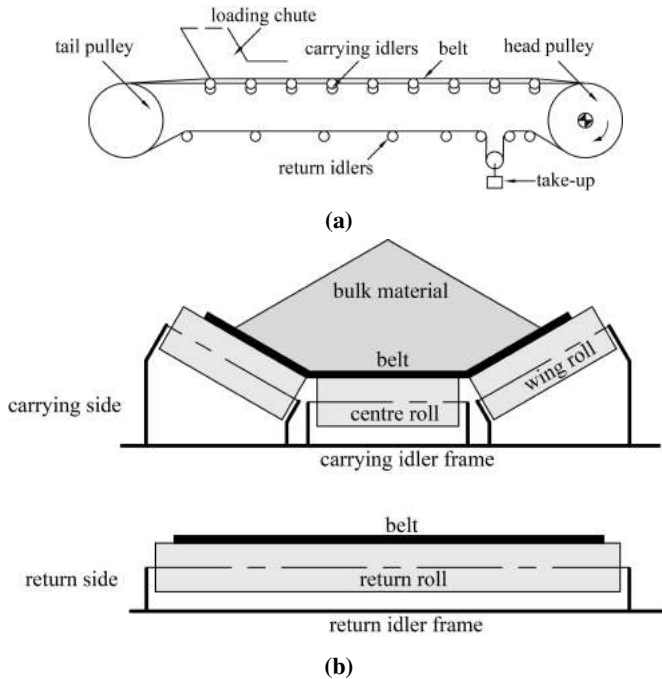


Figure 1.2: Schematic layout of a belt conveyor system, (a) overview of all conveyor components and (b) cross section of idler stations.

Figure 1.2 (a) illustrates a schematic layout of a belt conveyor system. A belt is spanned between a head pulley and a tail pulley. The head pulley is connected to a drive unit, which consists of an electric motor, multiple couplings, and a gearbox. Bulk material is loaded on the belt through a loading chute, and is conveyed forward along with the movement of the belt over spatially distributed carrying idlers. A conventional trough carrying idler consists of two wing rolls and one center roll which are installed on a rigid frame [Figure 1.2 (b)]. A return idler consists of one or two rolls, or three rolls when going through a curve. Each idler roll consists of a shell, a shaft, two bearings, two bearing houses, and two sealing systems (Figure 1.3). A take-up subsystem is used to apply pre-tension on the belt.

The reliability of a belt conveyor system can be considered as the integrated reliability

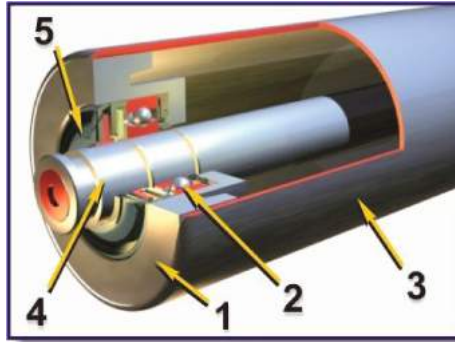


Figure 1.3: Anatomy of an idler roll, derived from CKIT (2012).

Note: 1 refers to the bearing house, 2 is the bearing, 3 is the shell, 4 refers to the shaft, and 5 represents the sealing system.

of all components. Unplanned downtime of a belt conveyor system is generally caused by the belt or rotating components such as the pulleys, idlers and drive unit (Zimroz and Krol, 2009). The malfunction of one of these components may lead to a shutdown of the whole conveyor system in order to carry out maintenance activities like repairing or replacing failed components. For example, failed idler rolls (Figure 1.4) can damage conveyor belts seriously, and consequently add downtime and maintenance cost for belt conveyor systems (Lodewijks, 2003).



Figure 1.4: A typical failed idler roll, figure courtesy of Rizhao Port Group Co., Ltd.

A direct way to increase the reliability of belt conveyor systems is to improve the reliability of the components (Pang, 2010). In literature on reliability engineering concerned with belt conveyor systems, the focus of research on the component level is on the belt, pulleys and drive units. Condition monitoring is considered as an effective manner to improve the reliability of the components (Pang and Lodewijks, 2012). With the development of sensing technologies, most belt conveyor components except idlers can be monitored online (Pang and Lodewijks, 2011). Design, engineering, monitoring and maintenance of conveyor belts have been investigated in order to improve the performance

(i.e. Harrison and Roberts, 1983; Pang, 2010). In addition, research on how to improve the design and effective condition monitoring of pulleys has been carried out (i.e. King, 1983; Zimroz and Bartelmus, 2012). The diagnosis on the condition of drive units, especially the gearboxes, is also a focus (i.e. Bartelmus, 2003).

However, to increase the reliability of belt conveyor systems with respect to idlers is underdeveloped. The performance of the idlers has a large impact on the reliable operation of belt conveyor systems (Bartelmus and Sawicki, 2000; Geesmann et al., 2009a). Nevertheless, belt conveyor idlers lack the due attention from researchers and operators (Relcks, 2008). So far idler rolls are the most difficult to be monitored in automated ways due to their large amount (up to 20,000 rolls for a 10 km long belt conveyor system), the scale of monitoring systems and the spatial distribution of rolls (Pang and Lodewijks, 2011). Meanwhile, idler rolls are often neglected because they are relatively simple and cheap compared to other components (i.e. the belt and pulleys) of a belt conveyor system. This circumstance may be true for belt conveyor systems of short distance. However, idler rolls in large-scale belt conveyor systems are important considering the large initial purchasing investment, high operating and maintenance cost, and the costly consequences of idler roll failures. In fact, many operators suffer from damages and breakdowns of belt conveyor systems caused by idler roll failures (Tuckey et al., 1985).

1.1 Aim of the research

The main research question of this project is:

How to improve the reliability of belt conveyor systems?

For the sake of high productivity in transportation of bulk materials with low cost, high reliability of belt conveyor systems is required. Low reliability of belt conveyor systems leads to insufficient utilization and serious financial loss in forms of added downtime, loss of revenues from the conveyance of bulk materials, and high maintenance cost. To achieve high reliability of belt conveyor systems, a direct way is to ensure the reliable operation of all components. Among the conveyor components, the reliability of the belt, drive units and pulleys has been researched while the idlers are neglected. This research focuses on how to improve the reliability of belt conveyor systems with respect to the idlers. Since the condition of idler rolls decreases with aging and accumulated wear, predictive maintenance is required in order to ensure the reliable performance of belt conveyor idlers. Therefore, four sub research questions need to be examined:

1. How to predict idler roll failures?

In order to improve the reliability of belt conveyor systems with respect to the idlers, it is necessary to predict idler roll failures. Prediction and detection of idler roll failures allow programmed maintenance, and preventing a small failure from turning into a large catastrophe (Owen, 1997). The prediction of idler roll failures is important for planning maintenance activities (i.e. inspections and replacements) in time, and for ensuring the reliable operation of idlers and belt conveyor systems.

There are three potential approaches to predict idler roll failures, theoretical calculation of the reliability of idler rolls based on their operational conditions (i.e. the load and

rotational speed), detection of idler roll failures based on condition monitoring data, as well as integrated maintenance decision making based on the two previous approaches.

2. How to calculate the reliability of idler rolls?

Theoretical calculation of the reliability or lifetime of idler rolls is important for the long term planning of maintenance activities. One characteristic of idler rolls in a belt conveyor system is the large amount of identical units. Since most idler rolls (except the idler rolls in special sections like curved trajectories) are under same operational conditions, they are supposed to have same reliability characteristics. By calculating the reliability of idler rolls, conveyor operators can obtain an adequate prediction of the failure rate of idler rolls within a belt conveyor system. With the prediction of failure rate, maintenance activities like periodic inspections and idler replacements can be planned accordingly. For example, a long inspection interval can be planned if prediction of a low failure rate of idler rolls exists and vice versa.

3. How to detect idler roll failures?

The detection of idler roll failures is critical for the decision making on replacements of idler rolls. Though the idler rolls are assumed to be identical and under the same operational conditions in theoretical calculation of reliability, failure occurs randomly to individual roll due to unpreventable differences in the design, fabrication, installation and operation. For instance, difference in the quality of roll bearings may lead to large variation in the lifetime of idler rolls within a belt conveyor system. As a result, idler roll failures have to be detected on individual roll level based on condition monitoring data.

4. Is it possible to achieve integrated decision making on idler maintenance?

Decisions on the idler maintenance mainly include diagnoses on idler roll failures and determination of inspection intervals. Theoretical calculation of the reliability or lifetime generally provides prediction on the failure rate of idler rolls with a certain discrepancy from the reality. On the other hand, inaccuracy also exists in detection of failures based on condition monitoring data. Consequently, it can be a challenge to achieve accurate maintenance decisions merely based on one of the two approaches. Therefore, it is desirable to develop an approach which combines the information from both the theoretical calculation and condition monitoring approaches.

1.2 Research methodology

Both theoretical and experimental research methodologies will be applied in this research. The prediction of idler roll failures is important to maintain the reliable operation of idlers. The prediction of idler roll failures may be achieved by the theoretical calculation approach, the condition monitoring approach, and the integrated approach. The capability of these three approaches will be improved.

In order to improve the accuracy of theoretical calculation of the reliability of idler rolls, research will focus on deriving the load on idler roll bearings. The proper running of idler rolls is largely dependent on the functioning of bearings (Rozentals and Msaime,

1981; Lodewijks, 2003; Wheeler and Ausling, 2007). As a result, theoretical calculation of the reliability of idler rolls can be achieved by calculation of the reliability of roll bearings. The bearing lifetime theory from Lundberg and Palmgren (1949) will be employed in this research. According to the bearing lifetime theory, the load on roll bearings is critical information for the calculation with a given rotating speed of the bearings (and hence the belt velocity). Krause and Hettler (1974) developed the only well-known theoretical model to calculate the load on idler rolls. However, their approach is considered to overestimate the load on wing rolls while underestimating the load on center rolls (Wheeler, 2003a). Therefore, the focus of this theoretical research is on how to develop a more accurate model to determine the load on idler rolls and further roll bearings. With more accurate determination of the load on roll bearings, the capability of the theoretical approach can be improved.

To derive the load on idler rolls, an analytical approach from soil mechanics will be applied to determine the pressure on conveyor belts exerted by bulk materials. Experimental study will be carried out to measure the pressure on a loaded conveyor belt.

Experimental study will be carried out on both laboratory and in-situ belt conveyors to investigate which monitoring parameters (temperature, vibration and acoustic emission) are suitable for the detection of idler roll failures. Though solutions for the condition monitoring of idler rolls are under development, the choice of monitoring parameters is still arbitrary. For the laboratory experiments, idler rolls with various defects and damages are prepared to simulate idler roll failures. In-situ experiments will be carried out on a terminal conveyor. With applicable monitoring parameters, the detectability of idler roll failures can be improved.

1.3 Outline of the thesis

The outline of the thesis is shown in Figure 1.5.

Chapter 2 introduces basic knowledge on the reliability of belt conveyors and the performance of idlers. Particularly, the reasons for idler roll failures and the consequences are discussed.

Chapter 3 focuses on deriving the load on idler roll bearings. For the theoretical calculation of the reliability of idler rolls, bearing lifetime theories are available. However, the method to determine the load on roll bearings is underdeveloped.

Chapter 4 presents an experimental study on the measurements of the pressure on a running conveyor belt caused by bulk materials.

Chapter 5 introduces an experimental study on the condition monitoring of idler rolls in both laboratory and in-situ environment. Temperature, vibration and acoustic sensors are applied in the experiment.

Chapter 6 presents a framework for the decision making of idler maintenance. The framework integrates both theoretical calculation of the failure rate of idler rolls and the information from condition monitoring data.

Chapter 7 gives conclusions and recommendations.

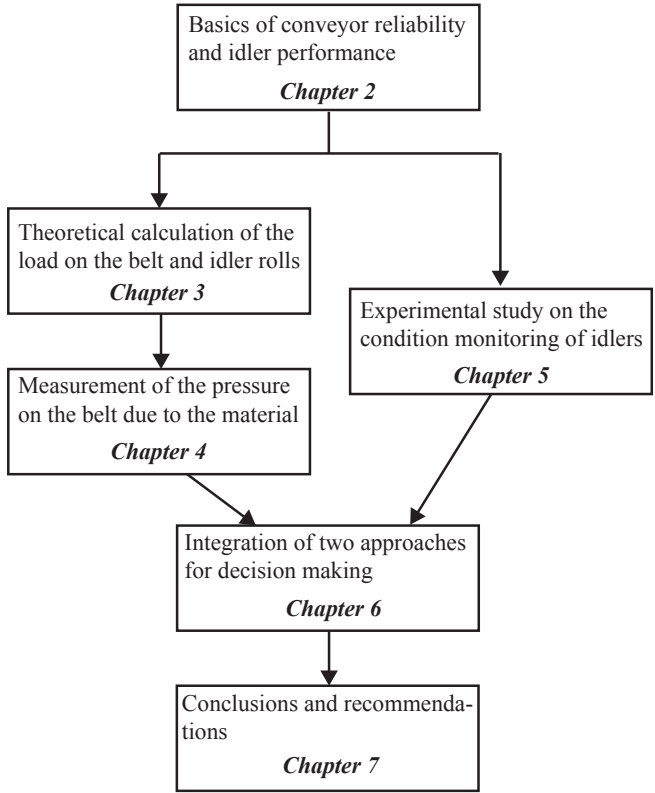


Figure 1.5: Thesis outline.

2

IDLER PERFORMANCE

The reliable performance of belt conveyors is critical to ensure uninterrupted transport of dry bulk materials. This chapter discusses the reliability of belt conveyors. Section 2.1 introduces the reliability of belt conveyor systems at different levels. Section 2.2 reviews research on improving the reliability of belt conveyor components. Section 2.3 presents the criteria and procedures for the selection of idlers. Prediction of the performance of belt conveyor idlers requires the analysis of idler roll failures. Section 2.4 discusses the reasons for idler roll failures and the consequences. Section 2.5 proposes the methodology that will be used for the rest of the thesis. Section 2.6 summarizes this chapter.

2.1 Reliability of belt conveyors

The reliability of a belt conveyor can be defined as the percentage of operational time the conveyor's continuous performance is guaranteed (Lodewijks and Ottjes, 2005a). The reliability of a belt conveyor represents the level of availability for the conveyor as a whole equipment for the transport of bulk materials within a certain period of operational time.

The reliability of a belt conveyor determines the design capacity of the conveyor. To design a new belt conveyor, information such as the total amount of bulk materials to be conveyed, the available time for operation, and a presumed reliability of the belt conveyor is required. With this information, the design capacity of the conveyor can be derived as the total amount of bulk materials divided by the product of the available operational time and the presumed reliability.

The design capacity of a belt conveyor on the other hand is a key determinant for the capital and operational costs. Belt conveyors are capital intensive equipment. Worldwide approximate \$600 million USD annually is spent on new installation and replacement of belt conveyors (Nordell, 2003). A higher design capacity necessitates higher belt speed and/or wider conveyor belts. Each option will raise the cost. For example, utilization of a wider belt will raise the annual equivalent cost of the system (Roberts and Harrison, 1987) due to the investment of larger conveyor infrastructure and components like idlers, pulleys and drive units. A higher belt speed results in larger power consumption of a conveyor

(Paul and Shortt, 2007). Therefore, the presumed reliability of belt conveyors is strongly related to the cost of bulk material conveying. With a higher reliability, a lower design capacity can be achieved and therefore lower cost for belt conveying can be realized.

The reliability of belt conveyors can be considered at three aggregation levels: the system, the equipment and the component level (Lodewijks and Ottjes, 2005b). The system reliability represents the overall operational performance of a belt conveyor system which consists of multiple conveyors and transfer stations. The reliability at the equipment level considers the performance of a single belt conveyor. At the component level, different conveyor components have their own reliability due to condition changing and degradation. In this thesis, the reliability of belt conveyors will be discussed at the equipment and component levels.

The equipment reliability of a belt conveyor can be obtained from the reliability of its components. In this study four conveyor components are included: the belt, drive unit, pulleys, and idlers. From general reliability engineering, an equation to calculate the equipment reliability R for a series of independent components (O'Connor, 1991) is:

$$R = \prod_{i=1}^n R_i \quad (2.1)$$

where R_i is the reliability of the i th component.

With given reliability of different components, the equipment reliability of a belt conveyor can be obtained by applying Eq. (2.1). As a result, the equipment reliability of a belt conveyor can be expressed by a reliability number (Lodewijks and Ottjes, 2005b).

Research on improving the reliability of belt conveyors at the equipment level has been carried out. The development of integrated monitoring of major conveyor components contributes significantly to the reliability control of belt conveyors (Pang and Lodewijks, 2013). Reliability control refers to the process to maintain the reliability of a belt conveyor at a certain level. For example, the Intelligent Belt Conveyor Monitoring and Control system was developed (Pang, 2010), by which the interrelationship among monitored components can be investigated so that maintenance and operational strategies can be chosen to maintain a high level of equipment reliability. Considering the spatial distribution (i.e. data acquisition from highly distributed sensors) and the functional distribution (i.e. different sensors for the condition monitoring of one component) that are required for the integration at the equipment level, Pang and Lodewijks (2012) proposed a multi-agent architecture (Figure 2.1) for the Intelligent Belt Conveyor Monitoring and Control system. Under the multi-agent architecture, agents that monitor and diagnose individual component are organized into cooperative communities to achieve optimum reliability control of a belt conveyor.

Improving the reliability of belt conveyor components is a direct way to increase the equipment reliability of belt conveyors. Continuous monitoring is considered as an effective manner to improve the reliability of conveyor components (Pang and Lodewijks, 2012). Therefore, condition monitoring of belt conveyor components has gain much attention in recent years.

2.2 Belt conveyor components

Belt conveyor components need to be monitored in order to understand their actual status. With condition monitoring, potential failures can be detected or predicted in advance, and

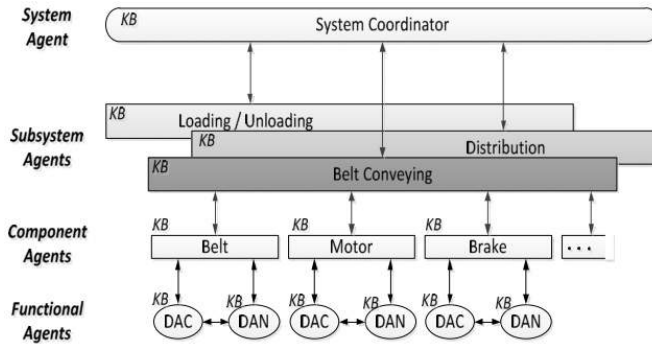


Figure 2.1: Multi-agent architecture, derived from Pang and Lodewijks (2012).

Note: KB represents knowledge base, DAC represents data acquisition, and DAN represents data analysis.

corrective actions can be carried out to ensure the reliability of conveyor components. Advances in sensing technologies have fueled the development of condition monitoring of components within a belt conveyor.

2.2.1 The belt

Monitoring technologies have been developed to detect or even predict damages to conveyor belts. Considering the actual status of a conveyor belt, three conditions are of concern for condition monitoring: the health of carcasses, the condition of belt splices, and the wear of belt covers. In principle, conveyor belt monitoring technologies can be categorized into non-embedded belt monitoring and embedded belt monitoring.

The non-embedded belt monitoring commonly applies magnetic, X-ray, or machine vision technologies. Harrison (1984) developed a conveyor belt monitoring system based on a magnetic technology. In the system, a magnetic circuit is formed between a transducer and a receiver via steel carcasses in a belt. The difference between the input voltage at the transducer and the output voltage at the receiver reflects condition change of a belt including the vertical displacement of steel cords, corrosion and belt wear (Harrison and Brown, 1986). The limitation of the system is that it can only be applied to steel cord reinforced belts. Alport et al. (2001) investigated the utilization of video cameras for the condition monitoring of conveyor belts. Considering the large amount of images produced by a camera during each inspection, Artificial Neural Networks methods are applied to improve the efficiency and accuracy of image processing. The advantage of the system is its easiness to install and operate. A drawback can be that residual of sticky materials on belt covers may give false indication of damages. Besides that, visual images only provide limited indication of the condition of internal carcasses and splices. The application of X-ray technology is also reported (Fourie et al., 2005). The monitoring of belt condition is achieved by using a low energy digital X-ray camera to scan a belt. The images produced by such a X-ray camera can reveal potential damages of a belt for instance a damage of the splice (Figure 2.2). However, the X-ray images may be difficult and time consuming to interpret because of the poor image quality derived from harsh environment surrounding a belt conveyor. In addition, safety may also be a concern when applying X-ray technology.

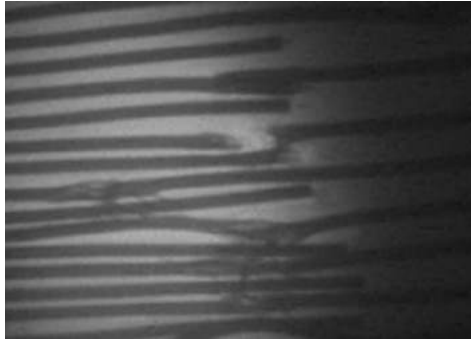


Figure 2.2: X-ray image of damaged splice of a belt, figure courtesy of Conveyor Expert B.V.

Condition monitoring of conveyor belts can also be achieved by applying embedded conductors in conveyor belts (Figure 2.3). In a patent, two conductors are embedded in a belt to monitor belt splices (Alles and Wach, 2000). The monitoring is realized by continuously measuring the distance between the two conductors. An increase of the distance potentially indicates increased belt tension or damage of splices. In another patented technology, microcoil springwire is applied as conductors (Gartland, 2002). Potential belt rips can be detected by external detectors as the break of microcoil springwire. Springwire is chosen because it can resist self-damage due to normal belt vibrating. A matrix of Hall effect magnetic sensors is also proposed to be embedded in conveyor belts to measure main operating parameters such as the identity, speed, wear, and belt tension (Pang, 2010). A common limitation for the category of embedded belt monitoring technology is that it is contemporarily difficult to manufacture conveyor belts with embedded conductors due to the high temperature during belt manufacturing and the low adhesion between a belt and embedded sensors (Pang and Lodewijks, 2011).

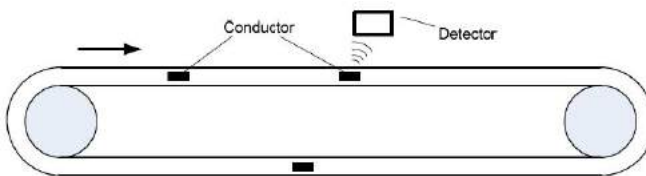


Figure 2.3: Principle of embedded belt monitoring, derived from Pang (2010).

Prediction of belt damages enhances the reliability of conveyor belts. With continuous monitoring of conveyor belts, diagnosis and even prognosis on the condition of conveyor belts can be achieved by using for instance Fuzzy Logic (Lodewijks and Ottjes, 2005b). Corrective actions (i.e. reparation and replacement) can be programmed to prevent a small belt damage from developing into a severe one. In this way, the reliability of conveyor belts can be maintained.

2.2.2 The pulleys

The pulleys of most belt conveyors can be monitored (Pang, 2010). A main focus of the monitoring of pulleys is to detect failures of pulley bearings (Fauerbach, 1993). Pulley bearing failures cause considerable downtime and cost for reparation or replacement.

There are a limited number of studies on the condition monitoring of bearings in pulleys. Temperature and vibration are two common parameters of monitoring. As most pulleys are large in scale, there is sufficient space to install sensors permanently. Contact (i.e. thermocouples) and non-contact (i.e. infrared sensors) temperature sensors can be applied to measure the temperature of pulley bearings. In general, temperature based diagnosis on the condition of pulley bearings is to assess whether the measured temperature exceeds a presumed threshold value. For example, Owen (1997) considers that a bearing failure may occur if the measured temperature of a bearing exceeds 90 °C.

However, the temperature based diagnosis on the condition of pulley bearings is not accurate. For one reason, it is a challenge to obtain a proper threshold value which can distinguish failures of pulley bearings. Even for same bearings, the threshold may vary considerably under different operational conditions and application environment (Sawicki et al., 2015). For another reason, temperature measurements of bearings may fluctuate due to external disturbances (i.e. temporary overloading). The fluctuation can lead to false alarms if measured temperatures exceed the threshold value. To overcome these limitations, Sawicki et al. (2015) proposed a framework to process acquired data. The proposed data processing consists of several steps including outliers removing, re-sampling, segmentation, decomposition, and de-trending. After processing, diagnostic information can be retrieved from the low frequency trend signals. With data processing, more reliable diagnosis on the condition of bearings is supposed to be achieved compared to the conventional approach without data processing.

Compared to temperature measurement, vibration measurement requires more sophisticated analysis. Excessive vibration detected by accelerometers can provide early indication of pulley bearing failures (Owen, 1997). Recent progress in signal processing and analysis such as adaptive filtering (Zimroz and Bartelmus, 2012) enables the extraction of rich information from the signal acquired by accelerometers. Information like the Kurtosis, RMS level, frequencies and their corresponding energy of vibration may be applied as diagnostic bases.

Most pulleys are located at either end of a belt conveyor, so it is relatively easy to collect and transfer condition monitoring data to the central control room. In addition, continuous monitoring of every pulley is feasible considering the limited cost to develop a monitoring system compared to the considerable cost due to potential pulley failures. Robust diagnosis on the condition of pulleys therefore improves the reliability of pulleys by providing information for planning maintenance activities in advance.

2.2.3 The drive unit

Research on improving the reliability of drive units has received considerable attention. The drive unit plays a key role in the continuous operation of a belt conveyor. Drive units are very sensitive to system degradation, contamination and overloading operations (Hills, 2009). Within a drive unit, the gearbox is a critical rotating motion transmission component. Therefore, improving the reliability of gearboxes by using condition monitoring has been a focus (Chaari et al., 2012). Vibration measurement is a common approach for the condition monitoring of gearboxes. The vibration signal requires further process-

ing before being used for the diagnosis. Model based diagnosis has been introduced into the diagnoses of gearboxes. The approach is based on comparisons between the measured vibration signal and a priori of vibration characteristic in form of a mathematical model (Chen and Patton, 1999). Diagnosis can be achieved through generating residual quantities when the mathematical model tries to match measurement results. For example, Bartelmus (2001, 2003) proposed diagnoses of one- and two-stage gearboxes based on dynamic modeling of gearboxes and vibration signal. However, it can be difficult to verify such a mathematical model with the actual condition of the modeled system.

Besides vibration, measurements of other electromechanical parameters (i.e. acoustic emission, torque on shafts, current and voltage of motors) are also applied. For example, Hills (2009) reported the application of measurements of the current of motors for the continuous monitoring of drive units within belt conveyors. But no sufficient information is provided in the study. Jeinsch et al. (2002) also successfully detected a seeded fault of a drive unit by using the model based diagnosis through measurements of driving torque and belt speed. With the effort for development of continuous monitoring of drive units, the reliability of drive units is generally ensured.

2.2.4 The idlers

While most conveyor components are monitored continuously to maintain their reliability, idler rolls remain a challenge to be monitored (Pang and Lodewijks, 2011). Though the idlers, pulleys and gearboxes are categorized as rotating elements within a belt conveyor, the differences among them make it challenging to apply same condition monitoring solutions. Firstly, the sizes and locations of pulleys and gearboxes enable easy installation of permanent sensors (Hills, 2009). On contrary, very limited space is available on an idler roll for the installation of monitoring sensors (Liu et al., 2014a). Secondly, successful applications of vibration, acoustic emission and temperature based condition monitoring for pulleys and gearboxes have been reported as mentioned in previous subsections, the applicability of these monitoring parameters for the idler roll monitoring remains dubious. Thirdly, it is feasible to monitor every pulley and gearbox because of their limited amount within a belt conveyor. Considering the large amount and highly distribution of idler rolls, however, a question rises whether it is cost effective to install sensor(s) on each roll.

Conventionally, idler rolls are inspected by maintenance personnel in human sensory manners (eye watching and ear listening). Such inspection can lead to inconsistent and unreliable diagnosis on the condition of idler rolls (Lodewijks and Ottjes, 2005b). Recent development in the monitoring of idler rolls provides automated mobile monitoring systems and automated fixed monitoring systems. Automated mobile monitoring systems follow the concept of intelligent maintenance of idlers proposed by Lodewijks (2003), in which the inspection of idler rolls can be carried out by robot manipulators installed on a trolley. Meanwhile, automated fixed monitoring systems are developed with ideas of installing sensors permanently into every idler roll. Sensors will collect data automatically and periodically. A detailed review on the development of condition monitoring of idler rolls can be found in Section 5.1.

2.3 Idler selection

The structure of an idler as well as the anatomy of a roll has been briefly introduced in Chapter 1 (Figure 1.2 and 1.3). Steel is commonly used to construct idler rolls. Besides steel rolls, idler rolls made of new materials are emerging. For example, Rulmeca Holding S.p.A. (2003) introduced TOP thermoplastic rolls. The TOP rolls are made of a thermoplastic material except bearings and shafts. Deep groove ball bearings are commonly utilized in idler rolls because they cannot only transfer radial force but endure a small amount of axial load. Sealing systems are important to prevent roll bearings from dust and water contamination.

In this section, the criteria as well as the industrial practice for the selection of idler rolls will be discussed. The selection of idler rolls needs to meet the technical, economic and environmental requirements. From the technical aspect, the main role of idler rolls is to provide support for a belt and conveyed bulk material with minimum rotating resistance (Geesmann et al., 2008). From the economic aspect, the selection needs to consider the life cycle cost of the rolls. The environment impact of idler rolls can be pollution in forms of noise, dust, spillage, as well as metal waste (Pang and Lodewijks, 2011). The industrial practice for the selection of idler rolls includes the calculation of the load on idler rolls and the selection of subcomponents including the bearing, shell, and shaft.

2.3.1 Idler selection criteria

There are five main criteria for the selection of idler rolls: the load carrying capacity, lifetime, cost, rolling resistance, and the environment impact.

The load carrying capacity is the primary requirement for idler rolls. The selection must ensure that selected rolls can endure the load exerted by a belt and bulk material (Geesmann et al., 2008). If the selected idler rolls cannot endure the load during operation, premature failure will occur soon due to excessive stress and deformation.

The lifetime of idler rolls is determined by a combination of the rolls and their operational conditions (Król and Kisielewski, 2014). It is difficult to estimate the lifetime of idler rolls because it may be affected by many variables which are hard to quantify. Idler manufacturers normally provide a rating lifetime according to the L_{10} bearing lifetime theory (Conveyor Equipment Manufacturers Association, 2014).

In view of the cost of belt conveyor idlers, the selection must consider the life cycle costs, including the initial investment of purchasing new idlers, associated operation and maintenance costs, and the cost of disposal. Compared to the initial investment, the operation and maintenance costs are hard to calculate due to the dependence on a given application, and lack of associated information such as quantification of the energy consumption and maintenance cost only allocated to idlers. The rolling resistance, mainly including the indentation rolling resistance (Lodewijks, 1995, 1996) and the rotating resistance of idler rolls (Geesmann et al., 2008), is a key determinant of the power consumption associated with idler rolls. This is of particular importance for long overland belt conveyors (Roberts and Harrison, 1987). The rolling resistance may contribute up to 40 percent of the total resistance of a belt conveyor (Gładysiewicz et al., 2004).

With growing requirement for the environment impact, the potential environment pollution becomes important consideration when selecting idler rolls. The noise emission is of big concern (Geesmann et al., 2009b). Failed rolls produce an excessive level of noise. The noise emission may cause serious problem for workforce in the field, and for

the residence if a belt conveyor passes through residential areas (Haines, 2007). The noise emission from idler rolls may originate from the shells, bearings or shaft ends, of which the first two are recognized as major source by CEMA (Farmer, 2000). One way to lower the noise pollution is to install acoustic enclosure. Recent introduction of new materials into roll construction, for instance polymeric materials, has been proven to lower the level of noise emission as well (Haines, 2007).

The selection of belt conveyor idlers also needs to consider the foreseen operational environment. The operational environment of idlers can be divided into interactions with their neighboring components and the ambient working environment.

The neighboring components of an idler include the transported bulk material, the belt and the conveyor structure. The properties of bulk material (i.e. the density and coefficient of internal friction) govern the idler spacing and the load on idler rolls (Geesmann et al., 2008; Liu et al., 2015a). Big lumps also result in high dynamic force on idler rolls (Conveyor Equipment Manufacturers Association, 2004). In addition, sticky materials, such as oil sand mentioned by Paton et al. (1995), will accelerate idler roll failures as they can aggravate the abrasive wear between a belt and roll shells (Figure 2.4).



Figure 2.4: Build-up of materials on an idler roll, figure courtesy of Nylocomp Ltd.

The weight of a conveyor belt contributes to the load on idler rolls. Besides that, flapping belts often lead to idler roll failures due to the inducement of extra load on idler rolls (Harrison, 1994). The sliding between a belt and a roll shell also accelerates the shell wear.

A stable and rigid conveyor structure can provide reliable support for idlers. On the other hand, a fragile conveyor structure will cause large deformation of idlers under the load of conveyed material, plus the weight of the belt and the idlers. Consequently, idlers under such circumstances will have more chances of run-out and premature failures (Watson and Niekerk, 1989).

The ambient temperature, humidity, and dust also have influence on the idler performance. Idlers which are exposed to extreme temperature will be largely influenced by the effectiveness of lubricant. A 20 km belt conveyor system which was subject to ambient temperature from $-53\text{ }^{\circ}\text{C}$ to $+33\text{ }^{\circ}\text{C}$ showed a high idler roll failure rate (Paton et al., 1995). The outdoor idler rolls (i.e. rolls in belt conveyors at bulk terminals) which are exposed to high humidity have potential risk of water contamination. Meanwhile, dust is also a large source of contamination for idler roll bearings (Granig, 2000).

2.3.2 Idler selection procedures

To select proper idler rolls for a belt conveyor project, the first step is to calculate the load on idler rolls during the foreseen operations. The load determines the dimensioning of idler rolls (Geesmann et al., 2008). The load needs to be examined at two levels, the load on one idler as a unit and the load on each roll of an idler.

The load on one idler consists of the weight of the idler, the resulting forces from the conveyor belt and the loaded bulk material within one idler spacing. Industry standards provide guidelines to calculate the forces from the belt and bulk material with given parameters of the conveyor (i.e. the capacity and belt speed), the belt (i.e. the type of belt and belt width), and the bulk material (i.e. the density and lump size). CEMA (Conveyor Equipment Manufacturers Association, 2004) established a guideline to calculate the forces on an idler by assuming a circular surcharge surface of the cross section of bulk material. Standard DIN 22101 (German Institute for Standardization, 2002) provides a theoretical calculation of the cross section based on a pentagonoid shape (Figure 2.5). The area of the cross section can be calculated as (German Institute for Standardization, 2002):

$$A_{th} = [l_M + (b - l_M) \cdot \cos \alpha]^2 \cdot \frac{\tan \beta}{4} + \left[l_M + \frac{b - l_M}{2} \cdot \cos \alpha \right] \cdot \frac{b - l_M}{2} \cdot \sin \alpha \quad (2.2)$$

where l_M is the length of the shell of the center roll (m), b is the loaded belt length (m), α is the trough angle ($^\circ$), β is the conveyor surcharge angle of the bulk material ($^\circ$).

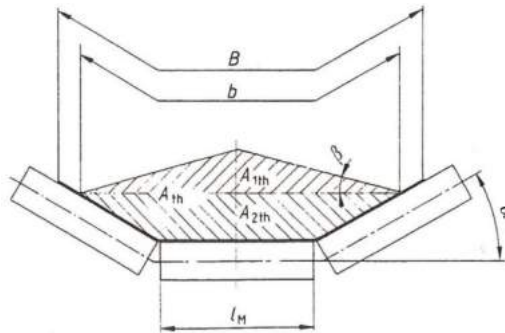


Figure 2.5: Theoretical cross section of bulk material in case of horizontal conveying and of three identical rolls, derived from German Institute for Standardization (2002).

The bulk volume can be further derived with the calculated cross section and a presumed idler spacing. Therefore, the weight of the bulk material within one idler spacing can be determined with the density of the bulk material. The weight of the belt within one idler spacing can be obtained from belt manufacturer.

After determining the load on each idler, the load on each roll can be further calculated. For idlers equipped with three identical rolls, load sharing among three rolls regarding the weight of the belt can be based on the contact length of the belt with each roll. In addition, a load sharing factor is commonly applied to derive the load from the bulk material on each roll. The load sharing factor can be expressed as a ratio between

the radial load on the center roll and the total weight of the bulk material within one idler spacing. The load sharing factor is empirical and generally within a range of 0.6 to 0.8 depending on the roll length and trough angle (Heemskerk, 1987; CKIT, 1991). Tooker (1988) mentioned the load sharing factors according to CEMA as in Table 2.1. With the load sharing factor, forces on the center roll and wing rolls can be calculated.

Table 2.1: Load sharing factors with varying trough angle.

Trough angle (°)	Load factor (-)
20	0.722
35	0.778
45	0.81

The selection of the subcomponents in an idler is normally based on the calculated load on the center roll. As center roll bearings are more heavily loaded than wing roll bearings, the selection of the six bearings in an idler is based on the calculated load on the center roll bearings. With the acquired load on the center roll, the load on either bearing can be determined. The type and size of bearings can be further chosen. The size of the bearing can be determined by comparing the calculated load on the bearing with the basic dynamic load rating of bearings provided by bearing manufacturers.

In addition to roll bearings, the selection of roll shell is also important. The shell needs to be capable to endure the load from the belt and the bulk material, while the eccentricity and unbalance is restricted in order to ensure quiet and smooth running of the rolls (Geesmann et al., 2009a). For the dimensioning of a shell, the thickness is the most important parameter. For idler rolls in a straight trajectory, it can be assumed that the load on one center roll is evenly distributed along the whole length of the shell. As a result, following equation applies to calculate the angular deflection y_{shell} of the shell of the center roll at the locations of bearings:

$$y_{shell} = \frac{ql_M^3}{24EI_y} \quad (2.3)$$

where q is the load on the shell (N/m) as a ratio of the center roll load and the shell length, E is the Young's modulus (GPa), I_y is the moment of inertia with respect to the y-axis. I_y can be calculated considering the shell as a thin tubular wall:

$$I_y = \frac{\pi d_0^3 s}{8} \quad (2.4)$$

where d_0 is the diameter of the shell (m), s is the thickness of the shell (m).

By applying Eq. (2.3) and (2.4), a minimum thickness of the shell can be obtained with a goal to keep the angular deflection not exceeding 0.004 radians required for the proper functioning of deep groove ball bearings (Tooker, 1988). Roll shells should be thick enough not just to guarantee a maximum tolerable deflection under the load, but also to survive the long term wear till the end of the lifetime of the roll.

The dimensioning of roll shafts is also important. The deflection of roll shafts strongly influences the performance of bearings if it exceeds a certain level. Excessive deflection of roll shafts induces significant extra stress in the contacts of bearings therefore shortens the fatigue life of bearings.

Figure 2.6 presents the schematic cutaway of a roll shaft. Considering the deflection of a shaft is dominated by the radial forces on bearings, it is possible to calculate the deflection of the shaft. If the radial forces on the two center roll bearings are equal, the deflection angle y_{shaft} of the shaft can be calculated as:

$$y_{shaft} = \frac{16 \cdot F_{NG,c} \cdot (a^2 + a \cdot c)}{\pi E d^4} \quad (2.5)$$

where a and c are dimensions in Figure 2.6, d is the diameter of the shaft (m), and $F_{NG,c}$ is the radial force on the center roll (N). From Eq. (2.5), the minimum diameter of the shaft can be derived which can meet the maximum allowable deflection angle of the shaft in order to ensure the bearing performance the same as the shell.

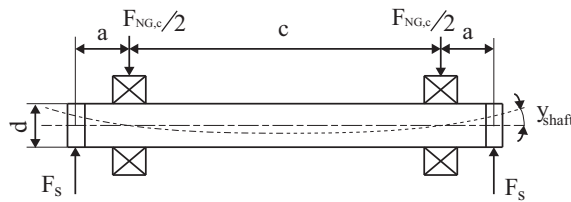


Figure 2.6: Schematic cutaway of an idler shaft assuming that the bearings do not transmit any moment.

From the industrial practice for the selection of idler rolls, it can be concluded that a precise determination of the load on idler rolls is still missing. The load sharing factors provided by industrial standards are rather rough estimations. Idler rolls which are selected according to such estimation often experience premature failures due to excessive loading (Król and Kisielewski, 2014). The unequal load sharing between the wing rolls and the center roll leads to unequal lifetime spans, which leads to challenges with the monitoring and replacements of rolls. In some industrial practices, groups of idler rolls are replaced at one time. This can result in waste of wing rolls which are still in good conditions if decisions on roll replacements are based on the condition of center rolls. On the other hand, severe center roll failures may occur if decisions on roll replacements are based on the condition of wing rolls. As a result, research on the determination of the load on idler rolls is needed.

2.4 Idler roll failure analysis

Improving the predictability of the performance of idler rolls requires analyses of their failures. Firstly, the definitions of idler roll failures, including the incipient failure, the final failure and the catastrophic failure are discussed. Figure 2.7 illustrates hypothetical condition change of an idler roll observed from condition monitoring versus its service time. Initially, the new installed idler roll works well under healthy condition. After a certain time, an incipient failure (i.e. spalling in the bearing) occurs to the roll as a result

of fatigue. The incipient failure is defined as the bearing fatigue failure, which refers to spalling on rolling elements or raceways reaching over 6.25 mm^2 according to Li et al. (1999). However, even when a spalling reaches such size, the spalling may propagate without impairment of proper rotating of the bearing. Therefore a roll with incipient failure can still fulfill its function until a final failure appears. Geesmann et al. (2008) define the final failure of an idler roll as the loss of its suitability for operation. A roll with the final failure may be observed impermissible noise emission, excessive runout, or even in stuck state (Tomsy, 1985). A roll reaching the final failure needs to be replaced quickly, otherwise the failure will develop into a catastrophic failure, in which the roll would cause severe damage to the conveyor belt (i.e. cutting the belt through its broken shell).

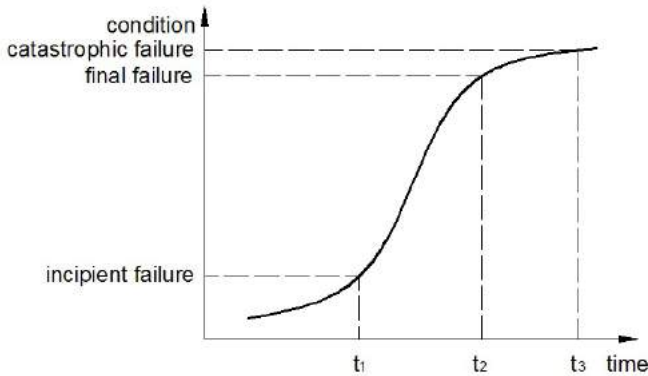


Figure 2.7: Hypothetical condition change of an idler roll versus its service time.

In this thesis, idler roll failure refers to the level of failure development between the incipient failure and the final failure ($t_1 \leq t < t_2$ in Figure 2.7). CEMA (Conveyor Equipment Manufacturers Association, 2014) suggests that for idler rolls equipped with tapered roller bearings, the final lifetime of the rolls is approximately 3 times of the L_{10} bearing fatigue lifetime. A bearing manufacturer for idler roll applications reported that the CEMA rule applies to deep groove ball bearings as well (Tooker, 1988). Therefore, if prediction of idler roll failures is achievable, there could be sufficient time to plan roll replacements in scheduled downtime of belt conveyors.

Secondly, failure modes of idler rolls are discussed. Bearing failures and shell wear are two main failure modes for idler rolls (Kruse, 2006; Zimroz et al., 2009). Figure 2.8 shows a survey of idler roll failures at an RWE mine (König and Burkhard, 2013). From Figure 2.8 it can be seen that bearing failures and shell wear are the two most frequent roll failure modes. Within the two main failure modes, the consequence of bearing failures is more significant. The rate of shell wear will be accelerated if one bearing runs into seized state. The malfunction of roll bearings is the most common idler roll failure mode (Rozentals and Msaime, 1981; Lodewijks, 2003; Wheeler and Ausling, 2007). Therefore, this thesis focuses on the roll bearing failures.

Reasons for roll bearing failures can be contamination, lack of lubrication, or overloading. Contamination (Figure 2.9) is a major factor that influences the actual lifetime of bearings (SKF, 1986; Paul and Shortt, 2007; Relcks, 2008). Bearing contaminants can

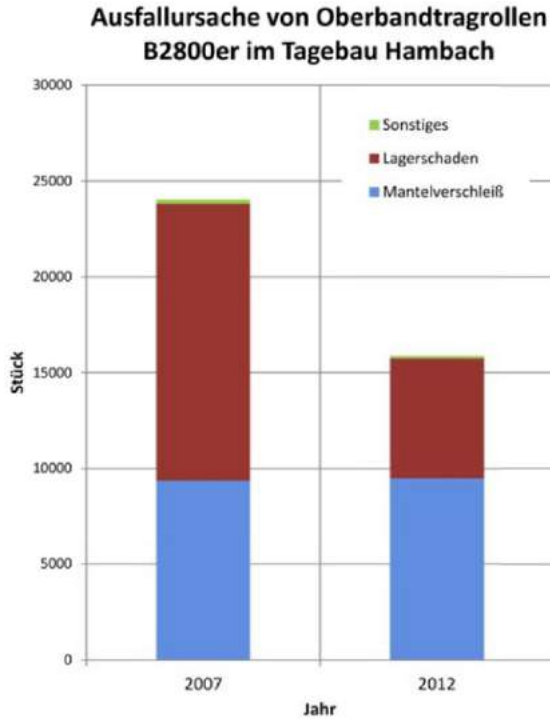


Figure 2.8: Failure modes of carrying side idler roll failures of belt conveyor B2800er at RWE Tagebau Hambach in 2007 and 2012 in form of number (Stück); Mantelverschleiß represents the shell wear, Lagerschaden indicates the bearing damage, and Sonstiges represents other causes, derived from König and Burkhard (2013).

be present in liquid and solid states. Therefore, the effectiveness of sealing systems is important as the sealing system are designed to isolate bearings from external contaminants. Malfunction of sealing systems fails to prevent contaminants from entering bearings, which will lead to bearing failure. The lubricant in a bearing is expected to function till the end of lifetime of the bearings. Though bearings can be designed to service very long time, the lubricant may not survive as long as the bearings (Roberts and Harrison, 1987). Therefore some bearings may be lack of lubrication when they are approaching failure. The misalignment and large deflection of roll shafts have negative effects on the lifetime of roll bearings by contributing additional radial and axial forces to the bearings (Watson and Niekerk, 1989; Paul and Shortt, 2007).



Figure 2.9: Contamination of rolling bearing, derived from Geesmann et al. (2008).

Shell wear of idler rolls is also a common phenomenon. Abrasive wear occurs to the shell of an idler roll as a result of sliding between the shell and the conveyor belt (Tuckey et al., 1985). This eventually attenuates the shell until it is broken (Figure 1.4). Abrasive wear can be affected by improper installation, unqualified frame design, belt curves, misalignment, and bearing failures (Madden, 1997). The abrasive wear can become much more worse if particles enter the interface between idler rolls and a belt. Particularly, Geesmann et al. (2008) pointed out that the shell wear tends to occur more to wing rolls than to center rolls because additional friction moments occur between wing belt sections and wing rolls due to the tendency of the wing belt sections moving towards center rolls.

The consequences of idler roll failures are among others added energy consumption, downtime, added maintenance cost, damages to equipment, and loss of revenue. The scale of idler roll failures depends on the failure rate of idler rolls in a belt conveyor, and the seriousness of roll failures. In a survey of failure rates of twenty belt conveyors for a period of six months, Gurjar (2012) found that idler roll failures constitute 74.1 percent of the total mechanical failures of the conveyors. Belt conveyors with stuck idler rolls consume much more energy. In some cases, if 10 percent of rolls are in seized state the belt conveyor would consume an additional 100 percent of power (Stewart-Lord, 1991).

Even worse scenario is that failed idler rolls can cause fire. Actually, idler rolls are identified as one of the main sources of fires in mines and power sector (Francart, 2006; Fernandez et al., 2013). One case is that Dong Power Energy Copenhagen caught a fire with huge financial loss in 2012 (Figure 2.10). Investigations concluded that the cause of the fire was that a failed hot roll dropped and ignited accumulated wood dust underneath

the conveyor belt (Barry, 2014).



Figure 2.10: Fire at Dong Power Energy Copenhagen, derived from Barry (2014).

2.5 Prediction of idler roll failures

Facing the consequences of idler roll failures, prediction of roll failures is important to achieve cost-effective maintenance of idlers. If adequate prediction of roll failures can be achieved, the inspection interval for idlers can be programmed correspondingly to ensure reliable operation of idler rolls while minimizing the cost of monitoring logistics. In addition, replacements of idler rolls can also be scheduled in planned downtime of belt conveyors based on the prediction. This can prevent breakdowns of belt conveyors due to abrupt occurrence of catastrophic failures of idler rolls during operation. Therefore the reliability of a belt conveyor at the equipment level can also be improved.

The prediction of idler roll failures needs to be considered at both the population level and the individual level. Considering the fact that there is a large amount of identical idler rolls under the same working condition, prediction of roll failures at the population level provides overall characteristics (i.e. failure rate) of idler rolls. Meanwhile, prediction of roll failures should be achieved at the individual level for decisions on which rolls need to be replaced in next maintenance time window.

In Chapter 1 it is stated that there are three potential approaches to predict idler roll failures. The three approaches are further elaborated in this section. Prediction of roll failures at the population level can be achieved by theoretical prediction of the reliability or lifetime of idler rolls. The L_{10} bearing lifetime theory from Lundberg and Palmgren (1949) is widely applied for the theoretical calculation of the lifetime of a population of bearings. According to the L_{10} bearing lifetime theory, the lifetime that ninety percent of a group of identical bearings under same working condition may survive can be calculated as (Lundberg and Palmgren, 1949):

$$L_{10} = \frac{10^6}{60n} \left(\frac{C}{P} \right)^3 \quad (2.6)$$

where L_{10} is the rating lifetime (hour), n is the constant rotational speed (rpm), C is the dynamic load rating from bearing manufacturers (N), P is the equivalent load on the bearings (N). The residual lifetime of the bearings can be further derived once the achieved service time is known.

For the prediction of the lifetime of bearings used in idler rolls, Eq. (2.6) is modified by researchers in order to take the specific working condition of belt conveyor idlers into account. For example, Geesmann et al. (2009a) provided a modified equation to calculate the rating lifetime of roll bearings:

$$L_{10,m} = a_1 a_2 a_3 \left(\frac{C}{\psi P} \right)^3 \frac{10^6}{60n} \quad (2.7)$$

where $L_{10,m}$ is the modified L_{10} lifetime of bearings (hour), a_1 is a factor concerning the bearing material, a_2 is a factor regarding the lubricant impurity, a_3 is a factor for the lubricant viscosity, ψ is the idler roll service factor.

Since the L_{10} rating lifetime is also associated with the reliability of bearings, the reliability of a population of roll bearings can be expressed as (Harris, 2001):

$$R_B = \exp(-0.1053(L/L_{10})^{10/9}) \quad (2.8)$$

where L is the achieved service time (hours).

The reliability of roll bearings in Eq. (2.8) provides a base to calculate the reliability of idler rolls which can be used to represent the overall reliability of the idler rolls in a belt conveyor for Eq. (2.1).

Meanwhile, the L_{10} bearing lifetime theory has limitations. The theory was developed to predict the lifetime or reliability of bearings which reach the incipient failure stage (bearings' lifetime), instead of predicting the lifetime of roll bearings reaching the final failure stage (rolls' lifetime) as argued in Section 2.4. The gap between the bearings' lifetime and the rolls' lifetime is technically correct and widely recognized, however, there is no laboratory test to provide proven equations to predict the roll's lifetime (Conveyor Equipment Manufacturers Association, 2014). In this case, prediction of the lifetime of idler rolls is still based on the L_{10} bearing lifetime theory in industrial standards like CEMA (Conveyor Equipment Manufacturers Association, 2014). Therefore, improvement on the predictability of the lifetime of idler rolls based on the L_{10} bearing lifetime theory is still important.

One way to improve the predictability of the lifetime of idler rolls is to use the actual load on roll bearings according to a record of real time throughputs of a conveyor. Figure 2.11 shows a time distribution of N levels of real time throughput (left y-axis) of a belt conveyor after running a certain time. The force on a roll bearing corresponding to each actual throughput level is also shown in Figure 2.11. For example, Q_i is the i th level of the real time throughput of the belt conveyor, P_i is the calculated force on one roll bearing according to the throughput Q_i , and T_i is the recorded subtotal operational time that the conveyor has run at the level of the throughput.

Assuming the design capacity of the belt conveyor is Q_m , and the corresponding equivalent force on one roll bearing is P_m . According to Eq. (2.7), the bearing rating lifetime $L_{10,m}$ is:

$$L_{10,m} = a_1 a_2 a_3 \frac{10^6}{60n} \left(\frac{C}{\psi P_m} \right)^3 \quad (2.9)$$

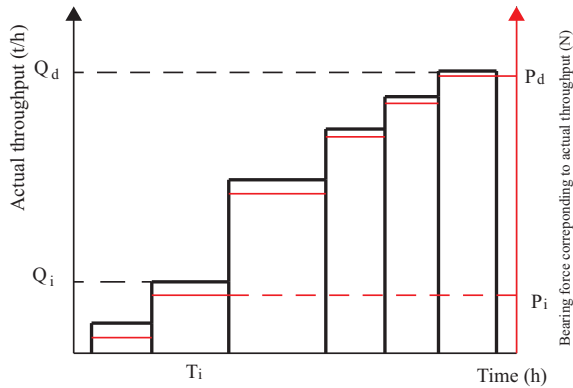


Figure 2.11: Record of actual throughputs of a belt conveyor and corresponding force on a roll bearing to each throughput level.

Note: The actual throughput Q_i is associated with the left y-axis; The corresponding force P_i on a roll bearing to a certain throughput Q_i is associated with the right y-axis.

On the other hand, prediction of roll failures at the individual level can also be achievable by applying condition monitoring techniques. If the evolution of certain physical parameters (i.e. temperature, vibration, and acoustic emission) of idler rolls can be associated with the hypothetical condition change verses the service time (Figure 2.7), diagnoses on roll failures will be more accurate. Even prediction of the final failure of an idler roll may be realized with sufficient acquired data and intelligent decision making algorithms.

The association between physical parameters and condition change of idler rolls can be challenging. Symptoms of idler roll failures can be sophisticated and random. Therefore, no consensus is reached on the representative parameters of idler roll failures. Some researchers claimed that temperature increase is a good indicator of roll bearing failures (i.e. Riley, 1994; Lodewijks et al., 2007; Pytlik, 2013). Some researchers consider that the vibration signal has distinguishable difference between health rolls and failed rolls (i.e. Bartelmus and Sawicki, 2000). The failure signal may occur one or multiple times during inspections. The symptoms of failure signal could also have different intensity and strength. All these lead to ambiguous diagnosis on the condition of idler rolls, let alone prediction of idler roll failures. Therefore, further research is needed to investigate which parameters can represent the technical condition of idler rolls.

Considering the limitations of the two approaches discussed above, prediction of idler roll failures based on integration of two source information, the lifetime/reliability information and the real time condition data is of interest. Integration of theoretical calculation of the reliability approach and the condition monitoring approach may improve the accuracy of prediction of idler roll failures.

2.6 Summary

In this chapter the reliability of belt conveyors is discussed. Research on the reliability of belt conveyors at both the equipment and the component level is reviewed. It is identified that idler rolls remain a challenge for the reliable performance of belt conveyors. Detailed

discussion about the selection of idlers are provided. The analyses of idler roll failures reveal the importance of prediction of idler roll failures for the cost-effective maintenance of idler rolls. Additional research is needed to improve the predictability of idler roll failures. Three approaches are proposed to predict idler roll failures. Chapter 3 and 4 will investigate the approach of theoretical calculation of the reliability of roll bearings, Chapter 5 will concentrate on the condition monitoring approach. Chapter 6 will explore the options of integrating the two approaches.

3

STRESS DISCONTINUITY MODEL FOR BULK LOAD DETERMINATION*

Chapter 2 pinpointed that the L_{10} bearing lifetime theory can be applied for the theoretical calculation of the lifetime or reliability of idler rolls. Subsequently the determination of the load on idler rolls due to the conveyed bulk material and the belt weight is essential. This chapter will investigate the determination of the load on idler rolls by developing an analytical approach for the derivation of the load due to the bulk material. Section 3.1 presents a brief introduction on the steps to derive the load on idler rolls. Section 3.2 introduces several related earth pressure theories in soil mechanics. Section 3.3 reviews previous models related to the determination of the load on idler rolls. Section 3.4 elaborates the development of an analytical model in this research. Section 3.5 proposes an aggregation of the model developed in this research and the model developed by Krause and Hettler (1974). Comparisons of results from the model in this research, the model from Krause and Hettler, the aggregation of the two models and experimental measurements will also be discussed in Section 3.5. Section 3.6 presents the calculation of the load on idler roll bearings. Section 3.7 provides some conclusive remarks.

3.1 Derivation of the roll load

For the theoretical calculation of the lifetime of idler rolls, the L_{10} bearing lifetime theory can be applied. To apply the L_{10} bearing lifetime theory, the load on roll bearings needs to be calculated accurately. The load on the two bearings within a roll originates from the conveyed bulk material, the conveyor belt, and the weight of the roll. There are three steps to determine the load on a roll bearing. The first step is to determine the load on a belt exerted by the conveyed bulk material (the bulk load). The second step deals with how to

*This chapter is partially based on Liu et al. (2014b, 2015a).

determine the load on each idler roll due to the loaded conveyor belt (the belt load). The third step is to calculate the radial and axial forces on each roll bearing based on the belt load (the roll bearing load).

For the calculation of the bulk load, the load distribution on the top cover of a belt due to the conveyed bulk material should be determined. The properties of the bulk material (i.e. the density) have a large influence on the bulk load. Industrial standards only provide empirical estimations of the bulk load. For example, DIN 22101 (German Institute for Standardization, 2002) applies the effective filling ratio $\varphi_{filling}$ to calculate the line bulk load m'_{bulk} as:

$$m'_{bulk} = \varphi_{filling} \cdot \rho \cdot A_{th} \quad (3.1)$$

in which ρ is the density (kg/m^3) of the conveyed bulk material, A_{th} is the area of the filling cross section in Eq. (2.2), and $\varphi_{filling} = \varphi_{Betr} \cdot \varphi_{St}$. The factor φ_{Betr} is determined by the properties of the conveyed bulk material (the lump size, maximum empty edge length on the belt, the angle of slope of the material on the belt) and by the operational conditions of the belt conveyor installation (uniformity of material feed, alignment of belt running, availability of a reserve capability). DIN 22101 only provides a qualitative instead of a quantitative guideline for the determination of the factor φ_{Betr} . The factor φ_{St} is dependent on horizontal, uphill or downhill installation of a conveyor, and can be quantitatively determined by the angle of inclination of the conveyor installation, the area of the filling cross section, and the surcharge angle of the bulk material on the belt.

Similarly, CEMA (Conveyor Equipment Manufacturers Association, 2014) considers the line bulk load m'_{bulk} as:

$$m'_{bulk} = \rho \cdot A_s \cdot K_1 \quad (3.2)$$

A_s is the area of the filling cross section in CEMA standard (m^2), and K_1 is the lump adjustment factor in a range of 1.0 and 1.4 empirically chosen according to the maximum lump size of the conveyed material.

Previous scientific research has revealed that bulk material experiences cyclic active and passive stress states due to the opening and closing movements of the belt as shown in Figure 3.1 (Krause and Hettler, 1974; Spaans, 1991; Wheeler, 2003b). When the belt passes over an idler, the wing belt sections (the WBSs in Figure 3.1) are released from a constrained trough shape by the idler (A to C: Belt Opening in Figure 3.1). When the belt approaches to the next idler, the WBSs are forced into a trough shape again (C to E: Belt Closing in Figure 3.1).

The opening and closing of the WBSs can be considered to be analogous to the movements of a retaining wall in soil mechanics. Therefore, theories in soil mechanics may be applicable to calculate the bulk load.

The calculation of the belt load is related to deriving the load on each idler roll based on the bulk load, the weight of the belt, the influence of the belt sag and the belt stiffness. The weight of the belt is usually provided by the belt manufacturer. The influence of the belt sag can be estimated by modeling the belt as a truss spanned between two idlers with a sag (Lodewijks, 1996). The extra force on trough idler rolls due to the belt stiffness can be neglected if a belt meets required troughability in industrial standards for instance ISO 15236-1 (International Organization for Standardization, 2005) because the belt will be compliant to a trough idler rolls without much resistance (Lodewijks, 2015). Standardized

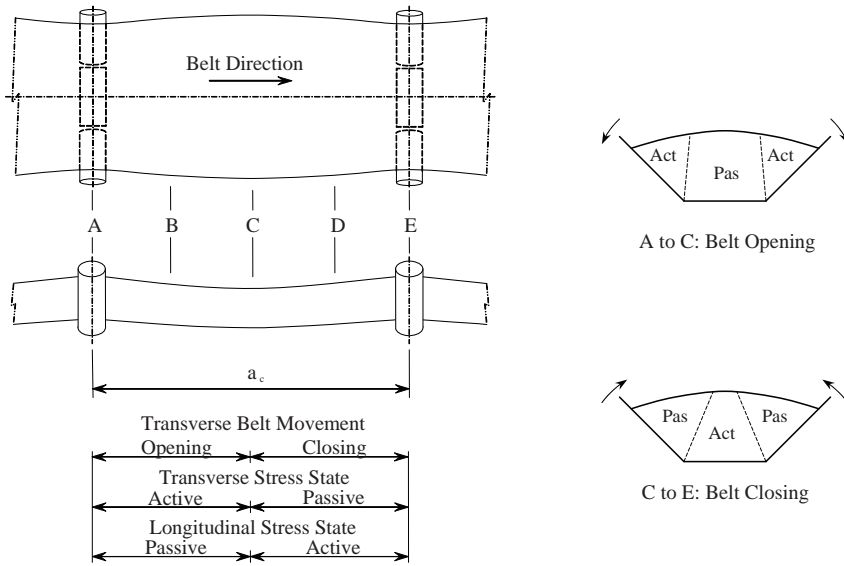


Figure 3.1: Transverse and longitudinal stress states within the bulk material due to the opening and closing of the belt, derived from Wheeler (2003b).

procedures to test the troughability of a conveyor belt are described in standard ISO 703 (International Organization for Standardization, 2007).

The calculation of the roll bearing load includes the derivation of the radial and axial forces on each roll bearing with the belt load and the weight of the roll shell. The normal load on the shell of a center roll can be considered as evenly distributed over the length of the shell. It is assumed that there is no axial load on a center roll if the belt is symmetrically loaded and not in a horizontal curve. For the normal load on the shell of a wing roll, an increasing load distribution from the outer edge towards the inner edge of the shell is expected. The axial force on wing roll bearings can be derived from the frictional force between the WBS and the wing roll, as well as the axial component of the weight of the wing roll.

Within the three steps, the calculation of the bulk load needs to be further investigated. The determination of the bulk load is required for the calculation of the belt load and the roll bearing load. The only widely recognized analytical model (the KH model) for the bulk load was developed by Krause and Hettler (1974). The KH model is considered to have limited accuracy on the derivation of the bulk load (Wheeler, 2003b; Ilic, 2013; Dratt et al., 2015). One reason is that the model incorporates Coulomb's earth pressure theory which is an upper bound theory that usually gives a solution greater than the true value (Budhu, 1999). One explanation can be attributed to the fact that the assumption of planar failure of a soil in Coulomb's earth pressure theory does not match the curved failure in reality (Clayton et al., 1993). This chapter will focus on the determination of the bulk load by developing an analytical model which incorporates a lower bound theory. Though numerical modeling gains popularity nowadays, analytical models are more applicable to be integrated into the theoretical calculation of the lifetime of idler rolls considering less required computation time, lower complexity of modeling and the

convenience of changing model parameters for different belt conveyors.

3.2 Related earth pressure theories

Research on the derivation of the bulk load commonly applies earth pressure theories from the field of soil mechanics. In this section several earth pressure theories will be briefly introduced, including Coulomb's earth pressure theory, Rankine's earth pressure theory, and Sololovski's stress discontinuity method.

3.2.1 Coulomb's earth pressure theory[†]

In 1776, Coulomb published his article *Essai sur une application des règles de maximis et minimis à quelques problèmes de statique, relatifs à l'architecture*, which is considered as the base of Coulomb's earth pressure theory. Coulomb's earth pressure theory is considered as an upper bound theory which overestimates the earth pressure on a retaining structure (Budhu, 1999).

In Coulomb's earth pressure theory, a soil under investigation is considered as a rigid mass (triangular block abc in Figure 3.2). A planar failure (the plane bc on which the force T locates in Figure 3.2) is assumed to occur through the soil from the surface till the interface between the soil and the retaining wall. Four forces are taken into consideration in Coulomb's solution: the weight of the soil, the supporting and frictional forces on the failure plane, and the thrust force from the retaining wall.

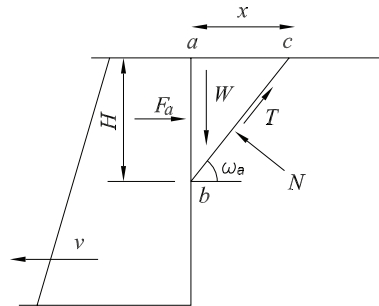


Figure 3.2: Geometry and force diagram for active earth pressure analysis in Coulomb's solution, derived from Clayton et al. (1993).

Coulomb considered that active stress state occurs within the soil when the retaining wall moves away from the soil. By solving the equilibriums of the forces perpendicular and parallel to the failure plane bc , Coulomb obtained an expression for the thrust force on the soil from the retaining wall. By differentiating the expression with respect to the inclination angle of the active failure plane, one can obtain the maximum value of the thrust force as:

$$F_{\max,a} = \frac{1}{2} \rho H^2 K_a \quad (3.3)$$

where H is the height of the soil (m), and K_a is the coefficient of active pressure which can be expressed as:

[†]All equations in this section are derived from Clayton et al. (1993).

$$K_a = \frac{1 - \sin \varphi_i}{1 + \sin \varphi_i} \quad (3.4)$$

in which φ_i is the internal friction angle of the soil ($^\circ$).

Meanwhile, the critical inclination angle that produces $F_{\max,a}$ is:

$$\omega_{a,crit} = 45^\circ + \frac{\varphi_i}{2} \quad (3.5)$$

By applying Eq. (3.3), one can calculate the force exerted on the retaining wall by the soil due to active failure.

On contrary, passive earth pressure occurs within a soil when a retaining wall moves against the soil. In this case, Coulomb derived an expression for the maximum thrust force $F_{\max,p}$ on the soil by the retaining wall as:

$$F_{\max,p} = \frac{1}{2} \rho H^2 K_p \quad (3.6)$$

in which the coefficient of passive pressure is:

$$K_p = \frac{1 + \sin \varphi_i}{1 - \sin \varphi_i} = K_a^{-1} \quad (3.7)$$

with the critical inclination angle $\omega_{p,crit}$ of the passive failure plane as:

$$\omega_{p,crit} = 45^\circ - \frac{\varphi_i}{2} \quad (3.8)$$

Coulomb's earth pressure theory was extended by Müller-Breslau to achieve a general expression for a frictional cohesionless soil with sloping backfill against a sloping back retaining wall with friction as shown in Figure 3.3.

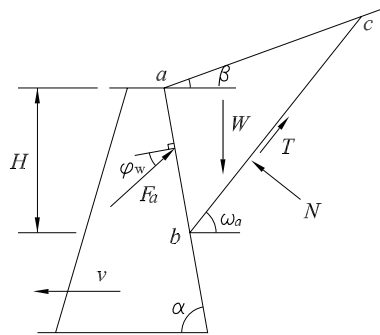


Figure 3.3: Geometry and force diagram for active earth pressure analysis in Müller-Breslau solution, derived from Clayton et al. (1993).

By constructing equations of forces perpendicular and parallel to the active failure plane as Coulomb did, Müller-Breslau derived an expression for the active thrust force on the soil by the retaining wall as:

$$F_a = \frac{1}{2} \rho H^2 \frac{K_a}{\sin \alpha \cos \varphi_w} \quad (3.9)$$

where

$$K_a = \frac{\sin^2(\alpha + \varphi_i) \cos \varphi_w}{\sin \alpha \sin(\alpha - \varphi_w) \left[1 + \sqrt{\frac{\sin(\varphi_i + \varphi_w) \sin(\varphi_i - \beta)}{\sin(\alpha - \varphi_w) \sin(\alpha + \beta)}} \right]^2} \quad (3.10)$$

in which α is the slope angle of the retaining wall ($^\circ$), φ_w is the friction angle of the soil with respect to the retaining wall ($^\circ$), and β is the inclination angle of the soil surface ($^\circ$).

The general Müller-Breslau solution of the thrust force by the retaining wall can also be obtained for the case of passive earth pressure, which can be expressed as:

$$F_p = \frac{1}{2} \rho H^2 \frac{K_p}{\sin \alpha \cos \varphi_w} \quad (3.11)$$

where

$$K_p = \frac{\sin^2(\alpha - \varphi_i) \cos \varphi_w}{\sin \alpha \sin(\alpha + \varphi_w) \left[1 - \sqrt{\frac{\sin(\varphi_i + \varphi_w) \sin(\varphi_i + \beta)}{\sin(\alpha + \varphi_w) \sin(\alpha + \beta)}} \right]^2} \quad (3.12)$$

Coulomb's earth pressure theory provides an approach to calculate the forces on a retaining structure against a soil in active and passive failure states. An assumption in Coulomb's earth pressure theory is that active and passive failures lead to planar failure interfaces within a soil. However, it was found later that failure interfaces are curved instead of being planar (Terzaghi and Peck, 1967; Clayton et al., 1993). The assumption of a planar failure interface generates relatively minor error in case of active earth pressure. But the assumption leads to serious overestimation of the force on retaining structures in passive stress state especially with high values of the wall friction [$\varphi_w \geq \phi_i/3$ as noted by Budhu (1999)].

3.2.2 Rankine's earth pressure theory [‡]

In 1857 Rankine published his paper *On the stability of loose earth*, by which he introduced the concept of effective stress to investigate an element of soil in a state of failure (Clayton et al., 1993). Therefore the effective stress states induced by stretching or compressing a soil element are named active or passive Rankine states (Terzaghi, 1943). Rankine's earth pressure theory is considered as a lower bound theory. Solutions derived from Rankine's earth pressure theory are generally lower than the true values (Budhu, 1999).

Figure 3.4 (a) shows an element of soil in active Rankine state. It can be seen that the normal stresses p and q_a are the principle stresses since there is no shear stress acting on the boundaries of the element. From the force equilibriums parallel and perpendicular to the slope side of the element [Figure 3.4 (b)], one can obtain:

$$\sigma ds = p dx \cos \omega + q_a dy \sin \omega \quad (3.13)$$

$$\tau ds = p dx \sin \omega - q_a dy \cos \omega \quad (3.14)$$

in which σ and τ are the normal and shear stresses on the failure slope (N/m^2), the x axis is perpendicular to the principle stress p and the y axis is perpendicular to the principal stress q_a .

[‡]All equations in this section are derived from Clayton et al. (1993).

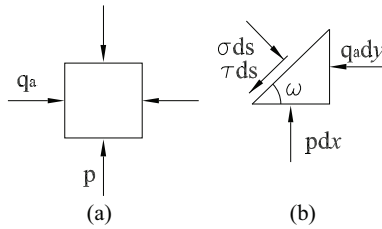


Figure 3.4: Element of soil in active Rankine state, derived from Clayton et al. (1993).

The failure of the element means that the friction on the slope reaches the maximum value, which yields:

$$\tau / \sigma = \tan \varphi_i \tag{3.15}$$

Figure 3.5 (a) shows an element of soil in active Rankine state which is located at depth z under inclined ground surface with an inclination angle β . Figure 3.5 (b) illustrates the Mohr circle which represents the effective stress state of the element of soil. In active failure state, the Mohr circle touches the failure envelope OF which is defined by the internal friction angle φ_i of the soil. In Rankine’s analysis, point X on the Mohr circle represents the normal and shear stresses on the plane parallel to the inclined ground surface in Figure 3.5 (a).

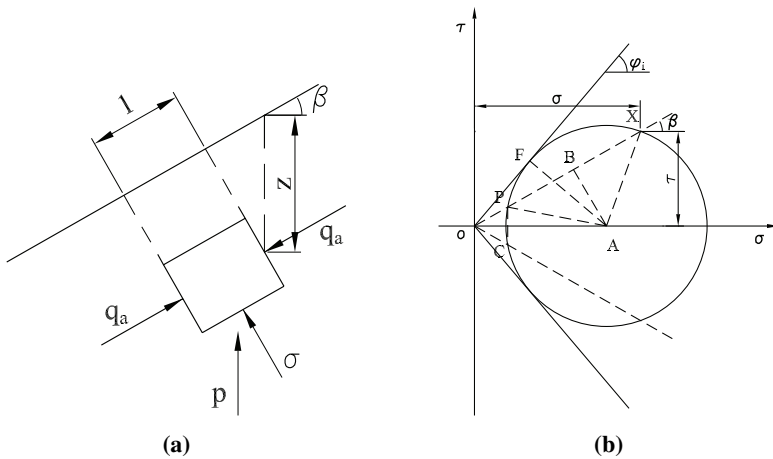


Figure 3.5: Analysis of soil in active Rankine state, (a) an element of soil located at depth z under incline ground surface, (b) Mohr circle for the element of soil in (a), derived from Clayton et al. (1993).

In addition, the normal and shear stresses on the vertical plane in Figure 3.5 (a) can be represented by point C in the Mohr circle in Figure 3.5 (b) by using the pole method. The coefficient of active Rankine state K_a can be further derived as:

$$K_a = \frac{q_a}{P} = \cos\beta \frac{\cos\beta - \sqrt{\cos^2\beta - \cos^2\varphi_i}}{\cos\beta + \sqrt{\cos^2\beta - \cos^2\varphi_i}} \quad (3.16)$$

In case of the inclination angle of the ground surface $\beta = 0$, which is equivalent to Coulomb's analysis in Figure 3.2, Eq. (3.16) produces the coefficient of active Rankine state K_a is:

$$K_a = \frac{q_a}{p} = \frac{1 - \sin\varphi_i}{1 + \sin\varphi_i} \quad (3.17)$$

which is the same result as Eq. (3.4) in Coulomb's earth pressure theory. This means that Rankine's earth pressure theory produces the same solution as Coulomb's earth pressure theory for the same geometry of soil-retaining wall structure. However, if the inclination angle of the ground surface $\beta \neq 0$, the solution from Rankine's earth pressure theory will be different from that of Coulomb's earth pressure theory.

Similarly, the coefficient of passive Rankine state K_p due to the passive failure in Rankine's earth pressure theory can be expressed as:

$$K_p = \frac{q_p}{P} = \cos\beta \frac{\cos\beta + \sqrt{\cos^2\beta - \cos^2\varphi_i}}{\cos\beta - \sqrt{\cos^2\beta - \cos^2\varphi_i}} \quad (3.18)$$

Rankine's earth pressure theory provides insight into the effective stress states of bulk elements, instead of looking at the global force equilibriums as Coulomb's earth pressure theory could offer. However, Rankine's earth pressure theory assumes that the principle stress q_a or q_p is parallel to the ground surface of the soil. Consequently, Rankine's earth pressure theory produces errors when the friction angle φ_w of a soil with respect to a retaining wall is not equal to the inclination angle β of the ground surface of the soil (Clayton et al., 1993).

3.2.3 Sokolovski's stress discontinuity method §

Sokolovski (1965) developed the stress discontinuity method to solve civil engineering problems that do not meet the requirements for the application of previous two earth pressure theories. The stress discontinuity method is a lower bound theory which means the solution is generally smaller than the true value (Powrie, 2004). The concept of stress discontinuity was introduced to describe the variation of the effective stress in a bulk volume. Examples of stress discontinuities can be found in failures of soil bodies (Schofield and Wroth, 1968), silo storage with mass flow (Cornish, 1973), shear bands in soil-structure interfaces (Ebrahimian et al., 2012) and so on.

Figure 3.6 (a) presents a stress discontinuity which separates two bodies of bulk material under different stress states. Each body consists of numerous infinitesimal bulk elements. In Figure 3.6 (b), Mohr circles are built to describe the stress states of bulk elements in body 1 (circle C_1) and body 2 (circle C_2) separately. For two bulk elements located at either side of the stress discontinuity, the stresses normal to the discontinuity plane must be equal to each other, while the normal stresses parallel to the plane can be different. As a result, Mohr circles of the two bulk elements intersect. The intersection [point A in Figure 3.6 (b)] depicts the normal stress and shear stress of the facets of both elements that are parallel to the discontinuity plane.

§This subsection is based on Liu et al. (2015a).

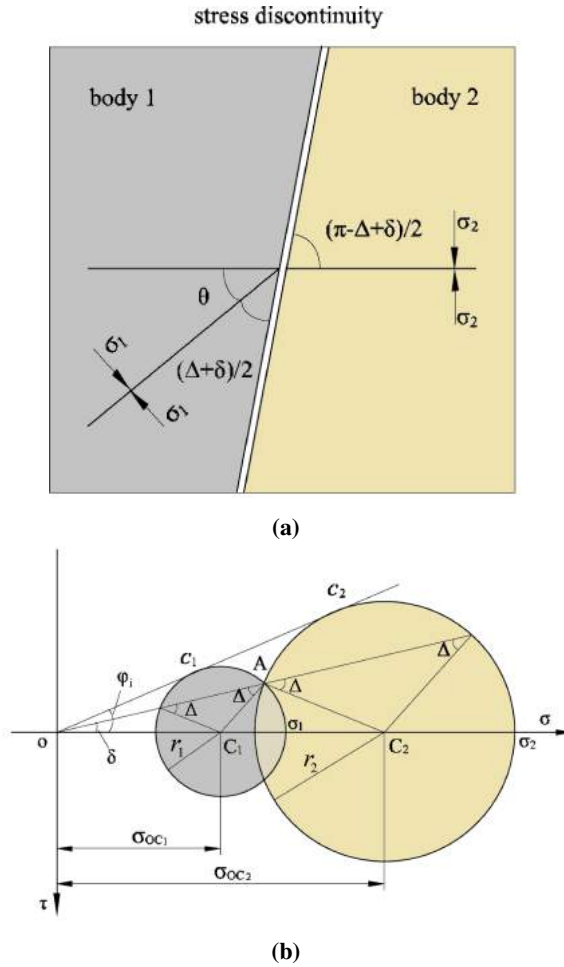


Figure 3.6: Concept of stress discontinuity, (a) areas on either side of a stress discontinuity with (b) Mohr circles, derived from Powrie (2004).

With the two intersected Mohr circles, the relationship of the effective stresses across the stress discontinuity can be retrieved. In most engineering problems, the direction and magnitude of the effective stress at one side of the discontinuity are already known, while the effective stress at the other side remains unclear. Assuming that the effective stress increases from body 1 to body 2, the average effective stresses σ_{OC_1} and σ_{OC_2} [Figure 3.6 (b)] have the following relationship (Sokolovski, 1965):

$$\frac{\sigma_{OC_2}}{\sigma_{OC_1}} = \frac{\sin(\Delta + \delta)}{\sin(\Delta - \delta)} \quad (3.19)$$

where Δ is an angle in Mohr circle [Figure 3.6 (b)] and $\sin \Delta = \sin \delta / \sin \varphi_i$, δ is the angle that indicates the strength mobilized on the discontinuity and $\tan \delta = \tau / \sigma$.

Moreover, the rotation of the direction of the major principal stress can also be obtained. In body 1, the plane that the major principal stress σ_1 acts on is at an angle of $(\Delta + \delta)/2$ to the stress discontinuity plane [Figure 3.6 (a)], while the plane for σ_2 is at an angle of $(\pi - \Delta + \delta)/2$ to the stress discontinuity in body 2 [Figure 3.6 (a)]. As a result, the rotation of the direction of the major principal stress across the stress discontinuity can be obtained:

$$\theta = \frac{\pi}{2} - \Delta \quad (3.20)$$

where θ is the rotation angle of the major principal stress [Figure 3.6 (a)].

The two intersections of the Mohr circles represent the effective stresses of the same magnitude but in different directions. This may result in different relationships of the effective stresses across the stress discontinuity. The selection of the intersection is generally determined by the stress state in body 1, the reference axes as well as the definition of the positive stress during the construction of Mohr circles.

After analyzing the condition of one stress discontinuity, the variation of the effective stress across a number of stress discontinuities can be considered. For each infinitesimal stress discontinuity, successive rotation and change in the major principle stress occur. For cohesionless bulk material, the two Mohr circles are almost overlapping with each other, so the mobilized strength δ tends to be the internal friction angle φ_i . As a result, for an overall rotation of angle θ_o of direction of the principal stress, the relationship of the average effective stress across the stress discontinuities can be obtained (Powrie, 2004):

$$\frac{\sigma_{OC_2}}{\sigma_{OC_1}} = e^{2\theta_o \tan \varphi_i} \quad (3.21)$$

The application of the stress discontinuity method does not have restrictions on the shape of the retaining wall as required for Rankine's earth pressure theory. Therefore it is a competitive method for many complicated problems of soil-structure interactions.

3.3 Review on bulk and belt models

The analyses of the bulk load and the belt load are complicated due to the lack of knowledge about the cyclic active and passive stress states in a bulk material during conveyance, and unascertained interface behavior between the bulk material-conveyor belt-idler rolls. Several researchers have applied earth pressure theories or numerical approaches to study the bulk load. Models for the belt load are also developed.

3.3.1 Models for the bulk load

The load distribution on a belt caused by a conveyed bulk material can not be simply derived from the weight of the bulk material. In fact, bulk material experiences active and passive stress states while the belt passing successive idlers. Analytical and numerical models have been developed to investigate the stress states in the bulk material and further to derive the bulk load.

Krause and Hettler's KH model

Krause and Hettler (1974) developed the KH model to study the bulk load based on the general Müller-Breslau solution in Coulomb's earth pressure theory. By comparing the cross section of a bulk material and a belt on an idler and the one in the middle of an idler spacing, a belt sag can be observed (Figure 3.7). Due to the loaded bulk material, the belt sags in both the x and z directions in Figure 3.7.

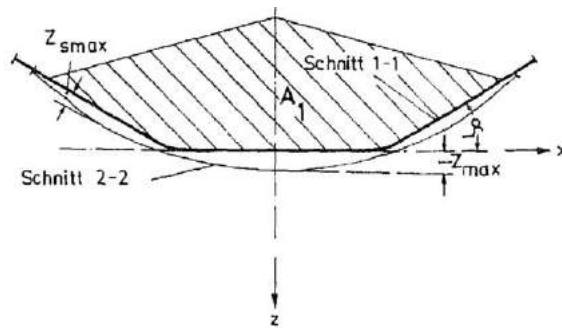


Figure 3.7: Bulk and belt profile during conveyance, derived from Krause and Hettler (1974).

In the KH model, several assumptions were made (Krause and Hettler, 1974):

- the belt opening occurs during the first half idler spacing, and the belt closing happens in the second half. Therefore, the bulk material on the WBSs within the first half idler spacing is in active stress state while within the second half the material is considered in passive stress state.
- the bulk material is considered as granular and cohesionless. The filling profile of the bulk material is after the theoretical shape in standard DIN 22101 (German Institute for Standardization, 2002) while the surcharge angle remains constant during conveyance.
- the opening and closing of the WBSs are considered to be about the joints between the two WBSs and the CBS. Consequently, two planar failures occur through the joints within the bulk material (Figure 3.1).

Figure 3.8 illustrates the geometry and the force diagram in the KH model for the analysis of active stress state due to the belt opening. Several forces are taken into account in the KH model, including the weight of the bulk material on the WBS, the supporting and frictional forces on the active failure plane, the normal and frictional forces from the WBS.

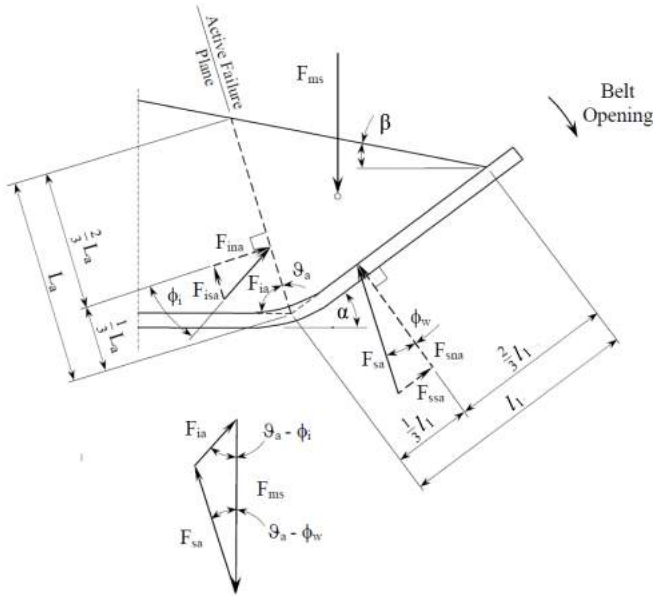


Figure 3.8: Geometry and force diagram in the KH model for active stress state analysis, reconstruction from Figure 3-8 in Wheeler (2003b).

By substituting the depth H of the bulk material as $l_1 \cdot \sin \alpha$, Krause and Hettler applied Eq. (3.9) in the general Müller-Breslau solution to calculate the normal force on the WBS in the first half idler spacing as:

$$F_a = \frac{1}{4} \rho l g l_1^2 K_a \cos \varphi_w \quad (3.22)$$

which l is the idler spacing (m), l_1 is the length of the bulk material on the WBS (m), K_a is the factor for active stress state which is given in Eq. (3.10).

The calculation of the normal force on the WBS in the second half idler spacing when the bulk material is in passive stress state can be derived as:

$$F_p = \frac{1}{4} \rho l g l_1^2 K_p \cos \varphi_w \quad (3.23)$$

which K_p is the passive stress state factor which is given in Eq. (3.12).

With Eq. (3.22) and (3.23), the total normal force on the WBSs within one idler spacing can be calculated, and the normal force on the CBS can be further calculated by establishing a force equilibrium in the vertical direction between the weight of the bulk material within one idler spacing and the normal and frictional forces from the WBSs and the CBS.

Krause and Hettler's work is widely considered as a milestone for the analysis of the bulk load (Katterfeld et al., 2010). Their work provides significant insight into the opening and closing movements of a belt during conveyance, and links the interaction between a bulk material and a belt to the mechanism of soil-retaining structures in soil mechanics.

However, the KH model has several limitations. Firstly, the wall friction in the KH model is considered to be effective only at the interface between the bulk material and the

WBSs. In reality the effect of the wall friction propagates within the bulk material and generates a curved failure plane (Terzaghi and Peck, 1967; Clayton et al., 1993; Wheeler, 2003b). Therefore, an interface zone exists within the bulk material adjacent to the WBSs in which the principle stresses of the bulk material are rotated under the influence of the wall friction. Secondly, the KH model applies Coulomb's earth pressure theory which is an upper bound theory. Consequently the KH model produces an overestimation of the passive normal stress on the WBSs. The overestimation of the KH model has been recognized by several researchers, for instance Wheeler (2003b) and Ilic (2013). Thirdly, the assumption of the opening and closing of the WBSs pivoting about the belt junctions in the KH model is under questioning. Based on a 3D scanned geometry, Ilic (2013) recently suggests that the opening and closing of the WBSs are more likely to pivot about the outer edge of the belt.

Ilic's DEM model

Recently the discrete element method (DEM) has been introduced into the analysis of the interaction between bulk materials and handling equipment including belt conveyor systems. Compared to continuum analysis which investigates the stress of a bulk material at a global or element level, the DEM provides detailed analysis of the interaction between handling equipment and individual particles (Katterfeld et al., 2010). In the DEM environment, an assembly of particles as well as their boundary can be simulated by inducing contact models such as the Hertz-Mindlin model (Ilic, 2013). Then the DEM is able to calculate displacements and forces acting upon each particle and the boundary.

Ilic (2013) developed DEM models to investigate the bulk load. Figure 3.9 shows one of the DEM models which is developed in the software code of Rocky (Granular Dynamics International, LLC.). In the resultant DEM model, the belt profile measured from a 3D scanner is implemented for a precise modeling of the belt deflection within one idler spacing. Five types of bulk materials, including coal, iron ore, gravel, magnetite, and river sand are chosen for the DEM models. The parameters of the bulk materials are determined from a series of calibration tests including the shear test, the wall friction test, the particle and bulk density test etc.

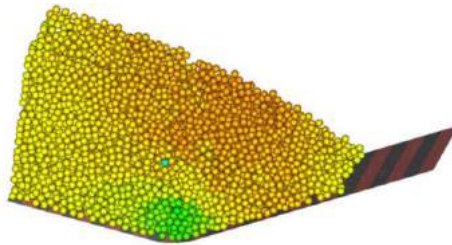


Figure 3.9: DEM model of a loaded conveyor belt, derived from Ilic (2013).

The results of the DEM models were compared with the gravitational force of the bulk material on the belt, as well as measurements from a Tekscan measurement system (detailed description about the Tekscan measurement system can be found in Chapter 4). The comparisons show that reasonably good overall correlation between the DEM modeled load profile and the measured load profile is achieved. However, the normal force exerted on the WBSs obtained from the DEM simulation is generally larger than the

experimental results for almost every bulk material in the tests. Meanwhile, the normal force on the CBS is lower than the experimental results. This indicates that the DEM simulation overestimates the normal force on the WBSs while underestimating the normal force on the CBS.

To date, DEM modeling still requires a lot of experience and knowledge for quantitative insights. For one thing, DEM modeling provides more qualitative rather than quantitative information at this moment (Barrios et al., 2013). Despite the DEM can provide close to reality simulation, quantitative information can be used only after the DEM models are verified and validated. The validity of DEM models largely depends on proper assignments of the properties of bulk materials (i.e. the size and shear modulus). Characterization and calibration tests can provide information for these properties. Nevertheless, the assignments of the values for these parameters in DEM modeling still require sophisticated analysis and experience. For another, DEM modeling is a customary process in order to provide fit-for-purpose models. Combinations of particle sizes, shapes and other properties can vary significantly for different applications. In addition, DEM modeling involves a large amount of particles, therefore the computation can be quite time consuming (Lommen et al., 2014).

3.3.2 Model for the belt load

Regarding the load exerted on idler rolls by a belt, one only needs to consider the weight of the belt and bulk material, but may also need to take the extra force caused by the belt sag into account. This section will examine whether it is necessary to take the belt sag into account by using a belt sag model.

Lodewijks's belt sag model

In a discrete analysis of the dynamics of a belt conveyor, Lodewijks (1996) considered a conveyor belt can be modeled by using three types of finite elements, a truss, a truss with a belt sag, and a beam. Within the three types of finite elements, a truss with a belt sag can be considered if one wants to take the belt sag into consideration. The extra force on idler rolls due to the belt sag can be calculated by modeling a loaded belt as a truss with a sag which is supported at two ends (Figure 3.10).

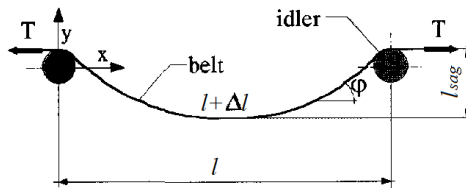


Figure 3.10: Static sag of a tensioned belt, derived from Lodewijks (1996).

From Figure 3.10 the belt sag l_{sag} can be calculated as:

$$l_{sag} = \frac{m'_{bulk} + m'_{belt} g l^2}{8T} = K_s l \quad (3.24)$$

in which m'_{bulk} is the weight of the bulk material per unit length (kg/m), m'_{belt} is the weight of the belt per unit length (kg/m), l is the idler spacing (m), T is the belt tension

(N), K_s is the sag ratio.

Furthermore, the angle between the horizontal and the tangent to the belt can be expressed as:

$$\varphi(x) = \frac{m'_{bulk} + m'_{belt}gx}{T} - \frac{m'_{bulk} + m'_{belt}gl}{2T} \quad (3.25)$$

At the left idler station when $x = 0$, Eq. (3.25) produces:

$$\varphi(0) = -\frac{(m'_{bulk} + m'_{belt})gl}{2T} \quad (3.26)$$

With the angle $\varphi(x)$ between the horizontal and the tangent to the belt, the additional length Δl of the belt due to the belt sag can be calculated:

$$\Delta l = \frac{l}{24} \left(\frac{(m'_{bulk} + m'_{belt})gl}{T} \right)^2 \quad (3.27)$$

Assuming the radial force on each idler due to the belt sag is perpendicular to the tangent of the belt at the contact area, and the frictional force is tangent to the belt, the radial force F_{NG} can be derived from the force equilibrium in the vertical direction as:

$$F_{NG} = \frac{(m'_{bulk} + m'_{belt})gl}{2 \cos \frac{(m'_{bulk} + m'_{belt})gl}{2T}} \quad (3.28)$$

By applying Eq. (3.28), the radial force on each idler due to the belt sag can be calculated.

With Lodewijks's belt sag model, it is possible to estimate to what extent the influence of a belt sag on the additional radial force on idler rolls. To carry out the analysis, an example of a belt conveyor is taken from CEMA (Conveyor Equipment Manufacturers Association, 2014). The main parameters of the bulk material and the belt conveyor are summarized in Table 3.1.

Table 3.1: Parameters of the bulk material and the belt conveyor, derived from Table 6.13 in Conveyor Equipment Manufacturers Association (2014)

Parameter	Value	Parameter	Value
material	crushed stone	design capacity (t/h)	2267.5
bulk density (kg/m^3)	1441.6	carrying idler spacing (m)	1.5
surcharge angle ($^\circ$)	20	belt width (m)	1.22
idler type	CEMA D6	belt tension rating (kN/m)	157.5
trough angle ($^\circ$)	35	belt line load (kg/m)	39.1

The example belt conveyor in CEMA (Conveyor Equipment Manufacturers Association, 2014) is not provided with information about the belt velocity and the roll length. Idler rolls with a shell length of 0.465 m are chosen for this case study. The resultant area of filling cross section of the bulk material on the belt is $A_s = 0.17 \text{ m}^2$, and the resultant

belt velocity is $v = 2.6 \text{ m/s}$. Assuming the lump adjustment factor $K_1 = 1$, the weight of the bulk material per unit length can be calculated by applying Eq. (3.2) as:

$$m'_{bulk} = \rho \cdot K_1 \cdot A_s = 1441.6 \times 1 \times 0.17 = 245.1 \text{ kg/m} \quad (3.29)$$

Assuming the belt tension T is equal to 19200 N, by applying Eq. (3.24), one can obtain the sag ratio as:

$$K_s = 2.8\% \quad (3.30)$$

which meets the maximum belt sag ratio between two carrying idlers required by CEMA standard [maximum belt sag ratio 3 percent as stated in Conveyor Equipment Manufacturers Association (2014)].

Furthermore, by applying Eq. (3.27), the additional belt length due to the belt sag can be calculated as:

$$\Delta l = \frac{l}{24} \left(\frac{(m'_{bulk} + m'_{belt})gl}{T} \right)^2 = 0.002 \cdot l = 0.003 \text{ m} \quad (3.31)$$

From Eq. (3.31) it can be seen that a very small additional belt length (0.2 percent) is produced due to the belt sag. Further applying Eq. (3.28), one can calculate the radial force on each idler under the influence of the belt sag as:

$$F_{NG} = \frac{(m'_{bulk} + m'_{belt})gl}{2 \cos \frac{(m'_{bulk} + m'_{belt})gl}{2T}} = \frac{(245.1 + 39.1) \times 9.81 \times 1.53}{2 \times \cos \frac{(245.1 + 39.1) \times 9.81 \times 1.53}{2 \times 19200}} = 2145.5 \text{ N} \quad (3.32)$$

If we neglect the belt sag, the vertical force on each of the two idlers due to the weight of the bulk material and the belt within one idler spacing can be calculated as:

$$F'_{NG} = \frac{m'_{bulk} + m'_{belt}gl}{2} = 2132.6 \text{ N} \quad (3.33)$$

Therefore, the error ε on the derivation of the belt load without taking the belt sag into account is:

$$\varepsilon = \frac{2145.5 - 2132.6}{2145.5} = 0.6\% \quad (3.34)$$

This indicates that the error on the derivation of the belt load without taking the belt sag into account is very limited. In conclusion, the belt sag generally can be neglected when calculating the belt load as long as the belt sag meets the maximum belt sag ratio of 3 percent.

3.3.3 Coupled model for the bulk and belt load

Rather than calculating the bulk load and the belt load in separate models, a more advanced approach is to develop coupled models to calculate the bulk load and the belt load. The calculation of the bulk load and the belt load is an iterative process. The bulk load leads to a belt deflection. The belt deflection will reversely cause re-distribution of the bulk material therefore a change of the bulk load. The change of the bulk load will

result in a further belt deflection. The bulk load and the belt load can be finally derived when both the bulk material and the belt reach stable states. Dratt et al. (2015) developed a coupled FEM-DEM model to determine the load on idler rolls due to a conveyor belt and a bulk material (Figure 3.11). The FEM model of the conveyor belt is carried out in ANSYS Classic based on Wheeler's finite model (Wheeler, 2003b). The DEM model of the bulk material is carried out in PFC3D (Itasca Consulting Group).

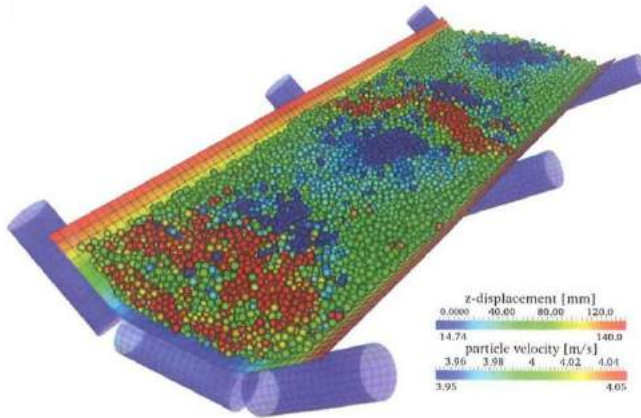


Figure 3.11: Coupled FEM-DEM simulation, derived from Dratt et al. (2015).

The resultant coupled FEM-DEM simulation is two way coupling (Katterfeld et al., 2010). One way is the transferring of the deformed profile of the belt from a FEM model to a DEM model. This is achieved by several steps. The first step is to export the node points of each shell element in the FEM model into a file. The second step is to generate two triangles for each shell element and to save as STL files. The last step is to import the STL files into the DEM model as walls.

The other way of coupling is to transfer the load on the walls in the DEM model to the FEM model as inputs of load. Considering the fact that the DEM model only uses the global coordinate system while the FEM model uses both the global and local coordinate system, the tangential force for each shell element of the FEM model has to be calculated manually based on the shear force and its exerting triangle wall elements in the DEM model (Katterfeld et al., 2010).

The two way coupling algorithm is verified by comparisons between a simulation of a static pre-tensioned belt segment loaded with bulk material and experiments. Using the verified FEM-DEM model, comparisons with the results of the KH model with respect to the load on idler rolls are also conducted. It is realized that the radial forces on the center roll from the coupled FEM-DEM model are 3 to 11 percent higher than those from the KH model, whereas the radial forces on the inner bearing of the wing roll from the coupled FEM-DEM model are 25 to 40 percent smaller than those from the KH model (Dratt et al., 2015).

3.4 Development of the SD model[¶]

Previous review indicates that analytical research on the bulk load is required. The existing KH model from Krause and Hettler (1974) provides overestimations on the bulk load on the WBSs while underestimating the load on the CBS (Wheeler, 2003b). Considering the KH model incorporates an upper bound earth pressure theory, a lower bound earth pressure theory may provide a more accurate solution. Within the two lower bound earth pressure theories mentioned in Section 3.2, Rankine's earth pressure theory is limited to soil-retaining wall applications where the inclination angle of the soil surface equates to the wall friction angle. For the bulk material conveyed on the belt, this might not be applicable because the surcharge angle of the bulk material can be different from the trough angle of the idlers. Therefore, Sokolovski's stress discontinuity method is applied to calculate the bulk load as a lower bound solution, which results in the SD model.

In this section, the development of the SD model is presented. Two assumptions have been made in the resulting SD model:

- bulk material is considered homogeneous and cohesionless
- the cross section of the loaded bulk material follows the theoretical shape in standard DIN 22101

Particle size is one of the important parameters that define the internal friction, as well as the thickness of the interface zone (Roscoe, 1970). Bulk material with diverse size distribution are out of scope in this research. As the adhesive stress effect is often negligible for dry bulk materials (Roberts, 1998), the cohesive behavior of dry bulk materials is also excluded in the SD model.

To develop the SD model, a new hypothesis of the dynamic movement of the bulk material on a moving belt is proposed based on recent experimental observations. The effective stress analysis is conducted regarding active and passive stress states separately. The bulk material is divided into a free surface zone and an interface zone. The interface zone is developed within the bulk material adjacent to the WBSs due to the wall friction and the belt movement. The relationship of the effective stress of bulk elements in different zones is built up using the stress discontinuity method. In the end, active and passive bulk load on the belt are obtained.

3.4.1 Dynamic movement of bulk materials

Analysis of the dynamic movement of the bulk material is of primary interest for the in-depth understanding of the behavior of the bulk material on a moving belt, the interactive phenomenon between the bulk material and the belt, and the determination of the direction of the internal friction as well as the wall friction.

When passing over consecutive idlers, the bulk material experiences transversal and vertical movements. During experiments carried out in this research (more details in Chapter 4), it was observed that the river sand sagged at the middle of each idler spacing (Figure 3.12). Another phenomenon is that river sand on the top surface of the central cross-section slides down to the edge immediately after passing over an idler (Figure 3.12).

[¶]This section is based on Liu et al. (2015a).



Figure 3.12: River sand within an idler spacing during conveyance.

Above phenomena cannot be explained by the traditional hypothesis proposed by Krause and Hettler (1974) in the KH model. Therefore, a new hypothesis is presented here. The dynamic movement of the bulk material is analyzed according to active and passive stress states separately. From zero belt sag (above an idler) to the maximum belt sag (at the middle of an idler spacing), the bulk material is in active stress state [Figure 3.13 (a)]. The downward movement of the CBS leads to a downward pivoting of the WBS about the outer edge of the belt [Figure 3.13 (a)]. As a consequence, bulk material on the WBS moves inward as shown in Figure 3.13 (a).

Based on Ilic (2013) hypothesis of the pivoting of the WBSs about the outer edges of the belt, it is considered that passive stress state is initiated by the upward pivoting of the WBSs due to the belt tension and belt stiffness [Figure 3.13 (b)]. The WBSs are also easier to recover from the maximum belt sag since the WBSs are less loaded than the CBS. With the sequence of the movement from the WBSs to the CBS, an assumption of a downward movement of the bulk material adjacent to the belt in passive stress state is made [Figure 3.13 (b)]. The downward movement can be obtained from the relative movement between the belt and bulk material. Meanwhile, the bulk material above the CBS is elevated significantly. The elevation can be so high that the internal friction cannot hold the particles on the top. As a result, these particles would slide downward to the outer edge.

The new hypothesis correlates to the experimental observations well. The sliding down of top surface particles can be interpreted by the movement of the bulk material in passive stress state. Moreover, contraction of particles at the junction between the WBSs and the CBS can be expected from this hypothesis due to the consistent sliding down of the material along the WBSs. The contraction is likely to exert extra high pressure on the belt junction, which is observed by Ilic (2013) during his experiments, and the experimental study in this research (more details in Chapter 4).

The new hypothesis is based on experimental observations of a fabric belt loaded with river sand. The movement of a bulk material on a steel cord belt may be different due to the high bending stiffness of the belt.

3.4.2 Active stress state analysis

Figure 3.14 illustrates active stress state of the bulk material above the WBSs in zone 1 (the free surface zone) and zone 2 (the interface zone). The directions of the normal stress

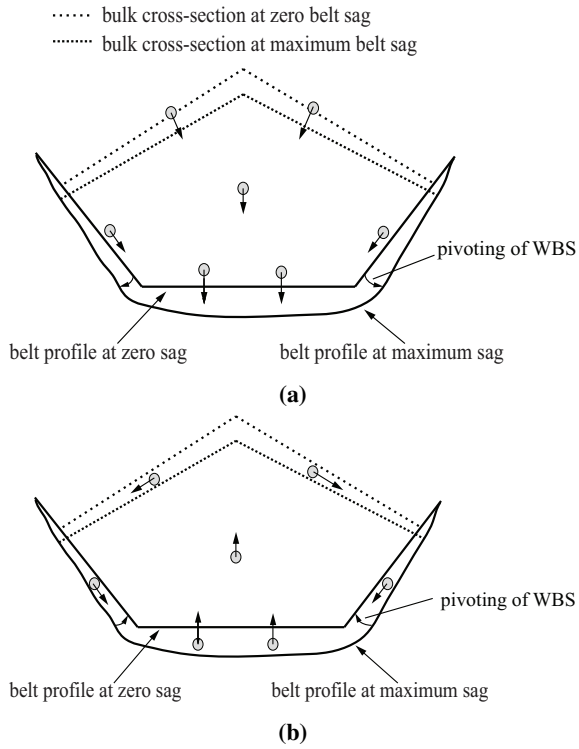


Figure 3.13: Dynamic movement of a bulk material during conveyance, (a) particle movement in active stress state, (b) particle movement in passive stress state.

and shear stress for bulk elements 1 and 2 (Figure 3.14) are determined by the proposed hypothesis in Section 3.4.1. For the definition of the positive shear stress, the shear stress which rotates the bulk element clockwise is defined as positive. While the compression stress is defined as the positive normal stress.

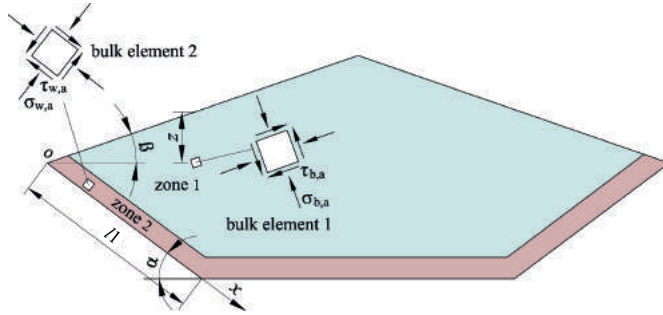


Figure 3.14: Bulk material in active stress state.

In order to investigate the stress state in zone 1, the stress field analysis for bulk element 1 needs to be carried out. Terzaghi’s theory (Terzaghi, 1943) is applied to determine the effective stress of bulk element 1, and the Mohr circle can be constructed (circle c_1 in Figure 3.15). Point D_1 on circle c_1 depicts the stress state of bulk element 1. From the geometry of Mohr circle c_1 , the major principal stress is at an angle of $[\pi/2 - (\Delta_1 + 3\beta)/2]$ clockwise from the horizontal axis. The normal stress $\sigma_{b,a}$ can be obtained:

$$\sigma_{b,a} = \rho g z \cos^2 \beta = \sigma_{OC1} + r_1 \cos(\Delta_1 + \beta) = \sigma_{OC1} [1 + \sin \varphi_i \cos(\Delta_1 + \beta)] \quad (3.35)$$

where ρ is the density of bulk material (kg/m^3), z is the depth of bulk element 1 (m), β is the surcharge angle ($^\circ$), φ_i is the internal friction angle ($^\circ$), σ_{OC1} is the average effective stress (N/m^2), r_1 is the radius of the Mohr circle c_1 (m) and $\sin \Delta_1 = \sin \beta / \sin \varphi_i$.

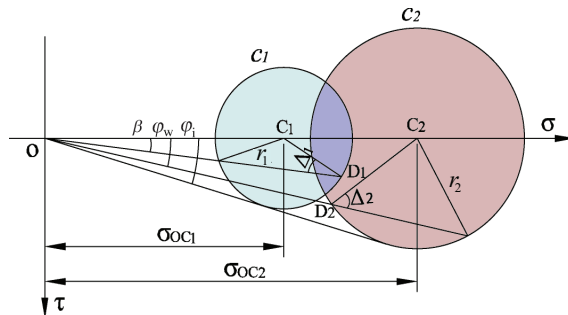


Figure 3.15: Mohr circles for the bulk elements 1 and 2 in active stress state in Figure 3.14.

Furthermore, the stress field analysis for bulk element 2 is conducted. With known directions of the effective stresses, a potential Mohr circle for bulk element 2 can be

constructed (circle c_2 in Figure 3.15). At this moment the position of the circle center C_2 remains unknown.

From Mohr circle c_2 , however, it can be derived that the major principal stress is at an angle of $[\alpha + (\Delta_2 - \varphi_w)/2]$ clockwise from the horizontal axis. In addition, the following equation regarding the normal stress $\sigma_{w,a}$ of bulk element 2 can be determined:

$$\sigma_{w,a} = \sigma_{OC2} - r_2 \cos(\Delta_2 - \varphi_w) = \sigma_{OC2} [1 - \sin \varphi_i \cos(\Delta_2 - \varphi_w)] \quad (3.36)$$

where φ_w is the wall friction angle, σ_{OC2} is the undetermined average effective stress (N/m^2), r_2 is the radius of Mohr circle c_2 (m), and $\sin \Delta_2 = \sin \varphi_w / \sin \varphi_i$.

In order to derive the average effective stress σ_{OC2} , the stress discontinuity method needs to be applied to investigate the relationship regarding the effective stress between zone 1 and zone 2. Considering the change of the effective stress from zone 1 to zone 2 as overcoming infinite number of stress discontinuities, the total rotation of the major principal stress can be calculated as:

$$\theta_a = \left| \frac{\pi - 3\beta - \alpha - \Delta_1 - \Delta_2 + \varphi_w}{2} \right| \quad (3.37)$$

By applying Eq. (3.21), the average effective stress of bulk element 2 can be obtained:

$$\sigma_{OC2} = \sigma_{OC1} e^{2\theta_a \tan \varphi_i} \quad (3.38)$$

Point D_2 on Mohr circle c_2 depicts the actual stress state of bulk element 2 adjacent to the WBS. After determining the average effective stress σ_{OC2} , the normal stress $\sigma_{w,a}$ and shear stress $\tau_{w,a}$ of bulk element 2 can be obtained:

$$\begin{cases} \sigma_{w,a} = \rho g K_a (\cos \alpha \tan \beta + \sin \alpha) x \\ \tau_{w,a} = \rho g K_a (\cos \alpha \tan \beta + \sin \alpha) \tan \varphi_w x \end{cases} \quad (3.39)$$

where α is the trough angle ($^\circ$), x is the distance (m) along the WBS in Figure 3.14, and the coefficient in active stress state:

$$K_a = \frac{1 - \sin \varphi_i \cos(\Delta_2 - \varphi_w)}{1 + \sin \varphi_i \cos(\Delta_1 + \beta)} \cos^2 \beta e^{2\theta_a \tan \varphi_i} \quad (3.40)$$

Finally, we determine the normal force and frictional force on the WBSs. Assuming that bulk material within half idler spacing is in active stress state, the normal force $F_{NG,bulk,a}$ and frictional force $F_{NA,bulk,a}$ that bulk material exerts on each WBS can be obtained:

$$F_{NG,bulk,a} = \frac{1}{4} \rho g l K_a (\cos \alpha \tan \beta + \sin \alpha) l_1^2 \cdot \frac{\cos^2 \alpha}{\cos^2 \beta} \quad (3.41)$$

$$F_{NA,bulk,a} = \frac{1}{4} \rho g l K_a (\cos \alpha \tan \beta + \sin \alpha) \tan \varphi_w l_1^2 \cdot \frac{\cos^2 \alpha}{\cos^2 \beta} \quad (3.42)$$

where l is idler spacing (m), l_1 is the length of bulk material on the WBS (m).

3.4.3 Passive stress state analysis

The analysis of passive stress state is similar to the determination of active stress state. However, the magnitudes and the directions of the effective stresses in the two zones are different (Figure 3.16). In zone 1, for example, the shear stress on the bottom facet of bulk element 1 now acts in the upward direction.

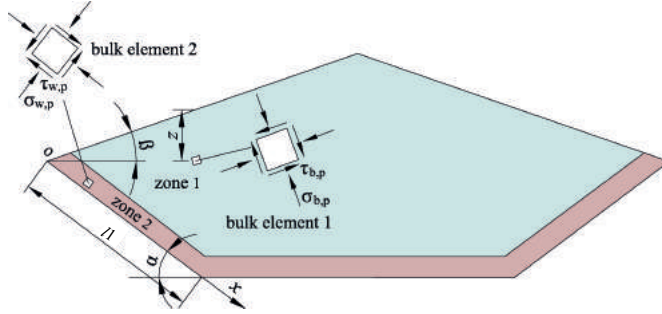


Figure 3.16: Bulk material in passive stress state.

As shown in Figure 3.17, Mohr circle c_3 represents the effective stress of bulk element 1 in zone 1, and Mohr circle c_4 depicts the stress state of bulk element 2 in zone 2 in passive stress state. The normal force $F_{NG,bulk,p}$ and the friction $F_{NA,bulk,p}$ that bulk material exerts on each WBS in can be obtained:

$$F_{NG,bulk,p} = \frac{1}{4} \rho g l K_p (\cos \alpha \tan \beta + \sin \alpha) \tan \varphi_w l_1^2 \cdot \frac{\cos^2 \alpha}{\cos^2 \beta} \quad (3.43)$$

$$F_{NA,bulk,p} = \frac{1}{4} \rho g l K_p (\cos \alpha \tan \beta + \sin \alpha) l_1^2 \cdot \frac{\cos^2 \alpha}{\cos^2 \beta} \quad (3.44)$$

and the coefficient in passive stress state

$$K_p = \frac{1 + \sin \varphi_i \cos(\Delta_4 + \varphi_w)}{1 + \sin \varphi_i \cos(\Delta_3 + \beta)} f_d \cdot \cos^2 \beta e^{2\theta_p \tan \varphi_i} \quad (3.45)$$

where f_d is the dynamic factor considering the belt sag. The dynamic factor f_d is an empirical factor that depends on the parameters of the belt conveyor among others the belt sag and belt tension, the belt velocity and the trough idler configuration. The dynamic factor is normally in the range of 1 to 1.9. An estimation of the dynamic factor f_d is given as $\left(1 + \frac{2\pi^2 v^2 K_s}{gl}\right)$ (Roberts, 1998), in which v is the belt velocity (m/s), K_s is the belt sag ratio, and l is the idler spacing (m). θ_p is the total rotation of the major principal stress in passive stress state as:

$$\theta_p = \left| \frac{\Delta_3 - \beta - 2\alpha + \Delta_4 + \varphi_w}{2} \right| \quad (3.46)$$

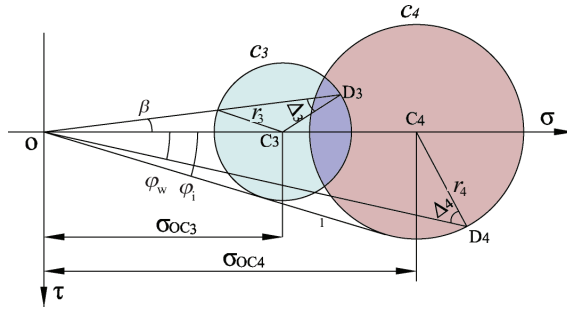


Figure 3.17: Mohr circles for the bulk elements 1 and 2 in passive stress state in Figure 3.16.

3.4.4 Derivation of the bulk load

With the normal and frictional forces on the WBSs calculated in subsection 3.4.2 and 3.4.3, the bulk load on the belt can be derived. The total normal force $F_{NG,w}$ and axial force $F_{NA,w}$ on each WBS within one idler spacing are as follows:

$$F_{NG,w} = F_{NG,bulk,a} + F_{NG,bulk,p} \quad (3.47)$$

$$F_{NA,w} = F_{NA,bulk,a} + F_{NA,bulk,p} \quad (3.48)$$

With the known normal forces and frictional forces on the WBSs, the vertical force equilibrium of bulk weight within one idler spacing can be established, from which the vertical (normal) force $F_{NG,c}$ on the CBS can be obtained:

$$F_{NG,c} = m'_{bulk} g l - 2 \cdot F_{NG,w} \cdot \cos \alpha - 2 \cdot F_{NA,w} \cdot \sin \alpha \quad (3.49)$$

in which m'_{bulk} can be derived by applying Eq. (3.1).

With the acquired bulk load on the belt, the load on each idler roll can be calculated by taking the belt weight into account. The radial and axial forces on each idler roll can be derived from the load on the WBS and CBS. A program for the optimization of load sharing among three idler rolls based on the SD model is also developed, which can be found in Appendix A.

3.5 Comparisons with the KH model

In literature, the KH model from Krause and Hettler (1974) is widely accepted for the determination of the bulk load even though with limited accuracy (Wheeler, 2003b; Ilic, 2013; Dratt et al., 2015). A comparison between the SD model and the KH model is useful to clarify the advantages and disadvantages of both analytical models.

A series of tests were carried out on a 65m long re-circulating belt conveyor at the University of Newcastle, Australia. The belt conveyor consists of a fabric belt PN300/2 and 35° offset three-roll trough idler with an equal roll length of 0.224 m. The measurement apparatus developed by Wheeler (2003b) was used during the tests to measure the normal and axial forces at each roll support. In total, six normal forces and two axial wing roll forces were measured (Figure 3.18). The bulk load on each WBS is assumed to be the

equivalent vertical force from the left or right wing roll measurements. The bulk load on the CBS is considered as the sum of center roll measurements. River sand was selected as the bulk material for the tests. Additional tests were undertaken to measure the properties of the river sand, which are presented in Table 3.2.

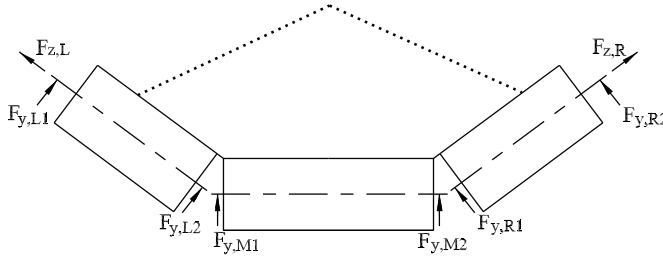


Figure 3.18: Positions of sensors during tests. Sensors $F_{z,L}$ and $F_{z,R}$ are used to measure the axial forces, other sensors are used to measure the normal forces.

Table 3.2: Parameters of the river sand and the belt conveyor

Material parameter	Value	Conveyor parameter	Value
material	river sand	capacity (t/h)	varying
density (kg/m^3)	1720	belt speed (m/s)	1~2
surcharge angle ($^\circ$)	15	idler spacing (m)	1.25
wall friction angle ($^\circ$)	26	belt width (m)	0.6
internal friction angle ($^\circ$)	46	belt line load (kg/m)	4.82

Tests were performed on the belt conveyor facility with different levels of throughputs, namely 245 t/h (100 percent loading level), 185 t/h (75 percent loading level), and 135 t/h (55 percent loading level). A typical measurement result is presented in Figure 3.19. It shows the measurement from sensor $F_{y,M1}$ of the measurement apparatus (Figure 3.18) when the empty belt with/without river sand passed the apparatus. The data acquisition frequency of all sensors is 10 Hz. From Figure 3.19, it can be seen that the belt portion with river sand arrived at the measurement apparatus around 20 seconds after the starting of the belt. Variations can be observed when the belt portion with river sand passed the sensors. This can be explained by the error of forming the bulk cross-section during the experiment, and the hysteresis of the sensor. A slight decrease in the force signal can also be noticed in Figure 3.19. It is probably due to the time drift of the sensor. Since the influence of the hysteresis and the time drift of sensors are rather small, this influence is compensated in the data analysis by averaging the acquired data. Data of each test was collected and processed, and the force components which were only caused by the loaded bulk material were extracted.

A detailed comparison of experimental results from the eight sensors with results from the SD model and the KH model is shown in Figure 3.20. Figure 3.20 (a) indicates a very good correlation between the predictions of the two models and the measurements of sensors $F_{y,M1}$ and $F_{y,M2}$ which measure the normal forces on the two supports of the

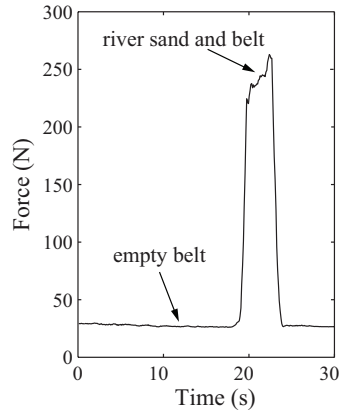
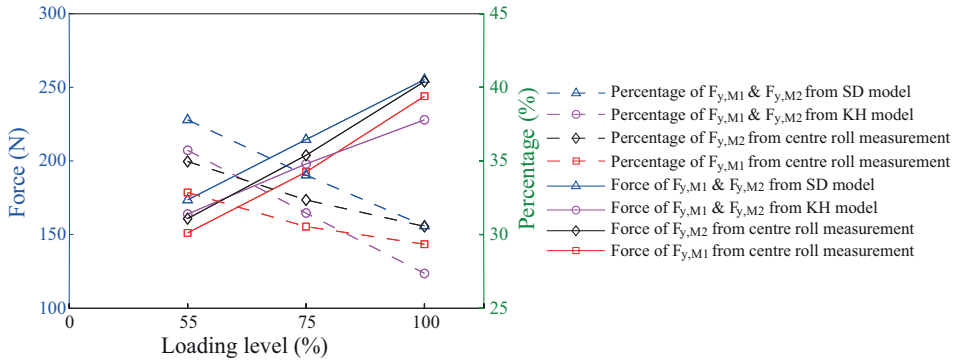
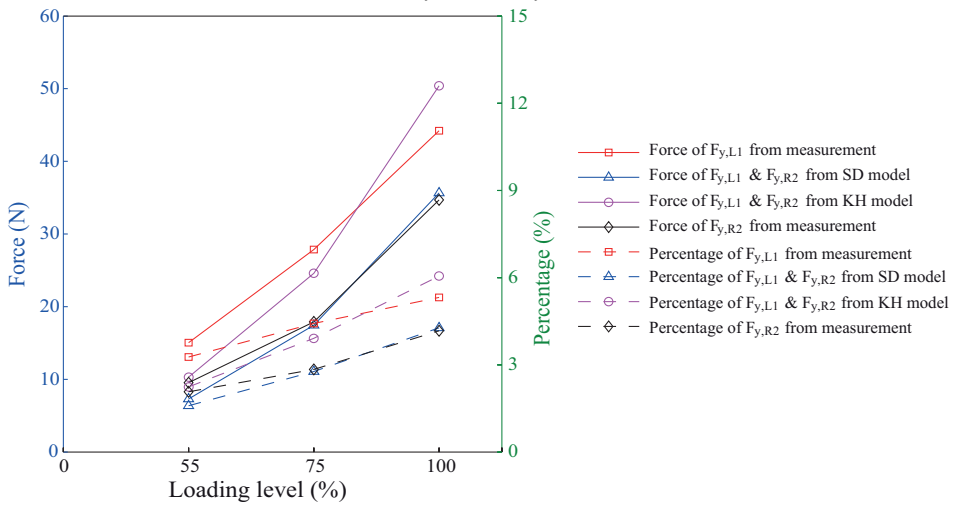


Figure 3.19: Typical measurement result during tests.

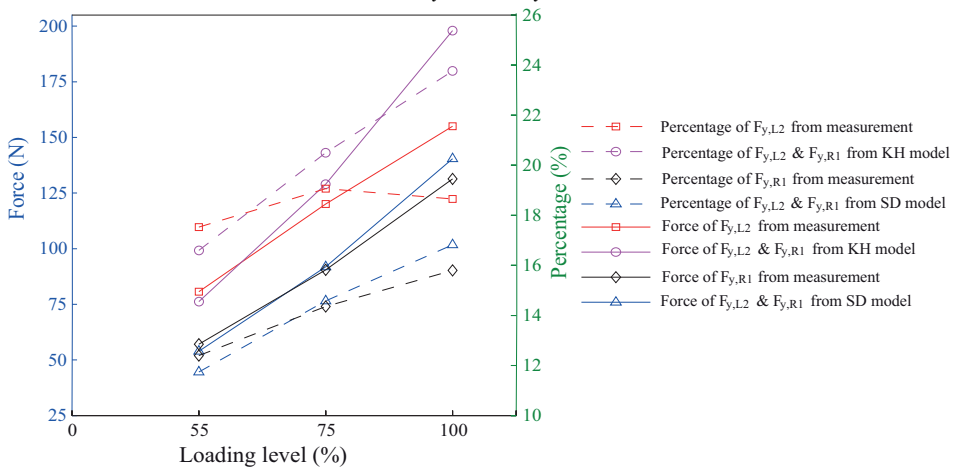
center roll (Figure 3.18). The percentage of the normal force on each support of the center roll with respect to the mass of the bulk material decreases with increasing capacity. For 55 percent loading level, the percentages derived from the SD model, the KH model, the measurement of $F_{y,M1}$, and the measurement of $F_{y,M2}$ are 37.8 percent, 35.7 percent, 32.9 percent and 34.4 percent respectively. When it comes to 75 percent loading level, the percentages of the bulk mass on each center roll support derived from the SD model, the KH model, the measurement of $F_{y,M1}$, and the measurement of $F_{y,M2}$ become 34 percent, 31.5 percent, 30.5 percent, and 33 percent respectively. For 100 percent loading level, the SD model predicts 30.6 percent of the bulk load on each center roll support, the KH model predicts 27.4 percent of the bulk load on each center roll support, the measurement of $F_{y,M1}$ shows 29.4 percent of the bulk load on each center roll support, while the measurement of $F_{y,M2}$ shows 30.6 percent of the bulk load on each center roll support. Compared with the measurements, the SD model overestimates the load on the center roll, while the KH model underestimates the load on the center roll for high loading levels.



(a) $F_{y,M1}$ and $F_{y,M2}$



(b) $F_{y,L1}$ and $F_{y,R2}$



(c) $F_{y,L2}$ and $F_{y,R1}$

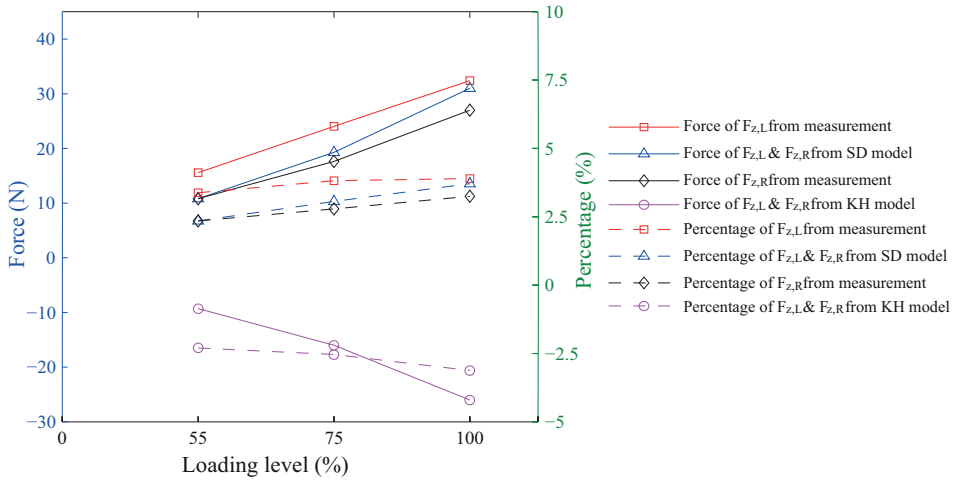
(d) $F_{z,L}$ and $F_{z,R}$

Figure 3.20: Comparisons of experimental results from eight sensors with the SD model and the KH model.

Note: The 'Force' and 'Percentage' in the legend correspond to the force on the left y-axis and the percentage on the right y-axis separately. The locations of the eight sensors can be found in Figure 3.18.

Figure 3.20 (b) and (c) show a good agreement between the predictions from the SD model, the KH model and the measurements of the normal forces at the two wing roll supports. Figure 3.20 (b) shows the force and its corresponding percentage on the outer wing roll support, while Figure 3.20 (c) shows the force and its corresponding percentage on the inner wing roll support. The percentage is achieved as the ratio between the normal force and the mass of the bulk material within one idler spacing. It can be seen that the normal forces at the wing roll supports increase with growing capacity. Moreover, the prediction from the SD model lies close to the 'lower bound' in both diagrams, whereas the KH model gives predictions close to or even higher than the 'upper bound'. In the case of 100 percent loading level, In Figure 3.20 (c), the KH model predicts that 23.8 percent of the bulk mass exerts on the inner wing roll support as the normal force, the percentages derived from the measurements of $F_{y,L2}$ and $F_{y,R1}$ are 18.7 and 15.8 respectively, while the SD model predicts that 17 percent of the bulk mass exerts on the inner wing roll support. Therefore, the KH model overestimates the normal force on the wing rolls while the SD model underestimates the normal force on the wing roll.

Figure 3.20 (d) depicts the comparison of the axial forces of two wing rolls. The axial force on the wing roll grows gradually with the increasing throughput. The SD model gives a good agreement with experimental results. The magnitude of the prediction from the KH model is also close to the experimental data. However, the direction of the axial force is opposite from test results. Krause and Hettler considered that the wall friction between bulk material and the belt changes the direction from active to passive stress state (Krause and Hettler, 1974). The hypothesis presented in Section 3.4 assumes that the wall friction does not change direction from active to passive stress state. The experimental

results confirmed that the proposed hypothesis is closer to the reality.

From the comparison above, it is also recognized that the SD model overestimates the load on the center roll while underestimating the load on the wing roll, meanwhile the KH model estimates the load on three rolls in the opposite way. Bearing in mind that the SD model provides a lower bound solution for the bulk load while the KH model gives an upper bound solution, an aggregation model (SD+KH) based on the SD model and the KH model may provide a solution closer to the true value of the bulk load than applying a single model. The aggregation of the SD model and the KH model can be expressed as:

$$F_{bulk} = \gamma \cdot F^{SD} + (1 - \gamma) \cdot F^{KH} \quad (3.50)$$

in which F_{bulk} is the calculated value of the bulk load (N) from the aggregation of the SD model and the KH model, γ is a factor that reflects the level of aggregation. γ is dependent on the characteristics of the bulk material such as the internal friction and the wall friction, the parameters of the conveyor belt such as the bending stiffness, and the loading level of the conveyor. F^{SD} refers to the calculation result from the SD model (N), and F^{KH} refers to the result from the KH model (N). A precautionary value of 0.5 for γ can be chosen for Eq. (3.50) in the case of the influential factors for γ are not known.

Figure 3.21 shows the bulk vertical force on the wing roll from experimental measurements, the KH model, the SD model and the aggregation of the two models with γ equal to 0.5. The bulk vertical force from the left roll measurement is the resultant force of measurements from sensors $F_{z,L}$, $F_{y,L1}$, and $F_{y,L2}$ in Figure 3.18. The bulk vertical force from right roll is the resultant force of measurements from sensors $F_{z,R}$, $F_{y,R1}$ and $F_{y,R2}$ in Figure 3.18.

Ideally, the vertical forces on the left and right wing rolls should be identical. Due to the belt misalignment, however, the vertical forces on the left and right wing rolls are different from each other. While it was difficult to control the belt misalignment during the tests, the measured forces from the two wing rolls give upper and lower bounds (Figure 3.21) where the true value of the bulk load may lie in. The vertical force on the left wing roll gives an ‘upper bound’, while the right roll gives a ‘lower bound’.

It can be seen from Figure 3.21 that the vertical force on the wing roll increases with a growing throughput. For a low throughput as 55 percent loading level, there is only 14 percent of the bulk material loaded on each wing roll. The percentage goes up to 22 percent when the throughput reaches 100 percent loading level.

Both the SD model and the KH model give good correlations with the experimental data as shown in Figure 3.21. In general, the prediction from the KH model is higher than that from the SD model. For high loading levels (more than 70 percent loading level), the prediction from the SD model lies between the upper and lower bounds. For low loading levels (less than 90 percent loading level), the prediction from the KH model also lies between the upper and lower bounds. Figure 3.21 also shows the calculated bulk load from the aggregation model by applying Eq. (3.50) is more accurate than a single model, especially for high loading levels of the conveyor.

To evaluate the accuracy of the SD model, the KH model, and the aggregation model, the errors of the prediction by the three models are calculated. It is assumed that the true value of the vertical force on each wing roll is the mean value of the vertical forces on the left and right wing rolls from measurements. The percentage of error ε is calculated as:

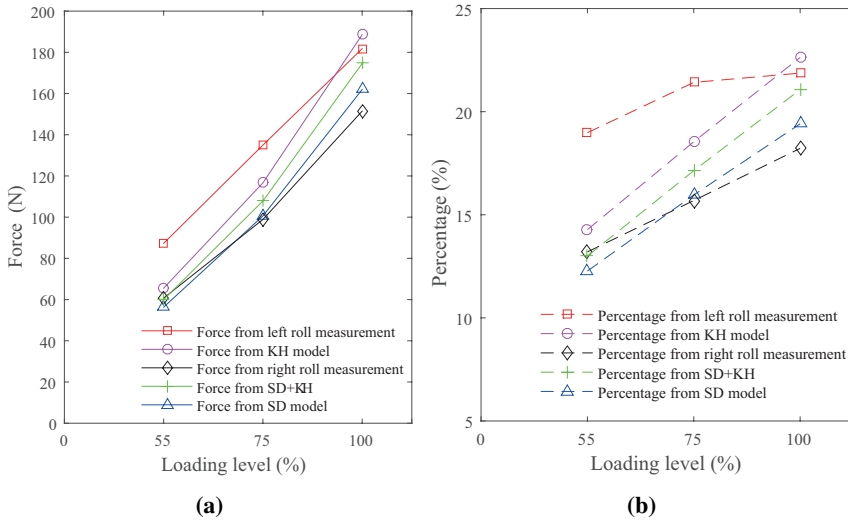


Figure 3.21: Bulk vertical force on the wing roll (a), and the corresponding percentage compared to the mass of the bulk material within one idler spacing (b).
Note: the 'Force' and 'Percentage' in the legend correspond to the force on the left y-axis and the percentage on the right y-axis separately.

$$\varepsilon = \left| \frac{F_{measure} - F_{bulk}}{F_{measure}} \right| \times 100\% \quad (3.51)$$

in which $F_{measure}$ is the true value of the vertical force on the wing roll in measurement (N), F_{bulk} is obtained by applying Eq. (3.50) with γ from 0 to 1. For $\gamma = 0$, Eq. (3.50) equates to the KH model. For $\gamma = 1$, Eq. (3.50) equates to the SD model. For $0 < \gamma < 1$, Eq. (3.50) produces different levels of aggregation of the two models. Therefore, Eq. (3.51) can be used to evaluate the errors of the predictions from the three models.

Figure 3.22 shows the percentage of error for the aggregation model with respect to three loading levels of the conveyor. For $\gamma = 0$ it represents the error of the prediction from the KH model. For $\gamma = 1$ it represents the error of the prediction from the SD model. For 55 percent loading level, the error for the SD model is 23.9 percent, and the error for the KH model is 11.5 percent. The predictions from both two models are lower than the true value. The error for the aggregation model increases linearly with rising γ . For 75 percent loading level, the error for the SD model is 13.9 percent, and the error for the KH model is 2.6 percent. The predictions from both two models are lower than the true value. Again, The error for the aggregation model increases linearly with rising γ . For 100 percent loading level, the prediction from the SD model is 2.8 percent lower than the true value while the prediction from the KH model is 13.1 percent higher than the true value. For the error of the prediction from the aggregation, it first decreases with rising γ (for $\gamma \leq 0.8$). For $\gamma > 0.8$ the error of the prediction increases again. Therefore, 0.8 is the optimum value of γ for the aggregation model in the case of 100 percent loading level.

In addition, for 100 percent loading level, if using the industrial empirical load sharing factor of 1/6 as the portion of the total bulk material loaded on each wing roll as mentioned in CKIT (1991), it will produce a 16.9 percentage of underestimation of the bulk load on

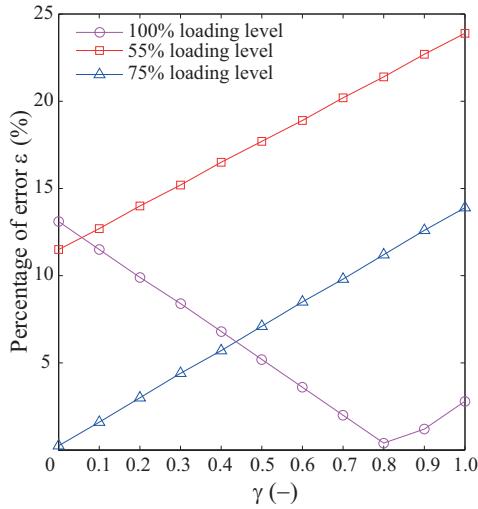


Figure 3.22: The percentage of error ε of predictions on the vertical force on a wing roll by using the aggregation of the SD model and the KH model with varying γ .

each wing roll compared to the measured bulk load. In this sense, the industrial empirical load sharing factor of $1/6$ underestimates the bulk load on the wing roll. For the other two loading levels, there is no empirical load sharing factor available.

For the bulk load on the center roll, the percentage of the mass of the bulk material loaded on the center roll (dash lines in Figure 3.23) decreases with a growing throughput though the vertical force is actually increasing (solid lines in Figure 3.23). Both the SD model and the KH model show a reasonably good agreement with the experimental results. For 55 percent loading level, the SD model predicts that 75.6 percent of the bulk material loaded on the center roll, the KH model gives a prediction of 71.5 percent, while the measurement shows that 67.8 percent of the bulk material loaded on the center roll. For 75 percent loading level, the SD model predicts that 68.1 percent of the bulk material is loaded on the center roll, while the KH model and the measurement give a value of 67.8 percent. For 100 percent loading level, the SD model predicts that 61.2 percent of the bulk material loaded on the center roll, the KH model gives a prediction of 54.7 percent, while the measurement shows that 59.9 percent of the bulk material is loaded on the center roll. Figure 3.23 also shows the calculated bulk load on the center roll by applying Eq. (3.50). It can be seen that the calculated bulk load from the aggregation model is more accurate than a single model, especially for high loading levels of the conveyor.

Figure 3.24 shows the percentage of error of the prediction on the vertical force on the center roll by using the aggregation model with varying γ . For $\gamma = 0$ in Figure 3.24, the percentage of error is the error only for the KH model as can be seen in Eq. (3.50) when $\gamma = 0$ is entered. Similarly, for $\gamma = 1$ in Figure 3.24, the percentage of error is only for the SD model.

In Figure 3.24, for 55 percent loading level, the error for the SD model is 11.3 percent, and the error of the prediction from the KH model is 5.1 percent. The predictions from both two models are higher than the true value. The error for the aggregation model increases linearly with rising γ . For 75 percent loading level, the error for the SD model

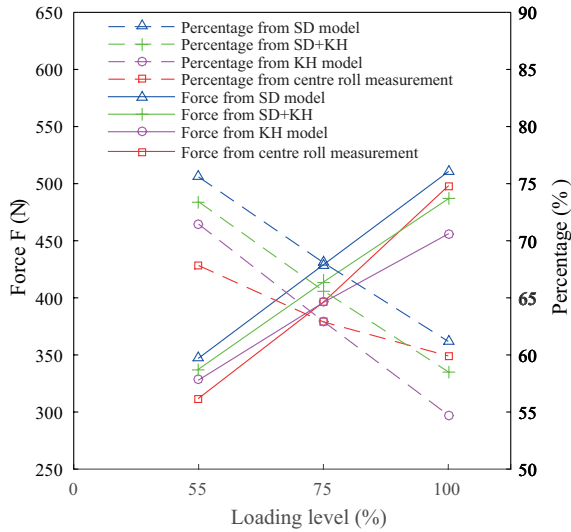


Figure 3.23: Bulk vertical force on the center roll.

Note: the 'Force' and 'Percentage' in the legend correspond to the force on the left y-axis and the percentage on the right y-axis separately.

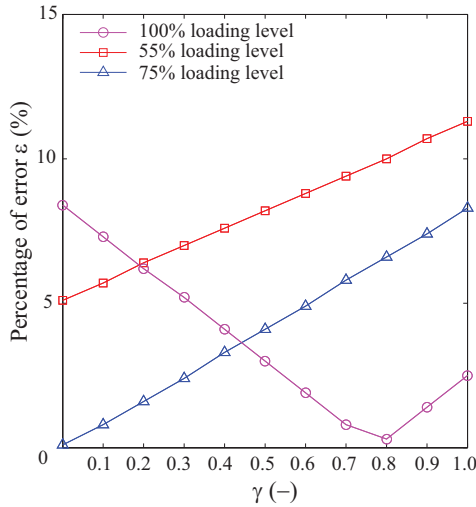


Figure 3.24: The percentage of error ϵ of predictions on the vertical force on a center roll by using the aggregation of the SD model and the KH model with varying γ .

is 8.3 percent, and the error for the KH model is 0.1 percent. The predictions from both two models are higher than the true value. Again, The error for the aggregation model increases linearly with rising γ . For 100 percent loading level, the prediction from the SD model is 2.5 percent higher than the true value while that from the KH model is 8.4 percent lower than the true value. The error for the aggregation model first decreases with rising γ (for $\gamma \leq 0.8$). For $\gamma > 0.8$ the error of the prediction increases again. Therefore, 0.8 is the optimum value of γ for the aggregation of the two models in the case of 100 percent loading level. The value is the same as the case of γ for the aggregation model for the wing rolls. Therefore, 0.8 is the optimum value of γ for the bulk load for 100 percent loading level in this case.

From the comparisons above, conclusions can be drawn that the results from the SD model and the KH model correlates well with experimental measurements. However, the SD model underestimates the bulk load on wing rolls (corresponding to the WBSs) and overestimates the bulk load on center rolls (corresponding to the CBSs). Whereas the KH model overestimates the load on wing rolls while underestimating the load on center rolls. An aggregation model based on the two models provides possibility to produce more accurate results than a single model. The aggregation factor γ requires further investigation.

3.6 The roll bearing load

With the derivation of the bulk load, it is possible to calculate the load on each roll bearing by taking the weight of the belt into consideration. Figure 3.25 depicts the force diagram for the bearings in a wing roll and a center roll in a straight trajectory.

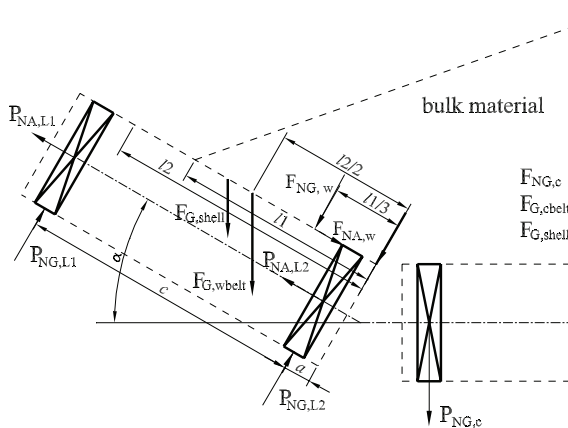


Figure 3.25: Force diagram for roll bearings.

On the shell of the wing roll, there are eight forces: the gravity of the WBS $F_{G,wbelt}$, the normal force $F_{NG,w}$ and frictional force $F_{NA,w}$ transmitted from the bulk load through the belt, the gravity of the shell $F_{G,shell}$, the axial supporting forces $P_{NA,L1}$ and $P_{NA,L2}$, as well as the radial supporting forces $P_{NG,L1}$ and $P_{NG,L2}$ from the two bearings. The gravity of the WBS $F_{G,wbelt}$ can be calculated as:

$$F_{G,wbelt} = m'_{belt} \cdot l \cdot \left(\frac{m - l_M}{2m} \right) \cdot g \tag{3.52}$$

in which m'_{belt} is the mass of the belt per unit length (kg/m), l is the idler spacing (m), m is the belt width (m), l_M is the shell length of the center roll (m).

The normal force $F_{NG,w}$ and the frictional force $F_{NA,w}$ of the bulk load can be calculated following Eq. (3.50):

$$F_{NG,w} = \gamma \cdot F_{NG,w}^{SD} + (1 - \gamma) \cdot F_{NG,w}^{KH} \quad (3.53)$$

$$F_{NA,w} = \gamma \cdot F_{NA,w}^{SD} + (1 - \gamma) \cdot F_{NA,w}^{KH} \quad (3.54)$$

By constructing the expressions of equilibriums of forces in the axial and radial directions for the wing roll, one can obtain the forces on the wing roll bearings as:

$$P_{NA,L1} = P_{NA,L2} = \frac{1}{2} F_{NA,w} + \frac{\sin \alpha}{2} (F_{G,shell} + F_{G,wbelt}) \quad (3.55)$$

$$P_{NG,L1} = F_{NG,w} \cdot \frac{l_1}{3a + 3c} + F_{G,wbelt} \cdot \cos \alpha \cdot \frac{l_2}{2a + 2c} + F_{G,shell} \cdot \frac{\cos \alpha}{2} - \frac{\sin \alpha \cdot d_0}{2a + 2c} (F_{G,wbelt} + F_{G,shell}) \quad (3.56)$$

$$P_{NG,L2} = F_{NG,w} \cdot \left(1 - \frac{l_1}{3a + 3c}\right) + F_{G,wbelt} \cdot \cos \alpha \cdot \left(1 - \frac{l_2}{2a + 2c}\right) + F_{G,shell} \cdot \frac{\cos \alpha}{2} + \frac{\sin \alpha \cdot d_0}{2a + 2c} (F_{G,wbelt} + F_{G,shell}) \quad (3.57)$$

in which the positions of the forces $P_{NA,L1}$, $P_{NA,L2}$, $P_{NG,L1}$, $P_{NG,L2}$ can be found in Figure 3.25, l_2 is the length of the WBS, a is the distance between the bearing and the bracket (m) in Figure 2.6, c is the distance between two roll bearings (m), d_0 is the diameter of the roll shell (m).

On the center roll, there exit the bulk load $F_{NG,c}$, the mass of the CBS $F_{G,cbelt}$, and the gravity of the shell $F_{G,shell}$. The bulk load can be derived following Eq. (3.50) as:

$$F_{NG,c} = \gamma \cdot F_{NG,c}^{SD} + (1 - \gamma) \cdot F_{NG,c}^{KH} \quad (3.58)$$

The mass of the center belt section $F_{G,cbelt}$ is:

$$F_{G,cbelt} = m'_{belt} \cdot l \cdot \frac{l_M}{m} \cdot g \quad (3.59)$$

Therefore, the radial force $F_{NG,c}$ on each bearing in the center roll is:

$$P_{NG,c} = \frac{F_{NG,c} + F_{G,cbelt} + F_{G,shell}}{2} \quad (3.60)$$

With the derivation of the load on wing roll bearings and center roll bearings, the lifetime or reliability of the roll bearings can be further calculated by applying the L_{10} bearing lifetime theory as already discussed in Section 2.5.

3.7 Conclusions

In this chapter an analytical approach is developed to determine the load on roll bearings due to the conveyed bulk material, the belt and the roll. For the belt load, it is concluded that belt sags contribute little additional load on idler rolls therefore the effect of belt sags on the roll load can be neglected. A new analytical model (the SD model) is developed in this chapter to provide a lower bound solution for the bulk load. Comparisons show that the SD model correlates reasonably well with experimental measurements. However, it is also observed that the SD model underestimates the bulk load on WBSs while overestimates the bulk load on the CBS. Combining the SD model with an upper bound model (the KH model) from Krause and Hettler (1974), an aggregation model for the bulk load is also developed. Comparisons between the SD model, the KH model and the aggregation model with experimental measurements show that the aggregation model is able to provide more accurate prediction of the bulk load than applying the SD model or the KH model.

4

EXPERIMENTAL DETERMINATION OF BULK LOAD*

Chapter 3 introduced the analytical model (the SD model) developed in this research to determine the load exerted on a conveyor belt by transported bulk material. Measurement of the distribution of the bulk load on a conveyor belt can provide information on how to improve theoretical models for the bulk load. However, direct measurement of the bulk load is still a challenge. This chapter presents an experimental study on measuring the bulk load on a running belt conveyor. A tactile pressure sensor is applied in the experimental study to investigate the pressure distribution on a belt. Comparisons between experimental measurements and results from the SD model are presented and discussed. Section 4.1 explains the motivation of the experimental study. Section 4.2 describes the experimental setup. Section 4.3 explains the experimental procedures. Section 4.4 discusses the techniques of data processing, and comparisons of results from the experimental measurements and the SD model. Section 4.5 gives some conclusive remarks.

4.1 Background

The bulk material may exert a high level of pressure on the conveyor belt due to the gravity and the dynamic movement during conveyance. The bulk load is further transferred to the idler rolls which influences the useful lifetime of the idler rolls.

Theoretical models have been developed to predict the bulk load. Based on Coulomb's earth pressure theory, Krause and Hettler (1974) developed the KH model to calculate the bulk load by considering the bulk material experiences active and passive stress states. In Section 3.4, the SD model, which is based on the stress discontinuity method, is introduced. Comparisons between the SD model and the KH model in Section 3.5 reveal

*This chapter is based on Liu et al. (2015b,c, 2016).

that the two models correlate reasonably well with the measurements of the forces on the idler roll supports. However, the two models are observed with either overestimation or underestimation of the forces on the idler roll supports to some extent. Therefore, an aggregated solution of the bulk load at the global force level has been developed as shown in Eq. (3.50) by introducing the aggregation factor γ . The determination of γ remains a challenge as it is influenced not only by the characteristics of the conveyed bulk material but also by the parameters of the belt conveyor.

Literature shows that no satisfactory sensors or procedures are available for the direct measurement of the bulk load. Previous experimental studies commonly applied load cells or strain gauges to measure the forces on the idler rolls. Geesmann (2001) developed an apparatus to measure the radial, lateral and horizontal forces on garland idler rolls. Grabner et al. (1993) designed a measuring apparatus to acquire the radial load distribution over trough idler rolls. Wheeler (2003a) developed an instrumented idler apparatus to measure the three dimensional (radial, lateral and horizontal) forces on trough idler rolls. The measured forces on idler rolls provide indirect estimation of the bulk load. However, these apparatuses only provide a few measuring points which limits the information of the bulk load.

Recent advances in the tactile pressure sensors show a promising potential to measure the bulk load. Ilic (2013) carried out preliminary measurements of the pressure on a belt simulation test facility and on a standstill conveyor belt caused by different bulk materials using a Tekscan pressure sensor. Regarding the measured results of the pressure on the belt simulation test facility, he divided the bulk load into two sections according to the belt opening and closing movements. Whereas for the measured results of the pressure on a standstill conveyor belt, he distinguished five sections of the pressure distribution within one idler spacing. However, the accuracy of the measured pressure was not assessed. Therefore it remains a question that the Tekscan pressure sensor provides qualitative or quantitative results of the bulk load. The pressure variation with different loading capacities was not investigated either.

The objective of this experimental study is quantify the bulk load distribution using a direct measurement approach. The first step is to assess the applicability of a tactile pressure sensor for the measurement of the bulk load. Using the tactile pressure sensor Tekscan 5315, measurements of the normal pressure on a running belt in an in-situ belt conveyor facility with varied loading levels is conducted. Comparisons of measurements from the tactile pressure sensor and well-established independent instruments are then performed. The errors of the measurements from the tactile pressure sensor are calculated. Comparisons indicate that the accuracy of the measurements needs to be improved. A post-process scheme is developed. Comparisons of the post-processed data and the measurements from a conveyor scale show that the scheme improves the accuracy. The pressure on the wing belt sections (WBSs) and the center belt section (CBS) is distinguished.

The transverse distribution of the bulk load on the belt at the stress/pressure level obtained from the measurements is also compared with theoretical calculation results. Within the three approaches (the SD model, the KH model, and the aggregated solution), the SD model is chosen. Krause and Hettler (1974) did not realize the necessity to provide the bulk load distribution at the stress level at that time, so they merely provided the derivation of the bulk load at the force level in their paper. Ilic (2013) gives two interpretations of the distribution of the bulk force on the WBSs: an average normal pressure

on the whole area of the WBSs and a total normal pressure acting 1/3 of the length up the inclined sides. However, these two interpretations lack evidences. Therefore, the aggregation of the SD model and the KH model is only considered at the force level [Eq. (3.50)]. The SD model is able to provide a normal stress distribution on the WBSs and the CBS. The transverse distribution of the measured bulk load in active and passive stress states will be presented and compared with the results from the SD model.

4.2 Experimental setup

All experiments are carried out on a 65 m re-circulating belt conveyor testing facility at the University of Newcastle, Australia. The experimental setup consists of a belt conveyor facility, river sand, a Tekscan pressure measurement system, a conveyor scale, and an instrumented idler apparatus (Figure 4.1).



Figure 4.1: Experimental setup.

4.2.1 Belt conveyor facility

The belt conveyor facility consists of two parallel belt conveyors which feed each other via storage bins and feeders. The main parameters of the testing facility can be found in Table 4.1.

Table 4.1: Parameters of the belt conveyor facility.

Parameter	Value	Parameter	Value
belt type	PN300/2	idler spacing (m)	1.25
belt width (m)	0.6	roll length (m)	0.224
belt velocity (m/s)	1	trough angle (°)	35

River sand has been chosen as the bulk material during all tests. The reason for choosing river sand is that the material has high bulk density (1720 kg/m^3 as measured in the test). The median grain size is 1 to 6 mm, which is much smaller than the size of the sensel (10 mm x 10 mm) in the sensor pad. This can minimize the influence of grain size on the accuracy of measurements.

4.2.2 Tekscan measurement system

The Tekscan pressure measurement system consists of a tactile pressure sensor pad, a sensor handle, I-Scan software and a laptop (Figure 4.1, the sensor pad is covered by rubber). Tekscan pressure sensor model 5315 is used in this experimental study (Figure 4.2). The 5315 sensor pad is 622 mm x 530 mm in size, and the sensing area is 488 mm x 427 mm consisting of a 48 sensels x 42 sensels matrix (Tekscan Inc., 2014). The sensor pad is made of two layers of polyester film, which consists of resistive materials and pressure-sensitive ink. The exerted force/pressure at each sensel is determined by measuring the change in the resistivity through the circuit of the two layers. The distribution of the pressure over the sensing area can be stored as a movie consisting of frames with a recording frequency of 25 Hz. This sensor model is chosen because the sensing area of the pad fits the loading area of river sand. The Tekscan software I-Scan is applied for the pre-processing of the acquired data.

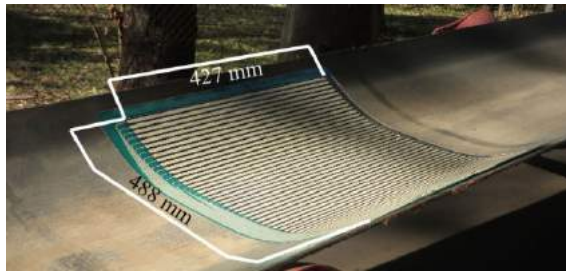


Figure 4.2: Tekscan pressure sensor model 5315.

Tactile pressure sensors are developed to measure the force, pressure and area of a loaded surface (Nicholas et al., 2012). Tekscan pressure sensors have been proved to be successful in the pressure measurement in static environment, for instance, the measurement of the load on the support structures buried in bulk stockpiles (He et al., 2014), the normal stress variation in the Jenike shear cell (Bilgili et al., 2004), and the normal wall stresses in hoppers (Johanson and Bucklin, 2004).

On the other hand, tactile pressure sensors have intrinsic limitations including the hysteresis and the susceptibility to curves (Buis and Convery, 1997). The sensors can be influenced by the loading rate, post-loading effects, creep, and hysteresis (Paikowsky and Hajduk, 1997). Further limitations like loss of the sensitivity and repeatability, inaccuracies between individual sensels were also reported (Dumbleton et al., 2009). Rose and Stith (2004) realized that Tekscan pressure sensors can produce varying measurement results depending on calibrations and sensor covering materials. As a result, customized calibration processes of tactile pressure sensors according to different applications draw intensive attention from researchers [i.e. (Paikowsky and Hajduk, 1997; Rose and Stith, 2004; Brimacombe et al., 2009; Palmer et al., 2009; Cazzola et al., 2013; Ganainy et al., 2014)]. However, customized calibration is quite challenging in the application of the pressure measurement on a running conveyor belt due to the difficulty in simulating a curved contact between the belt and the sensor.

4.2.3 Independent instruments

A conveyor scale and an instrumented idler apparatus are applied as independent references to assess the accuracy of measurements from the Tekscan pressure sensor. The conveyor scale utilized in this study is 3 m long, with an accuracy of ± 5 percent of read-out. The conveyor scale can provide the measurement of the bulk weight. The instrumented idler apparatus was designed to measure the normal and axial forces at each idler roll support (Wheeler, 2003b). The apparatus is utilized to compare with the Tekscan sensor in terms of the normal forces on the WBSs and the CBS. Detailed descriptions of the instrumented idler apparatus can be found in Wheeler (2003b). Within the two independent references, the conveyor scale was chosen as the main reference due to its accuracy, and the loss of the axial force registrations from the instrumented idler apparatus.

4.3 Experimental procedures

During the experiments the pressure caused by the bulk material is measured on a running belt with three levels of throughput: 245 t/h (100 percent loading level), 185 t/h (75 percent loading level), and 135 t/h (55 percent loading level). For each level of throughput, four trials were conducted. Three minutes of rest was provided between trials.

Prior to installation, the Tekscan pressure sensor was conditioned according to the manufacturer's recommendation. After that, the sensor pad was fixed to the top surface of the belt by glue tape, and covered using a thin rubber pad. The rubber pad can protect the sensor and minimize the influence of the shear force on the Tekscan sensor. The Tekscan sensor pad was placed in such a way that the width of the sensing area fits the loaded dimension of the belt (the loaded transversal dimension of the belt under 100 percent loading capacity is 490 mm according to standard DIN 22101 (German Institute for Standardization, 2002).

River sand was loaded from the feeder and shaped on the Tekscan sensor pad according to the theoretical geometry after DIN 22101 (German Institute for Standardization, 2002) before conducting each trial. The cross section of river sand was controlled by the clearance edge distance and the surcharge angle. To minimize slip-back, river sand was loaded on the belt within approximately three idler spacings.

Prior to the starting of the belt conveyor, the conveyor scale and the instrumented idler apparatus were calibrated carefully. During each trial, the conveyor scale and the instrumented idler apparatus registered the weight of river sand and the normal forces at roll supports independently.

After preparing all data acquisition systems, the belt conveyor was started. During each trial, the river sand passed around 30 idlers, including the conveyor scale and the instrumented idler apparatus before being stopped. Each trial lasted for about 40 seconds, and around 1000 frames of Tekscan data were collected per test (sampling frequency 25 Hz).

4.4 Results and discussion

The preliminary results from the Tekscan pressure measurement system cannot provide the bulk load within one idler spacing directly. Therefore, re-arrangement of the data is necessary. Facing the errors of measurements from the Tekscan system, a post-process scheme is further developed. The processed data are used to present the bulk load and

compare this with the results from the SD model.

4.4.1 Re-arrangement of preliminary results

Figure 4.3 shows representative results from the Tekscan pressure measurement system. In Figure 4.3 (a), the colored areas depict the pressure mapping while the red color indicates the pressure exceeding the saturation value of the sensel. The pressure mapping shows significant variations of the pressure distribution caused by the bulk material on the belt. Note that high peak pressures can be observed at the belt junctions [Figure 4.3 (a)] which face the idler junctions. From the pressure mapping in Figure 4.3 (b), it is also noticed that the contact area measured by the Tekscan pressure sensor is smaller than reality. As mentioned in Section 4.3, the whole sensing area of the Tekscan sensor pad was loaded by river sand. However, the sensels at the edge of the pad failed to register the pressure [white spots in Figure 4.3 (b)]. This is possibly due to a low magnitude of the pressure on the WBSs compared to the pressure on the CBS.

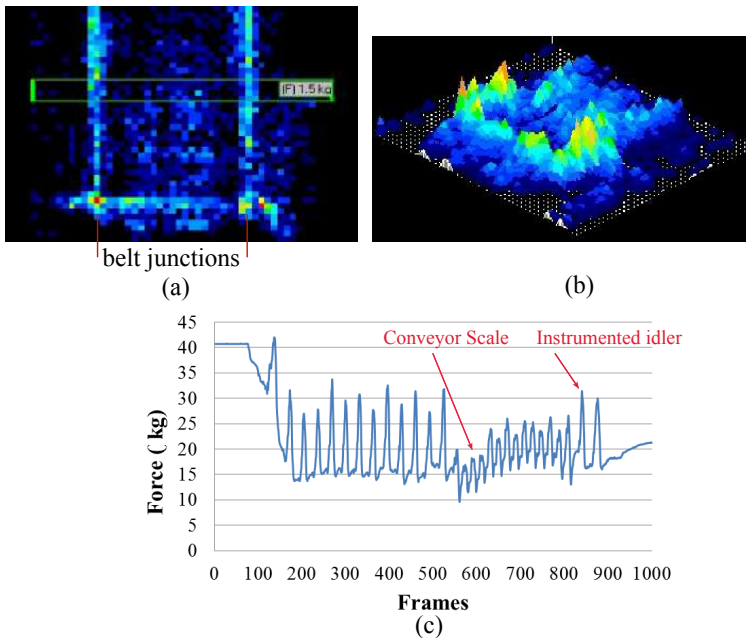


Figure 4.3: Pressure measurement results, (a) 2D pressure mapping, (b) 3D pressure mapping, (c) the total force vs frames.

Figure 4.3 (c) shows the total force exerted on the sensor pad versus sequential frames in one trial. The Tekscan sensor pad can produce 25 frames per second. As a result, Figure 4.3 (c) also depicts the temporal variation of the total force that the sensor pad experiences during 40 seconds running time. From the diagram, it can be seen that the Tekscan sensor pad experiences a high peak force when it passes over each idler. The positions of the conveyor scale and the instrumented idler apparatus are also shown on the diagram. Notice that the peak forces have variations. Larger differences can be seen before and after the pad passes the conveyor scale. One possible explanation is the difference of the belt sag due to the fact that the idler spacing of the conveyor scale (0.77m) is much smaller

than the normal idler spacing within the belt conveyor (1.25 m). The difference may also attribute to the offset versus inline roll configurations between normal idler sets in the conveyor and the idlers utilized in the conveyor scale.

The first challenge of data re-arrangement is to extract the pressure matrix within one idler spacing from the massive data collected by the tactile pressure sensor. For each trial, 1000 frames of raw pressure matrices were collected. I-Scan software provides the diagram of the force exerted on the whole frame versus the frame number [Figure 4.3 (c)]. From the diagram, it is possible to track the frame numbers during which the Tekscan sensor passed the conveyor scale. In addition, the corresponding frame numbers of two consecutive idlers from the peaks of the diagram was distinguished. Aware that the frequency of data acquisition for the Tekscan pressure sensor is 25 Hz, four rows of each frame were extracted to build up a pressure matrix which presents the pressure distribution on the belt within one idler spacing.

Figure 4.4 illustrates a typical 3D distribution of the normal pressure on the belt by using the filtering method mentioned above. For a better illustration, the pressure distribution within two idler spacings was presented. High peaks of the normal pressure at the idler roll junctions can be observed in Figure 4.4. The "mountains" of pressure develop from one idler to the neighboring one. Moreover, the Tekscan pressure sensor captured "high peaks" of pressure on the belt while the belt passes over each idler. The "high peaks" of pressure also correlates with the peak forces shown in Figure 4.3 (c). Furthermore, the pattern of the pressure mapping repeats at regular intervals the same as the idler spacing. However, the source of the "high peaks" of pressure has not been distinguished. The "high peaks" might come from the impact of idler rolls, or they may be exaggerated by the sensels due to the large deformation of the sensor pad facing the idler junctions. Another observation is that the normal pressure does not vary smoothly possibly due to the differences between individual sensels. With a Tekscan tactile pressure sensor, Ilic (2013) observed similar but lower magnitude of "high peaks" of the pressure on a belt simulation test rig.

The MATLAB program can also calculate the weight of the bulk material within one idler spacing. Table 4.2 summarizes the measured bulk weight from the conveyor scale. Figure 4.5 compares the measurements from the conveyor scale and the Tekscan pressure sensor. Taking the mean values of measurements from the conveyor scale as the references, the percentage of error of measurement is calculated and plotted for each trial. The Root Mean Square Error (RMSE) is also calculated to estimate the mean error of measurements from the Tekscan pressure sensor.

Table 4.2: Measurements of bulk weight from the conveyor scale.

55 percent loading level	Test	T1	T2	T3	T4	Mean value
	Weight (kg)	115.7	115.7	115.4	115.6	115.6
75 percent loading level	Test	T1	T2	T3	T4	Mean value
	Weight (kg)	156.9	156.5	156.3	156.2	156.5
100 percent loading level	Test	T1	T2	T3	T4	Mean value
	Weight (kg)	206.4	206.3	206.8	206.7	206.6

Note: The length of the conveyor scale is 3m.

From Figure 4.5, it can be seen that the percentage of error varies from 8.7 percent to

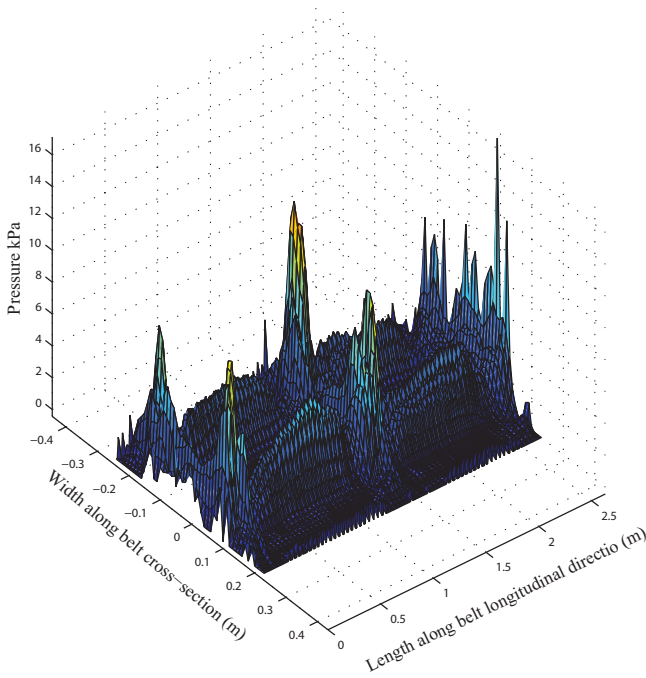


Figure 4.4: Typical 3D distribution of raw normal pressure distribution within two idler spacings.

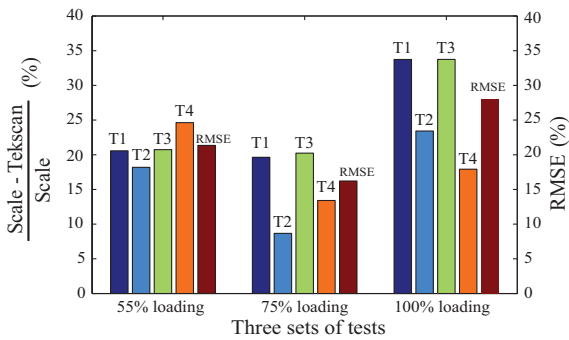


Figure 4.5: Comparison of measurements from the conveyor scale and the Tekscan sensor.

Note: For each loading level, four trials (T1, T2, T3, T4) were performed, and the root mean square error (RMSE) was calculated.

33.7 percent for the measurements from the Tekscan pressure sensor. The RMSE ranges from 16.2 percent to 28 percent. The inaccuracies of measurement results corroborate the findings of other researchers [i.e. (Brimacombe et al., 2009; Drewniak et al., 2007; Gao and Wang, 2013)]. The inaccuracies of measurements by the Tekscan sensor are acceptable for an in-situ dynamic applications to provide qualitative information for the purpose of scientific research.

For the four trials under the 55 percent loading level, small variations between trials can be observed. Meanwhile, large variations of measurement results can be seen for trials under the 75 percent and 100 percent loading levels. The variation may be accounted for the limited activation of sensels at the edge of the Tekscan sensor pad, as depicted in Figure 4.3 (b).

There are four potential reasons for the measurement errors by using the Tekscan tactile pressure sensor. One possibility is that the measurement range of the sensor pad is too high compared to the actual pressure level during the tests which means that the accuracy of the sensor may not meet the expected one. Another potentiality is that the rubber pad which is used to protect the sensor may affect the output of the Tekscan pressure sensor as Rose and Stith (2004) discovered in their experiments. Thirdly, the opening and closing of the belt during conveyance provided a very poor contact between the sensor pad and the belt. The last possibility is the misalignment of the belt during the experiment. Though the Tekscan sensor pad was placed in the center of the conveyor belt at the beginning of each trial, the belt was observed to misalign during the running.

On the other hand, the instrumented idler apparatus is applied to compare the normal forces on the WBSs and the CBS. The pressure mapping in Figure 4.5 was divided into three sections, the Left Wing Belt Section (LWBS), the Center Belt Section (CBS), and the Right Wing Belt Section (RWBS). The division of the pressure matrix was based on the length of the rolls. The resultant LWBS matrix consists of 1-12 columns of the pressure matrix, while the CBS matrix consists of 13-36 columns and the RWBS matrix consists of 37-48 columns. In addition, the mean values and standard deviations of the pressure in the LWBS, CBS, and RWBS were calculated separately. The pressure which is more than 2 standard deviation away from the mean value was filtered out. The pressure in each section is summed up and compared with the normal forces measured by the instrumented idler apparatus (the weight of the empty belt was subtracted).

Table 4.3 compares the results from the instrumented idler apparatus and the Tekscan pressure sensor. In general, the results for the CBS from the Tekscan pressure sensor correlate reasonably well with the results from the instrumented idler apparatus. However, the Tekscan results for the WBSs are much lower than the measurements of the instrumented idler apparatus. The reasons for the differences have been discussed previously in the comparison between the conveyor scale and the Tekscan pressure sensor (i.e. limited activation of sensels in the Tekscan sensor).

4.4.2 Post-process scheme

Preliminary experimental results in Section 4.4.1 indicate that the percentage of error from the Tekscan pressure sensor varied from 8.7 percent to 33.7 percent, which is a rather large error range. Since no satisfying customized calibration process has been found, a post-process scheme has been developed in MATLAB. The post-process scheme is to compensate the low read-out of measured results, and to average the output of the sensor.

Table 4.3: Comparison of measurements from the instrumented idler apparatus and the Tekscan sensor.

	Tekscan pressure sensor							Instrumented idler apparatus		
	Tests	NFLWBS		NFCBS		NFRWBS		NFLWBS Force (N)	NFCBS Force(N)	NFRWBS Force (N)
		Force (N)	Error (%)	Force (N)	Error (%)	Force (N)	Error (%)			
55% loading level	T1	68	28.9	285.4	8.5	34.1	48.8	95.7	312	66.6
	T2	67.1	29.9	294.8	5.5	36.8	44.7			
	T3	64.8	32.3	287.5	7.9	32.6	51			
	T4	68	28.9	266.7	14.5	33.7	49.4			
75% loading level	T1	111.6	24.6	346.7	12.5	84.1	22.4	148	396.3	108.4
	T2	122.8	17	397.1	-0.2	92.9	14.3			
	T3	133.4	9.9	332.3	16.1	71.9	33.7			
	T4	120.5	18.6	381.9	3.6	76.1	29.8			
100% loading level	T1	102.9	48.3	431.8	13.3	40.3	75.7	199.2	498	166
	T2	143.3	28.1	460.6	7.5	69.1	58.4			
	T3	173.4	13	441.7	11.3	79.8	51.9			
	T4	180	9.6	447.6	10.1	103.9	37.4			

Note: For each set of test, four trails (T1, T2, T3, T4) were performed. NFLWBS – Normal Force on the Left Wing Belt Section; NFCBS – Normal Force on the Center Belt Section; NFRWBS – Normal Force on the Right Wing Belt Section; the values from the instrumented idler apparatus are the mean values of the four trials for each loading capacity; error is derived by comparing the measurement of the force using the Tekscan pressure sensor with the measurements of the force using the instrumented idler apparatus.

A compensation factor is applied to compensate the low read-out of raw measurements from the Tekscan pressure sensor. Palmer et al. (2009) provided an assessment of tactile pressure sensors for geotechnical applications. They utilized the same sensor as we used in this research. From their research, we noticed that the measurements from the pressure sensor presented linearity in a low loading range. Due to the fact that the sensor was under a very low loading level, a linear compensation factor is considered to provide adequate accuracy. By comparing the measurements from the conveyor scale and the tactile pressure sensor in terms of the bulk weight within one idler spacing (Figure 4.5), a constant compensation factor of 1.4 was applied to all raw results of the tactile pressure sensor. This may indicate a systematic deviation exists for the measurement of the pressure on the belt by using the tactile pressure sensor. Table 4.4 shows the comparisons between the compensated results of Tekscan data and measurements from the conveyor scale.

Table 4.4: Comparisons of bulk weight between compensated Tekscan data and the conveyor scale.

Loading Level (%)	Trial 1		Trial 2		Trial 3		Trial 4 (N)		conveyor scale (N)
	weight (N)	error (%)	weight (N)	error (%)	weight (N)	error (%)	weight (N)	error (%)	
55	451.4	2.8	464.3	0	449.3	3.2	427.6	7.9	464.3
75	628.6	0	713.1	-13.4	616.9	1.9	671.3	-6.8	628.7
100	725.1	12.4	847.1	-2.3	738	10.8	914.2	-10.4	827.8

Note: error is derived by comparing the weight from the Tekscan pressure sensor with the weight from the conveyor scale.

Furthermore, an averaging algorithm which averages the pressure at each sensel with surrounding eight sensels was also applied to smooth the output of the sensor. Figure 4.6 and 4.6 show the distribution of the pressure at each sensel before and after the averaging algorithm separately. From the comparison between Figure 4.6 and 4.7, it can be seen that the high peak pressures were largely eliminated. The pressure was distributed more evenly. Another benefit is that much more sensels were considered to produce output after applying the averaging algorithm compared to the number of raw sensels. This overcomes the drawback that some sensels failed to register the pressure.

Figure 4.8 illustrates a typical 3D distribution of the normal pressure within two idler spacings after applying the re-arrangement and post-process scheme. Compared to Figure 4.4, relative high peaks can still be observed at the idler junctions. One possible explanation is that the pressure at idler junctions is exaggerated by the folding behavior of the thin sensor pad and the rubber cover sheet forced by the trough shape of the idler sets. Another possibility is the impact of the idler junction gap. The conveyor belt may bend at the idler junctions. The idler junction bending of the belt induces additional compression in the belt's top cover and the high pressure captured by the Tekscan pressure sensor.

In Figure 4.8, the pressure on the CBS is not evenly distributed. In fact, two "mountains" of high pressure can be observed following the idler junctions. Between the two "mountains", the pressure is relatively low. The two "mountains" of the pressure may be interpreted due to the excessive deformation of the belt by the bending at the idler junctions.

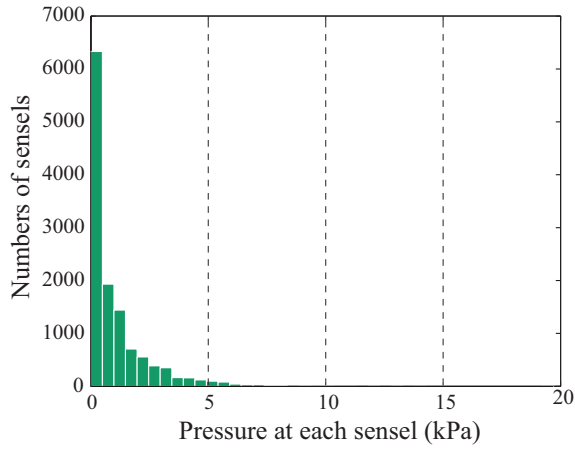


Figure 4.6: Distribution of the raw measured pressure.

Note: The number of sensels within pressure range 10-20 kPa is too small to be visualized in the figure.

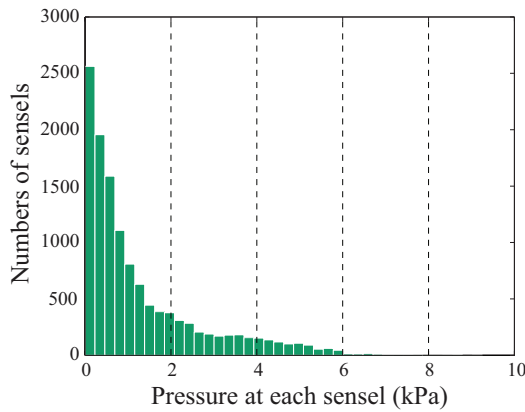


Figure 4.7: Distribution of the pressure after post-process.

Note: The number of sensels within pressure range 6-10 kPa is too small to be visualized in the figure.

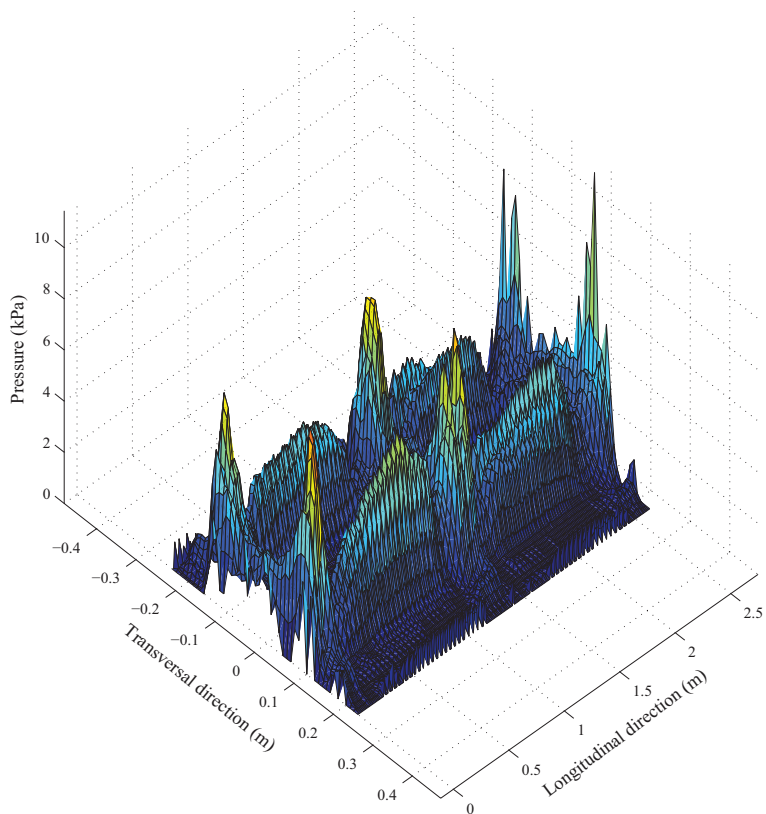


Figure 4.8: Typical 3D distribution of processed normal pressure within two idler spacings.

The phenomena of the pressure in Figure 4.8 correlate with the findings of Zhang (2015). He defined an idler junction bending area as an area along the belt travel direction and separates the belt's contact with the center roll and the wing roll (Figure 4.9). From a finite element analysis, Zhang (2015) recognized that high level of compression can occur to the belt's top cover around the idler junction bending area, and excessive tension may occur to the bottom cover. This reconfirms the two "mountains" of the pressure along the belt travel direction as shown in Figure 4.8. In addition, he also recognized that the contact pressure at the idler junction can be much higher than the rest of the contact area between the belt and the idler due to the impact of the cords and the edge of the center roll and the wing rolls. This gives an explanation of the "peaks" of the pressure at the idler junctions in Figure 4.8.

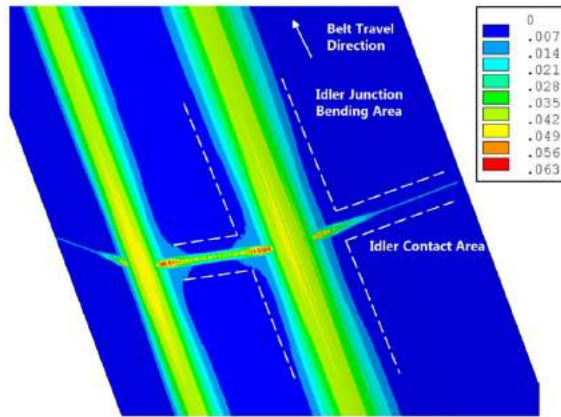


Figure 4.9: Equivalent strain in the belt bottom cover of a steel cord belt from finite element modeling, derived from Zhang (2015).

Zhang (2015) further summarized that the main factors that influence the belt bending at the idler junctions are the trough angle, belt thickness, the bulk load, idler spacing and convex and concave curves. In addition, the impact can be more serious for a fabric belt with low transverse stiffness as the belt used in this study compared to a steel cord belt because the belt can form a small bending curvature by the idler junction and experience high "peaks" of compression in the top cover in the idler bending area. The bending curvature can be so small that the belt may contact the edge of the center roll and the wing roll (Figure 4.10). This leads to excessive contact stress within the belt junction area of the belt.

Figure 4.11 depicts the comparison of percentage of the total normal force on the LWBS, CBS and RWBS under different loading capacities. The total normal forces were calculated by summing up the pressure in each section, and multiplying the corresponding area. Generally, the percentage of the normal force on LWBS and RWBS increases with growing capacities, meanwhile the percentage of the normal force on the CBS decreases. In Figure 4.11, the percentage of the normal force on the LWBS varies from 16.8 percent up to 23 percent, and the percentage for the CBS changes from 74.2 percent to 66.2 percent, while the percentage for the RWBS alters from 8.5 percent to 10.8 percent. The difference between the LWBS and RWBS is due to the misalignment of the belt during experiments.

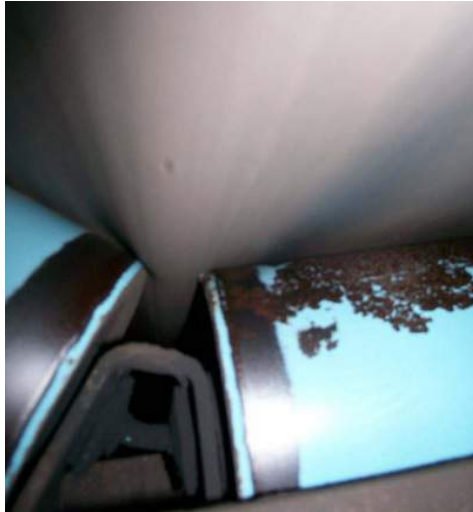


Figure 4.10: The belt contacting the edge of idler rolls, derived from Zhang (2015).

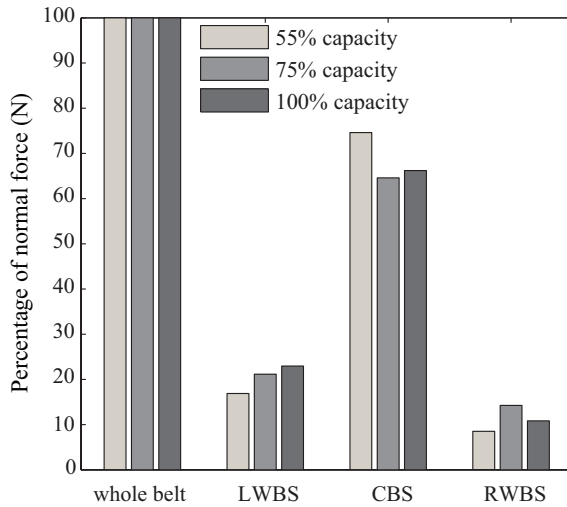


Figure 4.11: Comparison of the normal forces in different belt sections.

4.4.3 Comparisons of experimental and theoretical results

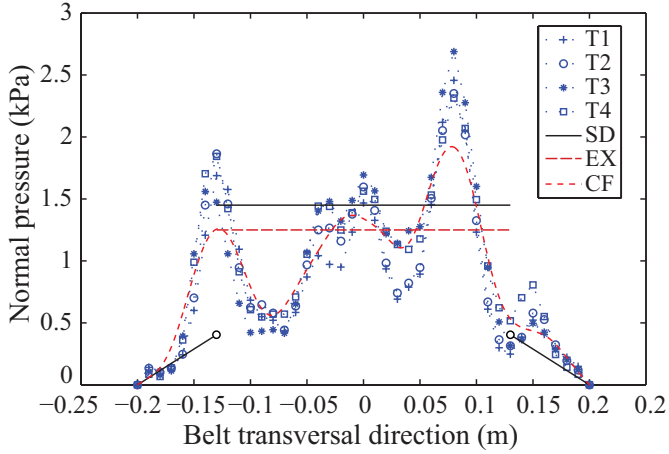
Figure 4.12 shows the transverse distribution of the measured bulk load at 55 percent loading level of the conveyor in (a) active stress state and (b) passive stress state, together with the calculated bulk load from the SD model. The origin of the horizontal axis is set at the center of the belt. Active and passive stress states are determined by considering the stress state of the bulk material on the WBSs. Following the assumption in Chapter 3, it is considered that active stress occurs within the first half idler spacing, while passive stress exists in the second half. Therefore the pressure matrix derived from the re-arrangement scheme is divided into two equal halves to represent active and passive pressure. The measured results (markers in Figure 4.12) are achieved by the mean value of the active or passive pressure matrix. In addition, a curve fitting (CF in Figure 4.12) is achieved after applying the moving average and the smoothing spline fitting technique in MATLAB. The window size of the moving average technique is set as 5. The same techniques are applied in Figure 4.13 and 4.14.

In Figure 4.12 (a), The pressure on the LWBS and RWBS is rather low because there is little bulk material on the WBSs for 55 percent loading level of the conveyor. The measured pressure on the CBS is rather high with a double hump shaped distribution from the curve fitting (CF in Figure 4.12). Two peaks can be observed from the measured results, the left peak (1.3 kPa) is located at the left idler junction, and the right peak (1.9 kPa) occurs on the CBS close to the right idler junction. The two pressure peaks are most likely due to the effect of folding behavior of the sensels facing the idler junctions plus the idler junction bending of the belt as discussed in subsection 4.4.2. Therefore, the pressure peaks in Figure 4.12 are not considered to represent the actual pressure on the belt junctions caused by the bulk material.

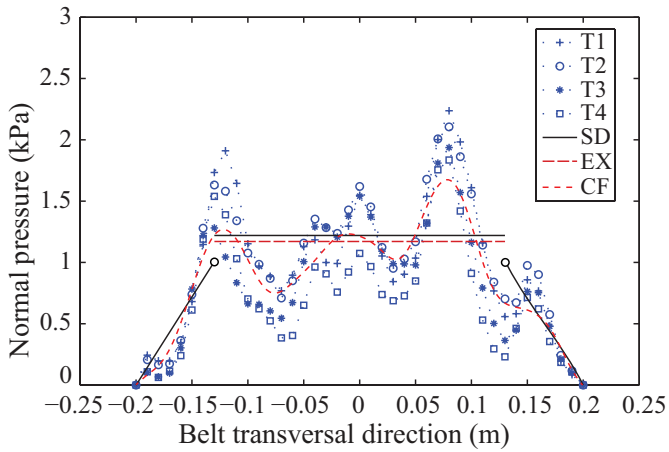
In Figure 4.12 (a), a reasonably good agreement can be observed between the measurements and the calculated result from the SD model. The measured pressure on the CBS shows large deviations, especially at the idler junctions. On contrary, the SD model considers that the pressure on the CBS is equally distributed while does not take the idler junction bending into account. It remains unclear to what extent the idler junction bending influences the measured pressure at the belt junctions. In this case, a mean value of the measured pressure on the CBS (EX in Figure 4.12) is retrieved and compared to the calculated pressure from the SD model (SD in Figure 4.12). The calculated pressure (1.5 kPa) on the CBS from the SD model is close to the mean value of the measurements (1.2 kPa). The measured and calculated normal pressure on the LWBS and RWBS correlate well.

Figure 4.12 (b) shows the distribution of the bulk load from experimental measurements and the SD model in passive stress state. A similar pattern of the pressure distribution as Figure 4.12 (a) can be observed. For the measured pressure on the LWBS, it increases to about 1.2 kPa at the left idler junction while the calculated passive pressure on the WBSs from the SD model grows to 1 kPa at the idler junctions. The measured pressure on the CBS presents a double hump shaped distribution varying from 0.75 kPa to 1.7 kPa from the curve fitting. The mean measured pressure on the CBS is 1.19 kPa while the calculated pressure from the SD model is 1.22 kPa. As a result, a good correlation is achieved between the measurements and the calculated results from the SD model.

Comparisons between Figure 4.12 (a) and (b) indicate that there is no significant difference between measured active and passive pressure on the belt at the 55 percent loading level. Another observation is that the SD model overestimates the pressure on the CBS in



(a)



(b)

Figure 4.12: Transverse distribution of the bulk load at 55 percent loading level from experimental measurements and the SD model in (a) active stress state and (b) passive stress state.

Note: T1, T2, T3, T4 are four trials, SD represents predictions from the SD model, EX represents the mean pressure on the CBS from measurements, and CF represents the result of curve fitting.

both active and passive stress states.

Figure 4.13 illustrates the transverse distribution of the measured bulk load and the calculated bulk load from the SD model at 75 percent loading level of the conveyor in both active and passive stress states. Regarding the distribution of the measured bulk load, a hump shaped distribution of the pressure can be observed in Figure 4.13 (a) and (b). Again, pressure peaks are observed at the idler junction area due to the folding behavior of the sensels and the idler junction bending of the belt. The measured normal pressure on the LWBS in Figure 4.13 (a) increases to a maximum of 1.9 kPa when approaching the left idler junction. From the curve fitting, the measured pressure on the CBS (CF in Figure 4.13) presents a variation between 0.7 kPa and 2.8 kPa, with a mean pressure of 1.6 kPa (EX in Figure 4.13). The calculated bulk load on the CBS from the SD model is 1.9 kPa. The measured pressure on the RWBS presents a small peak in the middle of the RWBS. The reason for that remains unclear.

In Figure 4.13 (b), a reasonably good correlation between the measured and calculated bulk load on the LWBS and CBS is achieved. The calculated bulk load from the SD model correlates with the measured pressure distribution on the LWBS quite well. The calculated pressure (1.6 kPa) from the SD model on the CBS is very close to the mean value of the measurements (1.5 kPa). The measured and calculated bulk load on the RWBS is hardly comparable due to the unexpected peak of pressure.

Comparisons from Figure 4.13 (a) and (b) indicate that a reasonably good agreement between the measurements and the results from the SD model is achieved. For the normal pressure on the WBSs in both active and passive stress states, the SD model produces lower value compared to the experimental measurements. On contrary, the SD model overestimates the pressure on the CBS compared to the measurements.

Figure 4.14 shows the distribution of the measured and calculated bulk load at 100 percent loading level of the conveyor in both active and passive stress states. Again, a hump shaped pattern is recognized from the curve fitting for the distribution the bulk load from the experimental measurements. In Figure 4.14 (a), the measured bulk load on the LWBS grows smoothly from the edge to the idler junction, reaching the maximum value of 2 kPa at the left idler junction. Another measured pressure peak of 2.9 kPa is observed near the right idler junction. In Figure 4.14 (b), a similar pattern of the pressure distribution can be observed, with two pressure peaks reaching 2.1 kPa and 3 kPa respectively. These pressure peaks are most likely caused by the idler junction bending of the belt and further exaggerated by the folding of the sensor pad in the idler junction area, rather than caused by the bulk load.

From Figure 4.14, the SD model correlates reasonably well with the measurements in both active and passive stress states. In Figure 4.14 (a), the calculated pressure on the WBSs from the SD model is lower than the measurements in four trials. If the pressure peaks are averaged with the pressure at the rest of the CBS, the measured pressure on the CBS has a mean value of 1.6 kPa [EX in Figure 4.14 (a)] while the calculated pressure from the SD model is 2.5 kPa [EX in Figure 4.14 (b)]. In Figure 4.14 (b), the calculated and measured bulk load achieve a good agreement. For the pressure distribution on the LWBS and RWBS, the measured pressure and the calculated pressure correlate quite well. For the mean pressure on the CBS, the measured pressure (1.6 kPa) is close to the calculated pressure (1.9 kPa) from the SD model. Though the SD model correlates reasonably well with the measurements, it has to be mentioned the SD model overestimates the pressure on the CBS in both active and passive stress states. Another observation is that the

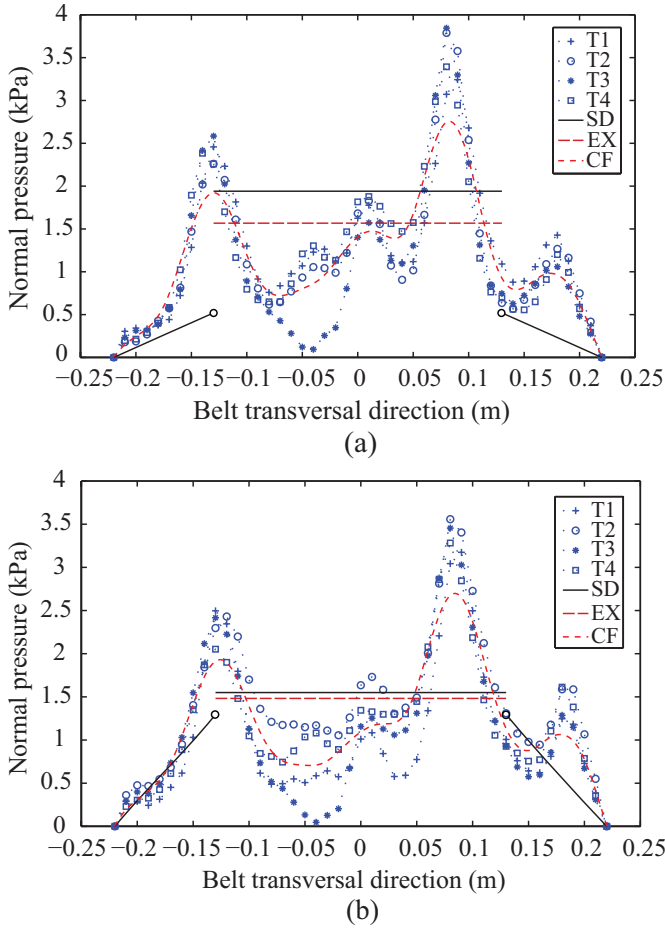
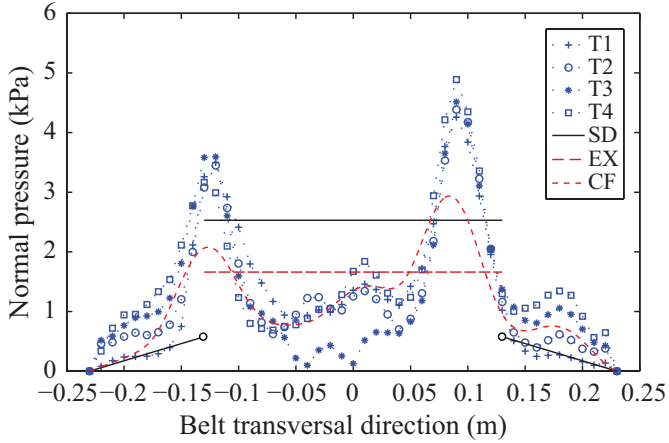
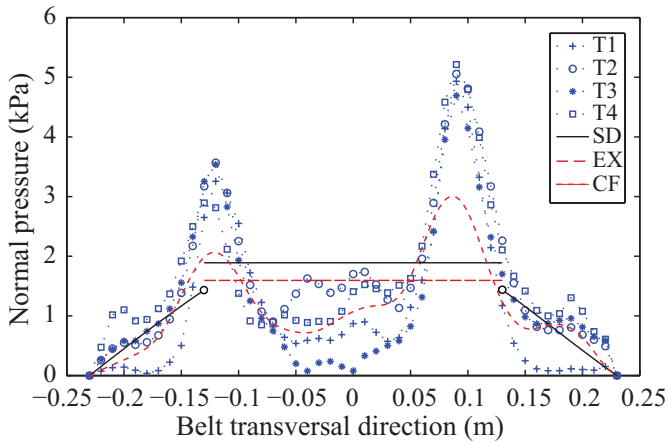


Figure 4.13: Transverse distribution of the bulk load at 75 percent loading level from experimental measurements and the SD model in (a) active stress state and (b) passive stress state.

Note: T1, T2, T3, T4 are four trials, SD represents predictions from the SD model, EX represents the mean pressure on the CBS from measurements, and CF represents the result of curve fitting.



(a)



(b)

Figure 4.14: Transverse distribution of the bulk load at 100 percent loading level from experimental measurements and the SD model in (a) active stress state and (b) passive stress state.

Note: T1, T2, T3, T4 are four trials, SD represents predictions from the SD model, EX represents the mean pressure on the CBS from measurements, and CF represents the result of curve fitting.

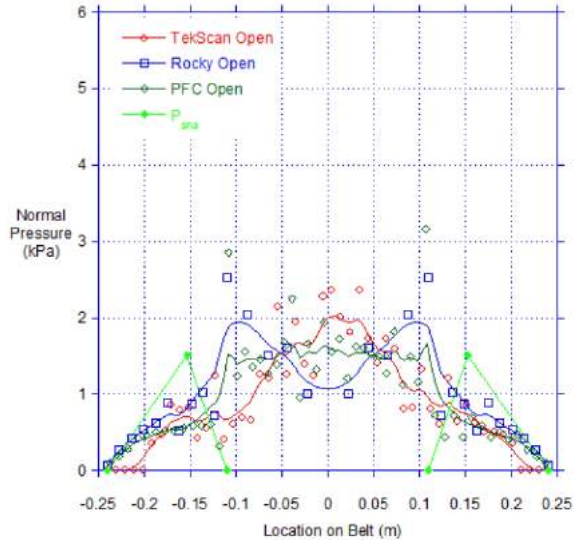
measured results from four trials have some dispersion. The dispersion may be attributed to the noises of the measurements.

The pattern of the pressure distribution in Figure 4.14 is reconfirmed by Ilic (2013) with Tekscan measurement results of the pressure on a belt simulation test facility and on a standstill conveyor belt caused by river sand. From the measured pressure on the belt simulation test facility (Figure 4.15), it can be seen that the pressure peaks cannot be noticed in active stress state while in passive stress state small pressure peaks also exist. However, from the measurements of the pressure on the standstill conveyor belt [Figure 6-10 in Ilic (2013)], the pressure peaks can be hardly observed at the sections of the belt at the idler (passive stress state), but can be clearly observed at the belt sag section (active stress state).

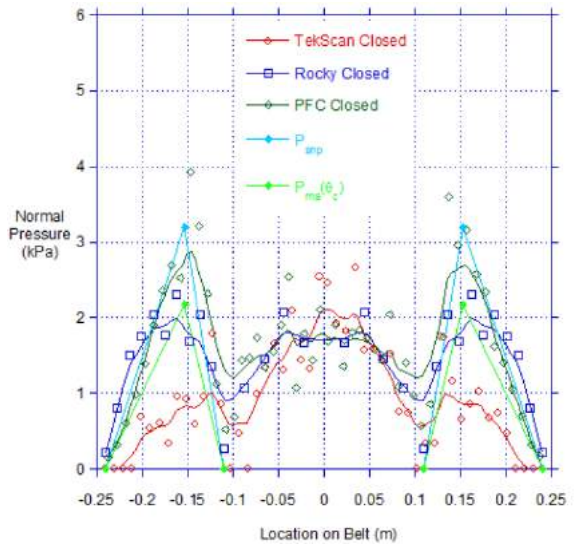
As a result, the Tekscan pressure sensor is considered to capture the belt behavior (bending and impact stress) at the idler junctions into the measurement of the bulk load on the running conveyor belt. Since the SD model does not take the belt behavior into account, the comparisons of the results from the SD model with the Tekscan measurement results cannot provide quantitative conclusions.

4.5 Conclusions

This chapter introduces the experimental study on direct measurements of the bulk load on a running conveyor belt by applying a tactile pressure sensor. The percentage of error for the measurements from the tactile pressure sensor varied from 8.7 percent to 33.7 percent. A filtering and post-process scheme was developed to process the data. Comparisons reveal that the tactile pressure sensor is able to provide qualitative insight of the bulk load distribution for scientific purpose. However, the measurements of the tactile pressure sensor provide limited quantitative information on the transverse distribution of the bulk load due to its intrinsic limitations (i.e. sensitivity and the susceptibility to curves) and the belt behavior at idler junctions observed in this study. This prevents the measurements of the tactile pressure sensor from being compared with results from the SD model in quantitative details. An experimental study on a steel cord conveyor belt is recommended to investigate the influence of the belt behavior at idler junctions on the measurement of the bulk load by using tactile pressure sensors.



(a)



(b)

Figure 4.15: Transverse distribution of the bulk load from a belt simulation test facility in (a) belt opening/active stress state and (b) belt closing/passive stress state, derived from Figure 5-34 (Ilic, 2013)

5

EXPERIMENTAL CONDITION MONITORING OF IDLER ROLLS

Idler rolls will eventually fail to function due to deterioration. In Chapter 1 it was stated that the detection of idler roll failures is important to ensure the reliability of a belt conveyor. Chapter 2 asserted that the detection can be achieved by applying condition monitoring techniques. Solutions for the condition monitoring of the idler rolls are under development. However, the choice of monitoring parameters in these solutions is arbitrary. This chapter aims to investigate which parameters can represent the technical condition of idler rolls. Section 5.1 reviews the development of condition monitoring of belt conveyor idlers. Section 5.2 presents a laboratory experimental study on the detectability of certain monitoring parameters with respect to idler rolls in both incipient and final failure stages. Section 5.3 shows a preliminary in-situ experimental study on the field application of selected sensors. Section 5.4 provides some conclusive remarks.

5.1 Condition monitoring of the idlers

Idler maintenance can be divided into three categories of activities: condition monitoring, decision making, and roll replacement. Condition monitoring is defined as the continuous or periodical inspections and the interpretation of inspection results to indicate the condition of an item (Sharpe and Leaney, 1999). The inspection refers to the act of checking or testing in order to collect a qualitative and/or quantitative description regarding the item. The decision making refers to the process of achieving decisions on when to inspect the next time and/or when to replace the item. The roll replacement encompasses all maintenance tactics that are associated with replacing an idler roll.

There are four types of maintenance strategies for belt conveyor systems: preventive maintenance, random maintenance, corrective maintenance, and predictive maintenance (Lodewijks, 2003). Pang (2010) prompted five steps towards automated maintenance of belt conveyor systems according to the level of automation. Out of the five steps, this section categorizes the development of condition monitoring of belt conveyor idlers into

three steps:

- human sensory inspection and interpretation;
- sensor assisted inspection and human interpretation;
- automated inspection and interpretation.

5.1.1 Human sensory inspection and interpretation

In this practice, the condition monitoring of idlers consists of periodical inspections by human conveyor inspectors through “eye watching” and “ear listening” as shown in Figure 5.1 (Owen, 1997; Leonida, 2013). The content of the inspection is to check whether a certain idler roll makes serious noise, shows excessive wear, or stops running (Tomskey, 1985). Based on such qualitative inspections, the conveyor inspectors can achieve subjective interpretation on the condition of the idler rolls. This practice can still be found on most conveyor sites (Lodewijks, 2003).



Figure 5.1: Manual inspection of belt conveyor idlers, figure courtesy of Martin Engineering (2014).

The advantages of this practice are high flexibility and low infrastructure investment. The conveyor inspectors are considered to easily adjust their inspection routine if necessary. On the other hand, this practice exclusively relies on human labor on most conveyor sites, so there is no need of extra infrastructure for the idler inspection.

The disadvantages of this practice include substandard inspection, arbitrary interpretation, labor intensiveness, inefficiency, and high total maintenance cost. Human sensory inspection can be inaccurate and inconsistent (Lodewijks and Ottjes, 2005b). The interpretation of inspection results also varies significantly according to the knowledge and experience of conveyor inspectors (Surtees, 1995). Moreover, conveyor inspectors are normally requested to repeat the daily routine to spot failed rolls, which is time consuming. The total maintenance cost can be very high considering the high labor cost, and the cost of unplanned downtime due to overdue detection of idler roll failures.

5.1.2 Sensor assisted inspection and human interpretation

In this practice, the inspection is carried out by conveyor inspectors with the assistance of sensors while the interpretation of measurement results remains to be done only by

humans. The deterioration of roll bearings involves the evolution of certain parameters such as the temperature, vibration, and acoustic emission (Niebel, 1994). Sensors which can detect these parameters are utilized to assist conveyor inspectors, for instance (Health and Safety Executive, 2004):

- thermometry sensors (i.e. infrared sensors and thermocouples),
- temperature transition identification techniques (i.e. heat sensitive paints),
- thermal imaging sensors (i.e. infrared cameras),
- noise and vibration sensors (i.e. accelerometers and microphones).

Applications of these sensors for the idler monitoring are qualitatively reported in a limited number of publications, while quantitative results of these applications are very rare. A merged visual-infrared image fire detector was developed to monitor the temperature of idler rolls and pulleys (Fernandez et al., 2013). Bearing failures were simulated by drilling into bearings and then introducing sand into the bearings, or alternatively by heating a roll purposely up to 150 °C. The results show the effective detection of hot spots on the failed idler rolls by the detector over certain distances. However, the accuracy and the area of interest of the detector were not provided. In addition, the temperature evolution of idler rolls at different failure stages was not analyzed.

Acoustic sensors are also applied to assist idler roll inspection. For instance, SKF (2012) has developed the idler sound monitoring kit to assist conveyor inspectors to spot idler rolls which generate abnormal sound. However, the representation of the technical condition of idler rolls by using the sound monitoring kit has not been reported.

A test bench based on vibration measurement was developed to examine detached garland idler rolls (König and Burkhard, 2013). It is stated that the vibration measurement is capable to detect bearing failures. However, the test bench is also reported to be over sensitive even to slight imbalance of the driving wheel. Furthermore, the vibration measurement shows “disturbances” from the sealing system instead of the bearings, which also exists during the normal operation of idlers. The test bench is limited to inspect detached rolls instead of on-site rolls.

The advantages of the sensor assisted inspection include improved accuracy, quantitative information, and less downtime. With the assistance of sensors, conveyor inspectors are able to collect data and to achieve objective interpretations. This will lower the probability of unnoticed idler roll failures and therefore reduce breakdowns of belt conveyors.

Meanwhile, this practice still requires a large amount of human labor and knowledge. It necessitates large involvement of conveyor inspectors to conduct periodical inspections. Guidelines on how to utilize sensors properly to derive accurate inspection results are still missing.

5.1.3 Automated inspection and interpretation

In this practice, inspections of idler rolls are conducted fully by sensors and the acquired data is also transferred into information automatically. Depending on the mobility of applied sensors, there are mobile and fixed monitoring systems.

Mobile monitoring systems

A mobile monitoring system may consist of multiple sensors, one or multiple robot manipulators, and a moving base. One example is the robotic idler prediction system (Figure 5.2). The system consists of a thermal imaging sensor for idler roll inspection, sensors for robot positioning, a six-axis robot manipulator, and a track. It is stated that the system is capable of automatically positioning itself at a required location along a conveyor, scanning appointed idlers rolls, and transferring imaging data to the central control system for further analysis (Scott Automation & Robotics, 2014). However, there is no quantitative information that can show the effectiveness of the thermal imaging sensor for the detection of idler roll failures.

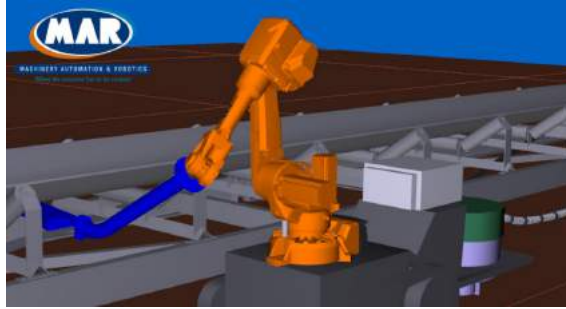


Figure 5.2: Robotic idler prediction system, figure courtesy of Scott Automation & Robotics (2014).

One advantage of mobile monitoring systems is that they are more flexible than fixed monitoring systems. Without much permanent infrastructure, it is easier for a mobile monitoring system to be transferred from one belt conveyor to another.

The drawback of such systems can be that the inspection cycle is longer than that of fixed monitoring systems. The positioning of a robot for the inspection of a certain idler roll may take quite some time. In addition, mobile monitoring systems can only provide periodic inspections. Economic comparison of these automated monitoring systems is difficult to be carried out as there is hardly sufficient information on the cost regarding idler maintenance (Thieme, 2014).

Fixed monitoring systems

In a fixed monitoring system, sensors are permanently installed on idler rolls. Data is acquired and transferred to the central control system continuously or periodically. Three examples of fixed monitoring systems are addressed as follows.

The first example is the "Smart Idler" (Figure 5.3). The "Smart Idler" is an idler roll equipped with a temperature sensor and a RFID node (Lodewijks et al., 2007). The "Smart Idler" may utilize batteries or a self-power electromagnetic mechanism to harvest energy for the sensors (Pang and Lodewijks, 2011). The "Smart Idler" enables continuous monitoring of the temperature of idler rolls and real-time data transferring. Commercialization of such "Smart Idlers" start to emerge, for instance Vayeron Pty Ltd (2013) claim their "Smart Idler" equips a wireless device that will perform temperature, vibration and acoustic measurements which is fitted into an idler roll.

The second example is a fiber optic-based distributed temperature sensing system (Figure 5.4). The fiber optic cable is fixed to idler brackets to monitor the temperature.



Figure 5.3: The "Smart Idler" at the RFID Laboratory of Delft University of Technology (Pang and Lodewijks, 2011).

Yang (2014) stated that the system is capable to spot a failed roll by justifying the assumption that the temperature of idler brackets can represent the condition of installed rolls. During his test the shaft end of a wing roll was heated up to 100 °C (ambient temperature is 32 °C), but the fiber optic cable only measured approximately 2.5 °C extra temperature increase at the bracket with the heated roll than other brackets with normal rolls. This means either the sensitivity of the system is very low or the temperature of idler brackets cannot represent the condition of idler rolls. Fiber optic-based distributed temperature sensing systems are reported to have been installed in underground belt conveyor systems for early detection of hot idler rolls. Fiber optic-based distributed temperature sensing systems are reported to have been installed in belt conveyors for the early detection of hot idler rolls which may cause fire (Vogel, 2011; Grzybek, 2011).



Figure 5.4: Fibre optic-based distributed temperature sensing system, derived from Yang (2014).

The third example is a fixed monitoring system using vibration sensors. Intium Solutions (2014) has developed a roll condition monitoring system which utilizes accelerometers to measure the vibration of idler frames in order to examine the condition of idler rolls. Wireless sensor nodes are also applied to transfer the data to the central control sys-

tem. However, there is no quantitative report on the effectiveness of the accelerometers on the detection of idler roll failures.

In summary, the existing condition monitoring of belt conveyor idlers mainly relies on the conveyor inspectors which is costly, inconsistent and periodical. The utilization of sensors to assist manual inspection and further automated monitoring solutions are under development. However, the choice of sensors in these solutions is still arbitrary. The reason is that suitable monitoring parameters are still uncertain. Therefore, laboratory and in-situ experimental studies are conducted to investigate which parameters among the temperature, vibration and acoustic emission can represent the technical condition of idler rolls.

5.2 Laboratory idler experiments

The focus of the laboratory idler experiments is on the detectability of roll bearing failures at two stages, the incipient and final failure stages (referring to Section 2.4). Roll bearings at the incipient failure stage have small defects, while those at the final failure stage have serious damages. A variety of sensors was applied to measure the temperature, vibration and acoustic emission of the rolls in order to examine which parameters can be used to detect idler roll failures.

Section 5.2 is structured as follows. Subsection 5.2.1 introduces the design of the test rig. Subsection 5.2.2 presents the preparation of idler rolls with different types of defects and damages. Subsection 5.2.3 introduces the selected sensors. Subsection 5.2.4 introduces the installation of the sensors on the test rig. Subsection 5.2.5 illustrates the procedures of the experiments. Subsection 5.2.6 presents the data analysis and results.

5.2.1 Design of the test rig

The test rig (Figure 5.5) consists of a belt conveyor, an idler frame, a control box, and a data acquisition system. The main parameters of the belt conveyor are summarized in Table 5.1. The belt velocity and belt tension can be adjusted.

Table 5.1: Parameters of the belt conveyor.

Parameter	Value
maximum belt speed (m/s)	1.8
type of conveyor belt	EP 500/3
belt width (mm)	1080
central length (mm)	3000

The idler frame (3 in Figure 5.5) is capable of changing the trough angle up to 15°. A mechanism is designed to adjust the height of the idler frame relative to the conveyor frame. With the installation of load cells underneath the idler frame, the load on the idler rolls by the conveyor belt can be determined.

5.2.2 Inducement of bearing defects and damages

The idler rolls used in the experiments have a shell diameter of 108 mm, shell length of 380 mm, and the diameter of the shaft end is 30 mm. The type of bearing is deep groove



Figure 5.5: The test rig.

Note: 1 is data acquisition system, 2 is control box, 3 is idler frame, 4 is belt conveyor.

single roll ball bearing (6206). The inducement of the bearing defects is summarized in Table 5.2. Four samples are prepared for each type of roll. The rolls with bearing defects are prepared by Rulli Rulmeca S.p.A., Italy.

In Table 5.2 two types of defect bearings can be distinguished. For one type of defects (roll code B, C and D), a specific component (i.e. the inner raceway) of the bearing is damaged. For the rest, it is not possible to determine the exact location of the induced defect.

The inducement of the damages to the idler rolls is presented in Table 5.3. Different damages are induced in order to simulate different levels of failure. The inducement of the damages to the rolls G3, K1 and K2 is similar to the way Fernandez et al. (2013) did.




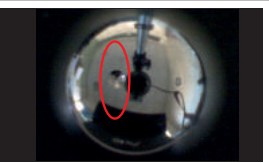




5.2.3 Sensor selection

In order to choose proper sensors, the expected measurement ranges of the temperature, vibration and acoustic emission are estimated and presented in Table 5.4.

Based on the estimated ranges, a variety of sensors is selected and summarized in Table 5.5. For the temperature measurements, thermocouples, infrared sensors and an infrared camera are chosen. Contact sensors like thermocouples may be suitable for fixed monitoring systems, while non-contact sensors (i.e. infrared sensors and infrared cameras) are useful for mobile monitoring systems. Omni- and uni-directional microphones, as well as a sound level meter were used to capture the acoustic emission. Particularly, the uni-directional microphones are capable to collect acoustic emission from the pointed direction while minimizing the background noise. For the vibration measurement, accelerometers with 3-axis sensing capability are selected.

Besides the sensors mentioned in Table 5.5, some accessory sensors including a belt velocity sensor and load cells are also utilized in order to control the test conditions.

Table 5.2: Summary of induced bearing defects.

		
<p>Roll code: A No defect</p>	<p>Roll code: B Outer race defect Defect details: Scratch perpendicular to raceway, width 1 mm, depth 0.5 mm.</p>	<p>Roll code: C Inner race defect Defect details: Scratch perpendicular to raceway, width 1 mm, depth 0.5 mm.</p>
		
<p>Roll code: D Rolling element defect Defect details: damage on one element, diameter 0.5 mm, depth 0.5 mm.</p>	<p>Roll code: E Debris in lubricant Defect details: MICRON+MDA particles, size 0.04 - 0.08 mm, contamination level 5 vol.%.</p>	<p>Roll code: F Radial overloading Defect details: applying 18 kN radial load, duration 0.5-2 hours.</p>
		
<p>Roll code: H No lubrication Defect details: new bearings without any lubricant.</p>	<p>Roll code: I Corrosion Defect details: one week in salty water, one week in air.</p>	

Note: Intact rolls (Code A) are included for reference.



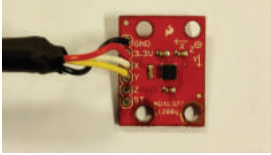




Table 5.3: Summary of induced bearing damages.

		
<p>Roll code: G1 Damage details: dust cover damaged using a hammar</p>	<p>Roll code: G2 Damage details: a hole drilled through the dust cover and seals till the bearing</p>	<p>Roll code: G3 Damage details: three holes drilled into the bearing, filled with metal particles, cage damaged.</p>
		
<p>Roll code: K1 Damage details: five holes drilled into the bearing, cage damaged.</p>	<p>Roll code: K2 Damage details: five holes drilled into the bearing, filled with metal particles, cage damaged.</p>	<p>Roll code: K3 Damage details: covers removed from bearing house, cage damaged.</p>

Table 5.4: Expected ranges of measured parameters.

Physical parameter	Range
temperature (°C)	0 to 100
vibration (g)	± 2
sound level (dB)	30-130

Table 5.5: Summary of the selected sensors.

Temperature sensors	Acoustic sensors	Accelerometer
		
<p><i>thermocouple</i> Model: RS BMS-K-C70-MP Main specifications: range (°C): -50 ~ 250; accuracy (°C): 1; with magnet button.</p>	<p><i>omni-directional microphone</i> Model: CEM-C9745JAD46-2P2.54R Main specifications: range (Hz): 100 ~ 10k; sensitivity (dB): -46±2 at 1kHz Max. input S.P.L: 110 dB.</p>	<p><i>accelerometer</i> Model: ADXL 337 Main specifications: range (g): ±3; nonlinearity: ±0.3%; 3-axis sensing.</p>
		
<p><i>infrared sensor</i> Model: OS35-RS-100C-V10-24V Main specifications: range (°C): 0 ~ 100; accuracy (°C): 1; Field of view: 2:1.</p>	<p><i>uni-directional microphone</i> Model: CEM-C9745JAD46-2P2.54R Main specifications: range (Hz): 100 ~ 10k; sensitivity (dB): -46±3 at 1kHz Max. input S.P.L: 110 dB.</p>	
		
<p><i>infrared camera</i> Model: FLIR AX8 Main specifications: range (°C): -10 ~ 150; accuracy (°C): 2; Resolution (pixels): 80×60.</p>	<p><i>sound level meter</i> Model: ISO-TECH SLM 52N Main specifications: range (Hz): 31.5 ~ 8000; sensitivity (Hz): -37 dB; sound range (dB): 30 ~ 130.</p>	

Note: The datasheets of the sensors can be found in Appendix B.

5.2.4 Sensor installation

Figure 5.6 shows the locations of the sensors installed on the test rig. The shaft ends of the three rolls are named as ShL1, ShL2, ShC1, ShC2, ShR1 and ShR2 respectively. Eight thermocouples are installed on the test rig (No.1 to 8 in Figure 5.6), of which six on the shaft ends, one on the idler frame, and one on the conveyor frame. Six infrared sensors are also installed towards the shaft ends with neglectable distance. In total seven accelerometers are installed, of which six are installed at the shaft ends, one in the middle of the idler frame. Four microphones are installed as shown in Figure 5.6. The infrared camera and the sound level meter will be focused on the shaft end of interest during different sets of experiments.

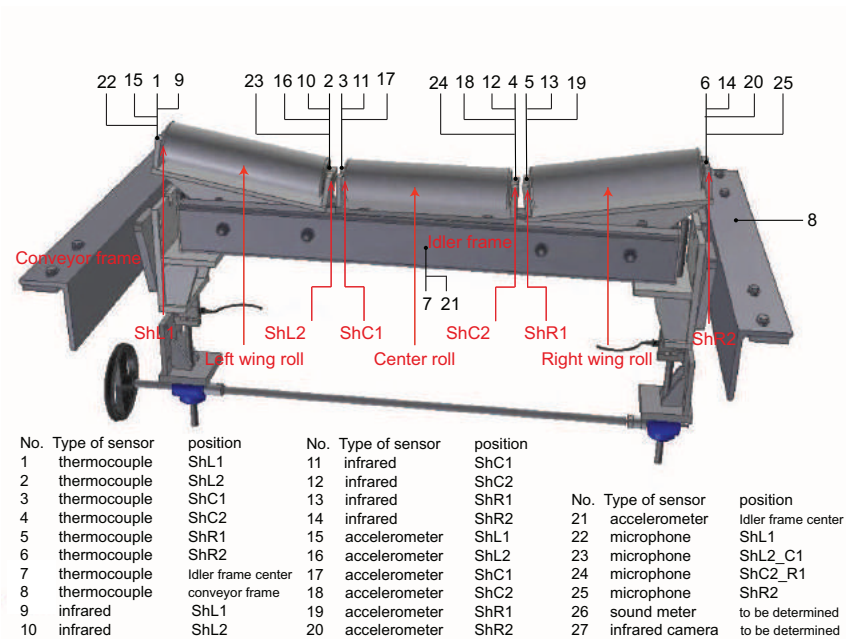


Figure 5.6: Installation locations of the sensors on the test rig.

The sensors at the shaft end ShL1 are taken as an example to explain how the sensors are installed on the test rig (Figure 5.7). The thermocouple is installed on the top of the shaft end using a magnet button. The infrared sensor is installed into a bracket which hosts the shaft end. The accelerometer is bolted onto the shaft end. The X-axis of the accelerometer is set in the horizontal direction, while the Y-axis is set in the vertical direction. Flexible holders with magnetic base are used to hold the infrared camera, the microphone and the sound level meter towards the shaft end ShL1 with a distance of 200 mm, 110 mm, and 200 mm respectively.

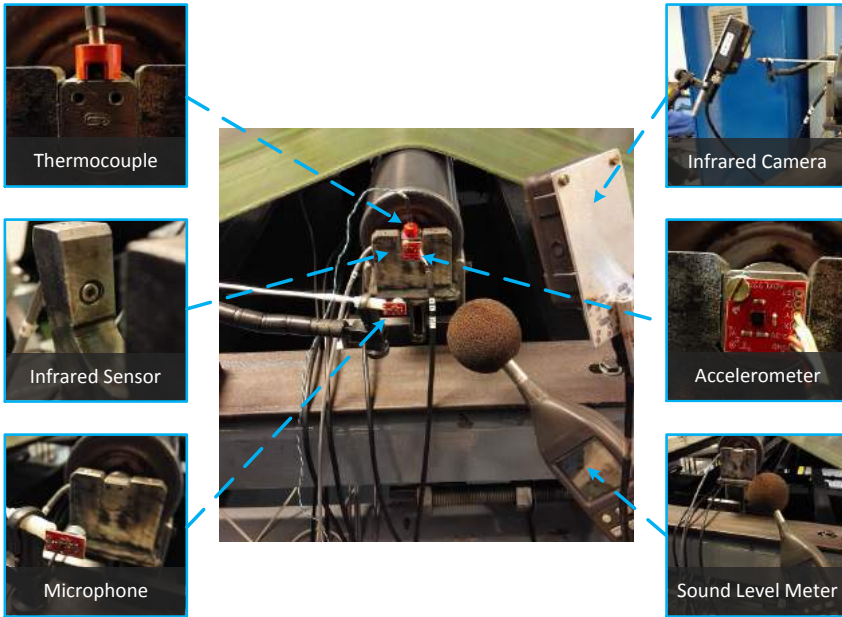


Figure 5.7: Sensor installation at the shaft end ShL1.

5.2.5 Experimental procedures

The first step is to install the rolls on the idler frame. The second step is to install and adjust the sensors. The third step is to apply a certain amount of load on the rolls by tensioning the conveyor belt or adjusting the height of the idler frame. After that, the data acquisition can be initialized and calibrated. The program LabVIEW (Version 11, National Instruments Inc.) is applied for the data acquisition. Figure 5.8 shows the program that has been developed for the laboratory idler experiments. The sampling time and frequency can be adjusted. The analog signal from the sensors is converted by an AD converter. The data can be saved into txt files. After preparing the data acquisition system, the belt conveyor can be started and ran for a certain period of time with a certain belt velocity.

After data acquisition, Matlab (Version 2012B, Mathworks, Inc.) programs are developed to process the data. Depending on the type of signal, time domain and/or frequency domain data processing can be conducted. The frequency domain data analysis applies the Fast Fourier Transform (FFT) technique. In summary, data provided by the Matlab programs are as follows:

- values of the measurements from the thermocouples,
- values of the measurements from the infrared sensors,
- values of the measurements from the infrared camera,
- RMS levels of the measurements from the accelerometers (in X and Y directions),

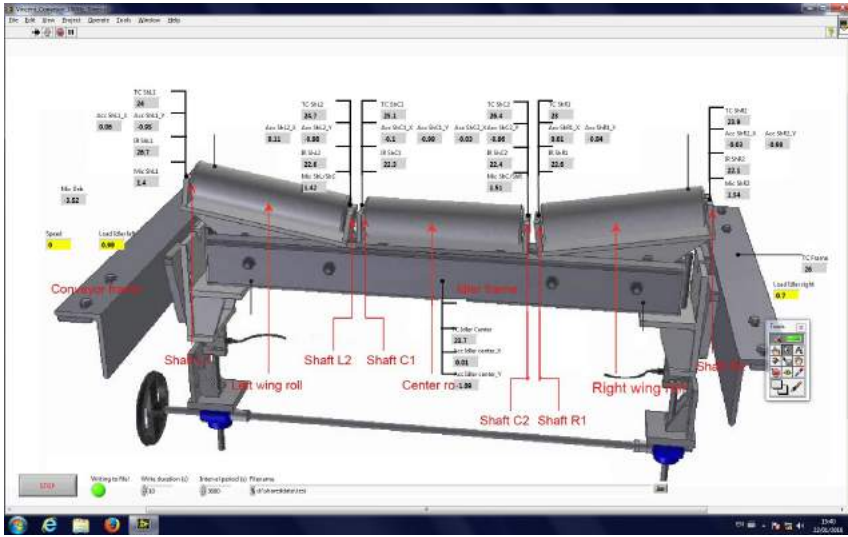


Figure 5.8: LabVIEW interface.

- frequency plots of the measurements from the accelerometers (in X and Y directions),
- frequency plots of the measurements from the microphones.

5.2.6 Results and discussion

Four types of experiments are conducted: a verification test, defect roll tests, damaged roll tests and endurance tests. The verification test is performed to verify the data processing by the developed FFT program and to find out the eigenfrequency of the roll and the idler frame as a whole structure. The verification test (von Bodegom, 2015; Sikkes, 2016) is presented in Appendix C. The defect roll tests are conducted to investigate whether it is possible to detect idler rolls with incipient failures by temperature measurements (using the thermocouples, infrared sensors and infrared camera) and/or vibration measurements (using the accelerometers). The damaged roll tests are carried out to investigate whether it is possible to detect idler rolls with final failures by the temperature (using the thermocouples, infrared sensors and infrared camera), vibration (using the accelerometers) and/or acoustic emission measurements (using omni and uni-directional microphones). The endurance tests are to explore the evolution of the temperature (measured by the thermocouples) of defect rolls and damaged rolls over a reasonably long period of time. A summary of all experiments is presented in Table 5.6.

Defect roll tests

Eight sets of defect roll tests are performed with different levels of load on the idler rolls, in combination with different belt velocities (Table 5.6). The duration of the test for each roll is 120 minutes.

Typical evolutions of the temperature for the defect rolls are shown in Figure 5.9. A regressive pattern can be observed for all three rolls. Another observation is that the

Table 5.6: Summary of laboratory idler experiments.

Type of test	Name	Test conditions			Duration (min×trials)
		Location of bearing of interest	Load on the bearing of interest (N)	Belt velocity (m/s)	
verification test	FFT verification	ShL1	35.0	1.8	10 × 1
defect roll tests	ShC1_1	ShC1	566.0	1.8	120 × 8
	ShC1_2	ShC1	566.0	1.8	120 × 8
	ShC1_3	ShC1	766.5	1.8	120 × 8
	ShC1_4	ShC1	766.5	1.8	120 × 8
	ShC2_1	ShC2	965.1	1.8	120 × 8
	ShC2_2	ShC2	965.1	1.8	120 × 8
	Trough_ShR1_1	ShR1	674.1	1.0	120 × 8
Trough_ShR1_2	ShR1	674.1	1.0	120 × 8	
damaged roll tests	ShL1_G1_1	ShL1	256.6	1.4	120 × 2
	ShL1_G1_2	ShL1	256.6	1.8	120 × 2
	ShL1_G1_3	ShL1	347.5	1.8	120 × 2
	ShL1_G2_1	ShL1	256.6	1.4	120 × 1
	ShL1_G2_2	ShL1	256.6	1.4	120 × 1
	ShL1_G3_1	ShL1	347.5	1.8	120 × 2
	ShL1_G3_2	ShL1	437.5	1.8	120 × 2
	ShR2_K3_1	ShR2	256.6	0.4	30 × 1
	ShR2_K3_2	ShR2	256.6	1.0	30 × 1
ShR2	ShR2	566.0	1.8	15 × 6	
endurance tests	I_A_A	ShL1	42.5	1.0	480 × 1
	I_H_A	ShL1, ShC1	55.6 for I, 117.7 for H	1.2	480 × 1
	B_H_A_1	ShL1, ShC1	55.6 for B, 117.7 for I	1.2	900 × 1
	B_H_A_2	ShL1, ShC1	124.3 for B, 269.8 for H	1.8	900 × 1
	K2_A_K1	ShL1, ShR2	425.8 for K2, 585.8 for K1	1.8	480 × 1
	G3_A_K2	ShL1, ShR2	425.8 for G3, 585.8 for K2	1.8	6000 × 1

Note: The location of the bearing of interest refers to the location of the shaft end as shown in Figure 5.6. The results of the verification test is presented in Appendix B. The utilized sensors in each set of experiments can be traced by the location of the bearing of interest.

starting temperature for each roll is slightly different. It is recognized that the bracket may be warmed up by the previous test. From Figure 5.9 a very small difference is observed between the intact roll A and the defect rolls regarding the temperature increase during the test. The temperature increase of the intact roll A is 6 °C while those of the defect rolls are 7 °C. Considering the accuracy (1 °C) of the thermocouple, it is difficult to distinguish the defect rolls from the intact rolls.

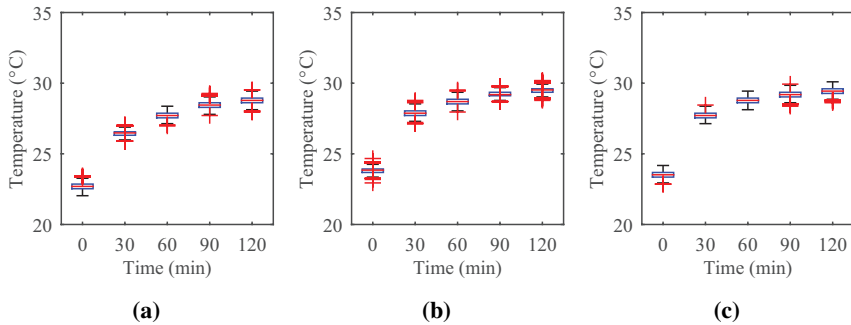


Figure 5.9: Temperature measurements by the thermocouple at the shaft end ShC1 for the roll A (a), roll B (b), and roll F (c) during the defect roll test ShC1_3.

Note: The central mark is the mean value (μ), the edges of the box are the 25th and 75th percentiles, the whiskers present $\mu \pm 2.7\sigma$, in which σ is the standard deviation.

Similar observations apply to the measurements of the infrared sensors and infrared camera. For instance, Figure 5.10 shows the measurements from the infrared sensor and the infrared camera for the roll F during the defect roll test ShC1_3. The measured temperature also shows a regressive pattern of evolution. Compared to Figure 5.9 (c), a small difference exists among the measurements of the thermocouple, infrared sensor and infrared camera. The difference can be attributed to the accuracy of the sensors, and the emissivity of the shaft end as discovered from the emissivity test in Appendix C. However, the difference does not influence the detectability of the sensors as the temperature increase derived from the sensors are investigated separately.

A summary of the temperature increase of the idler rolls during the defect roll tests is presented in Table 5.7. The temperature increase is achieved by subtracting the value of the measurement at 120 minutes by the ambient temperature to diminish the influence of warming-up brackets. In Table 5.7, the defect rolls are generally observed to have a slightly higher temperature increase than the intact rolls. It is considered that the bearing defects induce extra friction during rotating which generates additional thermal energy. However, the difference of the temperature increase is very small. In most tests the difference is just 1 to 2 °C. Considering the accuracy of the thermocouples (1 °C), infrared sensors (1 °C) and infrared camera (2 °C), it is not possible to clarify that the temperature difference is caused by the induced bearing defects or due to the error of measurements.

In a few cases the temperature increase of the defect rolls is distinctly bigger than the intact rolls, for instance the roll I in the test ShC1_3, the roll E in the tests ShC1_4 and ShC2_2 in Table 5.7. However, the distinct difference cannot be consistently observed. For the sample of roll E, it is recognized that the shaft end is substandardly machined. Consequently, abnormal vibration occurs between the shaft end and the bracket and gen-

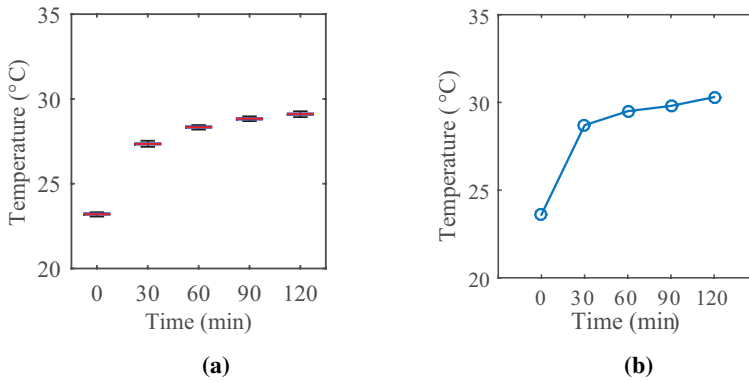


Figure 5.10: Temperature measurements by (a) the infrared sensor and (b) the infrared camera for roll F during the defect roll test ShC1_3.

Note: For Figure 5.10 (a), the central mark is the mean value (μ), the edges of the box are the 25th and 75th percentiles, the whiskers present $\mu \pm 2.7\sigma$, in which σ is the standard deviation.

5

erates additional heat during the tests ShC1_4 and ShC2_2.

Therefore, the temperature measurements with the thermocouples, infrared sensors and the infrared camera are not capable to distinguish the defect rolls from the intact rolls under the test conditions.

Table 5.7: Summary of the temperature increase during the defect roll tests.

Measurements	Test	ShC1_1	ShC1_2	ShC1_3	ShC1_4	ShC2_1	ShC2_2	Trough_ShR1_1	Trough_ShR1_2
	thermocouple measurements (°C)	A	7	5	6	7	6	7	4
B		7	6	7	7	7	7	5	3
C		8	6	7	8	8	5	6	4
D		6	5	8	9	8	6	5	5
E		7	5	8	30	7	19	7	6
F		8	6	7	7	7	7	6	6
H		6	5	8	7	7	7	5	4
I		8	6	9	8	8	7	6	4
infrared sensor measurements (°C)		A	6	4	5	6	6	6	4
	B	7	5	6	7	6	7	5	5
	C	7	6	7	7	8	8	6	5
	D	6	5	7	8	8	6	5	6
	E	7	9	7	26	7	23	7	6
	F	7	6	8	6	7	8	6	7
	H	6	4	8	7	7	7	5	5
	I	8	5	9	7	7	8	6	6
	infrared camera measurements (°C)	A	6	5	7	8	-	7	4
B		7	7	8	8	-	8	5	5
C		8	8	10	8	-	7	5	6
D		5	7	10	9	-	7	5	7
E		6	9	8	22	-	19	6	7
F		6	7	9	7	-	7	6	8
H		6	7	10	9	-	8	5	6
I		7	7	10	8	-	9	7	7

Note: To diminish the effect of the warming up brackets at the beginning of each test, the ambient temperature (measured by the thermocouple on the conveyor frame shown in Figure 5.6) is used as the starting temperature of each test.

Table 5.8: Summary of the RMS levels of the vibration during the defect roll tests.

RMS level		ShC1_1	ShC1_2	ShC1_3	ShC1_4	ShC2_1	ShC2_2	Trough_ShR1_1	Trough_ShR1_2
Tests									
RMS level of horizontal (X) vibration (g)	A	0.16	0.21	0.19	0.20	0.14	0.10	0.17	0.15
	B	0.19	0.20	0.20	0.21	0.13	0.11	0.20	0.13
	C	0.20	0.17	0.21	0.19	0.15	0.11	0.20	0.13
	D	0.18	0.17	0.23	0.20	0.15	0.11	0.18	0.13
	E	0.19	0.17	0.23	0.30	0.15	0.17	0.21	0.14
	F	0.21	0.18	0.23	0.18	0.14	0.11	0.23	0.11
	H	0.19	0.18	0.22	0.20	0.13	0.11	0.16	0.12
	I	0.19	0.18	0.20	0.19	0.14	0.11	0.17	0.12
	RMS level of vertical (Y) vibration (g)	A	1.01	0.99	1.01	1.02	1.01	0.96	0.98
B		1.01	1.00	1.01	1.02	1.01	0.96	0.98	0.91
C		1.01	0.98	1.01	1.02	1.03	0.97	0.98	0.92
D		1.00	0.98	1.01	1.02	1.02	0.96	0.99	0.92
E		1.01	0.99	1.01	1.04	1.01	1.01	0.99	0.93
F		1.00	0.98	1.01	1.02	1.00	0.96	0.98	0.91
H		1.00	0.99	1.01	1.02	1.02	0.98	0.99	0.91
I		1.01	0.98	1.01	1.01	1.01	0.96	0.98	0.91

The analyses of the vibration signal are carried out in both time domain and frequency domain. In the time domain, the RMS level is chosen as it is one of the most widely used parameters to investigate the vibration amplitude of rotating elements (Qiu et al., 2003; Jayaswal et al., 2011). The RMS level X_{RMS} can be expressed as:

$$X_{RMS} = \sqrt{\frac{1}{N} \sum_{n=1}^N |X_n|^2} \quad (5.1)$$

in which N is the total number of samples (200 samples in this analysis) in one calculation, X_n is the n th sample of the vibration measurement.

Figure 5.11 illustrates the RMS levels of the vibration in the horizontal direction acquired by the accelerometer ShC1 for the rolls A, C and F respectively during the test ShC1_3. For each data acquisition, five RMS levels are derived. It can be seen that the RMS levels of the three rolls are all around 0.2 g. There is hardly noticeable difference between the RMS levels of the intact roll and those of the defect rolls.

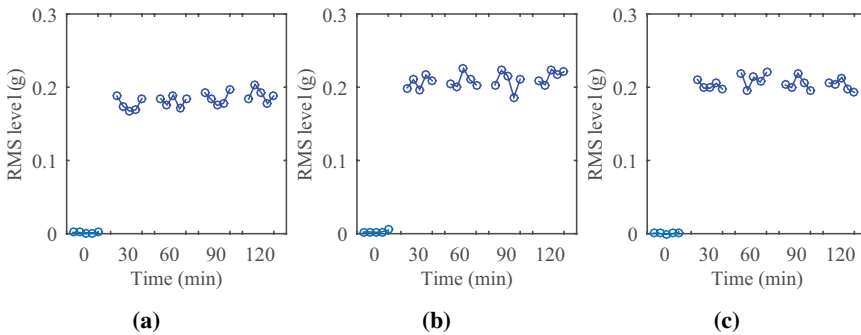


Figure 5.11: RMS levels of the vibration in the horizontal (X) direction for the roll A (a), roll C (b) and roll F (c) during the test ShC1_3.

Note: For each measurement (i.e. 30 min) 1000 samples are acquired and five RMS level are derived as 200 samples are taken for each calculation of the RMS level.

The RMS levels of the rolls during the defect roll tests are calculated and presented in Table 5.8. In general, there is no distinguishable difference between the defect rolls and the intact roll, in both the horizontal and vertical directions. Therefore, it can be concluded that the RMS level is not appropriate to distinguish the defect rolls from the intact rolls.

Besides the time domain analysis, the frequency domain analysis may also provide a potential to detect defect idler rolls, especially for the bearing defects on the inner race (rolls B), outer race (rolls C) and rolling elements (rolls D). It is suggested to check whether the frequencies exhibiting highest levels of vibration energy in the frequency spectrum match the calculated defect frequencies for the rolls B, C, and D respectively. The defect frequencies can be calculated according to the formulas as follows (Harris, 2001):

The defect frequency f_{bo} when the defect is located on the outer race:

$$f_{bo} = \frac{n}{2} f_{rot} \left(1 - \frac{BD}{PD} \cos \gamma_1\right) \quad (5.2)$$

The defect frequency f_{er} when the defect is located on the rolling element:

$$f_{er} = \frac{PD}{2BD} f_{rot} \left[1 - \left(\frac{BD}{PD} \cos \gamma_1 \right)^2 \right] \quad (5.3)$$

The defect frequency f_{bi} when the defect is located on the inner raceway:

$$f_{bi} = \frac{n}{2} f_{rot} \left(1 + \frac{BD}{PD} \cos \gamma_1 \right) \quad (5.4)$$

in which f_{rot} is the rotating frequency of the bearing, n is the number of rolling elements in the bearing (eight in this case), BD is the diameter of the rolling element (0.01m), PD is the diameter of the center of the cage (0.046m), γ is the angle of contact (0 for deep groove bearings in this case).

For a belt velocity of 1.8 m/s, the calculated rotating frequency and defect frequencies, as well as their harmonics less than 50 Hz are presented in Table 5.9.

Table 5.9: Summary of specific frequencies for belt speed 1.8 m/s.

Type of frequency	Corresponding roll code	Frequency and its harmonics (Hz)
rotating frequency	-	5.3, 10.6, 15.9, 21.2, 26.5, 31.8, 37.1, 42.4, 47.7
outer race defect frequency	B	18.7, 37.4
inner race defect frequency	C	29.1
rolling element defect frequency	D	24.5, 49

The time domain data from the accelerometers of all defect roll tests is transferred into frequency plots of vibration energy by applying the FFT program. Figure 5.12 presents the energy spectra of the vibration in the horizontal and vertical directions for the rolls B, C and D during the defect roll test ShC1_4. It can be seen that the energy at 37 Hz is exclusively dominant for the three rolls. 37 Hz can be considered as a harmonic of the rotating frequency (37.1 Hz in Table 5.9) of the bearing. It can also be correlated to the eigenfrequency of the roll and the idler frame as discovered in Appendix C.

For Figure 5.12 (a) and (d), 37 Hz matches the harmonic (37.4 Hz) of the outer race defect frequency. This indicates that the frequency plots may indicate the outer race defect. However, the results of the tests Trough_ShR1_1 and Trough_ShR1_2 contradict this hypothesis. In Figure 5.13, 34 Hz is dominant for the roll B under the belt velocity of 1 m/s. However, 34 Hz does not match any harmonics of the outer race defect frequencies (10.4 Hz, 20.8 Hz, 31.2 Hz and 41.6 Hz after calculation with belt velocity 1 m/s). Therefore, it is not possible to pick up the defect frequencies and their harmonics from the energy spectra of the vibration for the seeded defect rolls B, C, and D.

The influence of changing the idler frame (or the trough angle) on the vibration of the idler rolls is further investigated. For this purpose, the defect roll test Trough_ShR1_1 and Trough_ShR1_2 are carried out by which the wing rolls are set at a trough angle of 12 degree. From Table 5.8, it can be seen that there is no distinguishable difference regarding the RMS levels as the trough angle is changed from 0 to 12 degree.

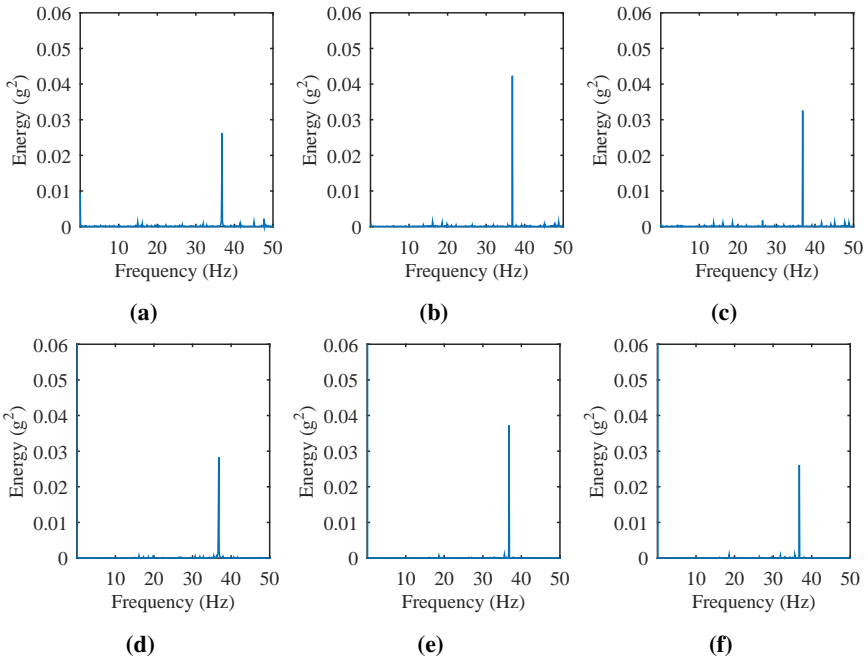


Figure 5.12: Energy spectra of the vibration in the horizontal (X) direction for the roll B (a), roll C (b), roll D (c), and in the vertical (Y) direction for the roll B (d), roll C (e), roll D (f) measured at 120 minutes during the test ShC1_4.

Figure 5.13 shows the energy spectra of the vibration in the horizontal direction for the rolls B, C and D during the test Trough_ShR1_1. It can be seen that the frequency around 34 Hz is dominant for each roll. Comparing with Figure 5.12, the change of the idler frame shifts the dominant frequency from 37 Hz to 34 Hz. This is due to the change of the eigenfrequency of the idler frame with the change of the structure. On the other hand, the energy spectra still cannot provide information regarding the defect type of the rolls.

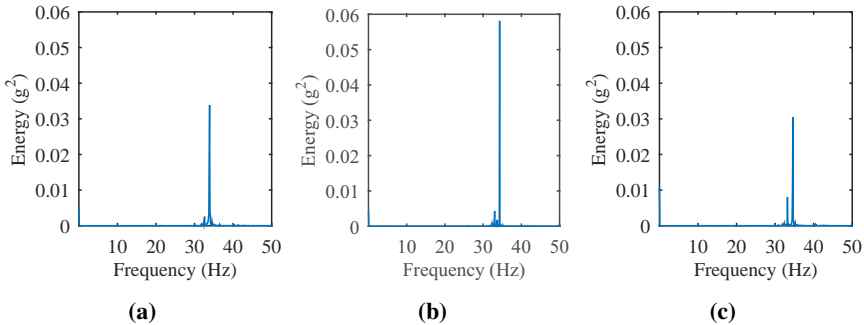


Figure 5.13: Energy spectra of the vibration in the horizontal (X) direction for roll B (a), roll C (b), and roll D (c) measured at 120 minutes during the test Trough_ShR1_1.

Therefore, the vibration measurements in both the horizontal and vertical directions are not able to detect the idler rolls with bearing defects.

From the defect roll tests, it can be concluded that with the used test rig and rolls it is not possible to distinguish a defect roll from an intact roll from the measurements of the temperature and vibration.

Damaged roll tests

In total ten sets of damaged roll tests are performed as shown in Table 5.6. The load on the damaged bearing varies from 256.6 N to 566 N, the belt velocity is in a range of 0.4 to 1.8 m/s. The duration of the test varies from 15 to 120 minutes depending on the purpose of the test. The acquired data from the damaged roll tests will be analyzed with respect to the temperature, vibration and acoustic emission respectively.

Typical temperature evolutions of the damaged rolls from the measurements of the thermocouple ShL1 are presented in Figure 5.14. The temperature of the roll G1 rose up to 66 °C [Figure 5.14 (a)], and the temperature of the roll G3 increased to 63 °C (b) after 120 minutes running time. Compared to Figure 5.9, the damaged rolls show a significant raise in temperature that can be picked up by the thermocouples.

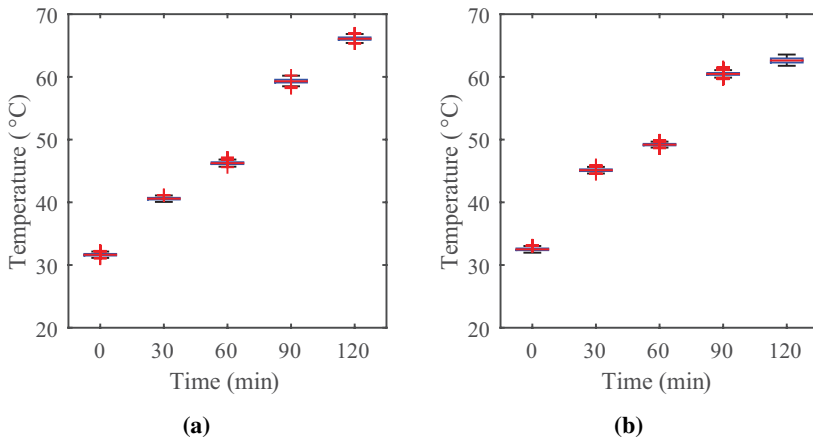


Figure 5.14: Typical temperature evolutions from the measurements of thermocouples, a) trial 2 from the test ShL1_G1_2, b) trial 2 from the test ShL1_G3_1.

Note: The central mark is the mean value (μ), the edges of the box are the 25th and 75th percentiles, the whiskers present $\mu \pm 2.7\sigma$, in which σ is the standard deviation.

Table 5.10: Summary of the temperature increase during the damaged roll tests.

Measurements		Tests							ShR2
		ShL1_G1_1	ShL1_G1_2	ShL1_G1_3	ShL1_G2_1	ShL1_G2_2	ShL1_G3_1	ShL1_G3_2	
thermocouple measurements (°C)	trial 1	23	32	17	21	23	28	18	G1: 18, G2: 20, G3: 18
	trial 2	26	44	19	-	-	40	19	K1: 25, K2: 19, K3: 4
infrared sensor measurements (°C)	trial 1	15	28	13	18	26	22	17	-
	trial 2	17	29	15	-	-	33	17	-
infrared camera measurements (°C)	trial 1	23	-	16	23	24	-	20	-
	trial 2	28	-	19	-	-	-	20	-

Note: To diminish the effect of the warming up brackets at the beginning of each test, the ambient temperature (measured by the thermocouple on the conveyor frame shown in Figure 5.6) is used as the starting temperature of each test.

Table 5.11: Summary of the RMS level of the vibration during the damaged roll tests.

Measurements		Tests							ShR2
		ShL1_G1_1	ShL1_G1_2	ShL1_G1_3	ShL1_G2_1	ShL1_G2_2	ShL1_G3_1	ShL1_G3_2	
RMS level of horizontal (X) vibration (g)	Trial 1	-	0.35	0.37	-	0.33	0.37	0.38	G1: 0.3, G2: 0.32, G3: 0.31
	Trial 2	-	1.02	1.02	-	1.04	1.04	1.04	K1: 0.31, K2: 0.25, K3: 0.3
RMS level of horizontal (Y) vibration (g)	Trial 1	-	0.34	0.35	-	0.34	0.35	0.37	G1: 1.06, G2: 1.05, G3: 1.04
	Trial 2	-	1.02	1.02	-	1.03	1.03	1.04	K1: 1.05, K2: 1.04, K3: 1.05

Note: To diminish the effect of the warming up brackets at the beginning of each test, the ambient temperature (measured by the thermocouple on the conveyor frame shown in Figure 5.6) is used as the starting temperature of each test.

A summary of the temperature increase of the damaged rolls is presented in Table 5.10. It can be seen that all damaged rolls show significant temperature increase during the tests. Therefore, a certain threshold of temperature exists which can distinguish the damaged rolls from the intact rolls. The exact value of the threshold is out of scope of this research.

In Table 5.10, noticeable difference regarding the temperature measurements by the thermocouple, infrared sensor and infrared camera exist. It is largely due to the influence of the emissivity. The emissivity is the measure of an object's capability to emit infrared energy (Raytek Corporation, 1999), with a value which varies from 0 (i.e. shiny mirror) to 1 (i.e. blackbody). The shafts of the idler rolls used in the experiments are made of polished mild steel. The emissivity of the polished mild steel is about 0.1 to 0.35 (Raytek Corporation, 1999). However, the emissivity factor of the infrared sensors is fixed as 0.9. Therefore, the infrared sensors provide measurement results lower than the true values. The emissivity factor of the infrared camera can be changed by the users.

An emissivity test is conducted to investigate the influence of the emissivity on the temperature measurements of the painted shaft end, polished shaft end, and rusted shaft end by the thermocouple, infrared sensor and infrared camera (Appendix D). From the emissivity test, it can be seen that different treatments have influence on the accuracy of the measurements. The painted shaft end provides the most accurate measurements for all three types of sensors. Considering the idler rolls in the field are normally painted for corrosion protection. The sensors are supposed to provide accurate measurements of the temperature. For the polished and rusted shaft ends, the accuracy of measurements may not affect the diagnosis as different threshold values can be chosen for different sensors.

The achievable temperature increase of the damaged rolls may vary significantly according to the loading level and rotational speed. For instance, in an experimental study, Hawksworth et al. (2003) obtained the temperature evolution of a failed roll bearing which steadily rose up to around 100 °C followed by sharp increase to 200 °C within 60 minutes. The failure of the roll bearing in that case was induced by 125 percent axial overloading, 1200 kN radial force, and a rotational speed of 570 rpm.

Due to the limitations of the test rig, the damaged idler rolls in our tests did not achieve so a dramatic temperature increase. However, it can already be concluded from the significant temperature increase in our tests that the temperature measurement is capable to detect the damaged rolls in the final failure stage.

From the perspective of the vibration measurement, the RMS level of the horizontal vibration shows distinct differences between the damaged rolls and the intact rolls. Figure 5.15 (a) and (b) show the RMS levels of the horizontal vibration for the damaged roll G1 and the intact roll A respectively. It can be seen that the RMS level of the damaged roll G1 is around 0.3 g while that of the intact roll A is around 0.15 g. Therefore, the RMS level of the horizontal vibration can distinguish the damaged roll from the intact roll.

A summary of the RMS levels of the damaged rolls is presented in Table 5.11. It can be seen that the RMS levels of all damaged rolls in the horizontal direction are more than 0.25 g. Compared to the RMS levels of the intact rolls and defect rolls in Table 5.8, distinct differences can be observed.

On the other hand, the RMS level of the vertical vibration cannot provide distinguishable differences between the damaged rolls and the intact rolls. The RMS levels of the vertical vibration of the damaged rolls (Table 5.11). are very close to those of the intact rolls (Table 5.8). It is considered that the conveyor belt provides much higher load in the

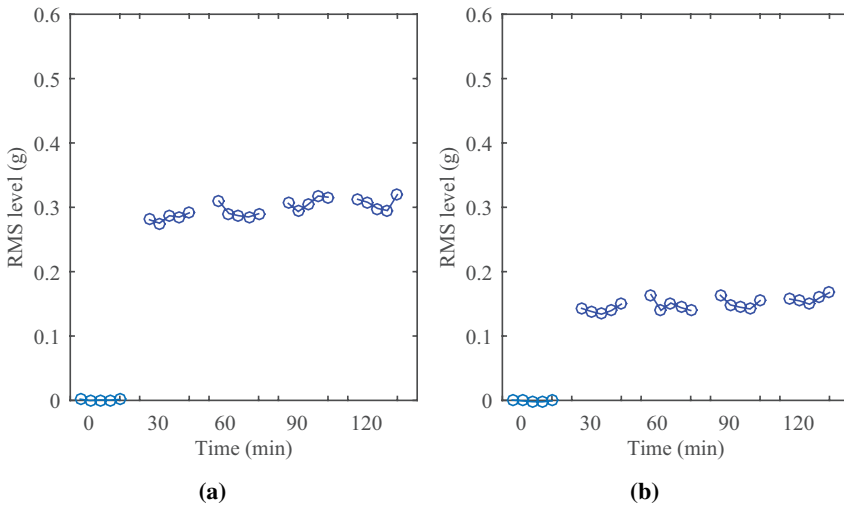


Figure 5.15: RMS levels of the horizontal (X) vibration of the damaged roll G1 (a) and an intact roll A (b) during trial 2 of the test ShL1_G1_2.

vertical direction to the rolls than the horizontal direction. Therefore, the shaft ends of the rolls are pushed against the bracket tightly which makes the bearings very difficult to vibrate in the vertical direction.

The analysis of the acoustic emission of the damaged idler rolls is conducted Audacity (Version 2.1.2) and Matlab. Figure 5.16 shows part (0.04 second) of the recorded audio by the uni-directional microphone in Audacity in which the abnormal acoustic emission from the damaged bearing is highlighted. The audio was recorded during the test ShR2_K3_1. The distance between the damaged roll and the uni-directional microphone is 10 mm. The sampling frequency of the microphone is 30 kHz.

From Figure 5.16, it can be seen that the acoustic emission from the damaged bearing exhibits characteristics of a stimulation following with quick damping (the upper plot), discontinuous sound level (the medium plot), and covering a wide range of frequency (the lower plot). Especially from the lower plot of the spectrogram, it can be seen that the acoustic emission around 3 kHz from the damaged roll has high sound intensity. It can also be noticed that the frequency of the background noise from the engine is mainly less than 1 kHz.

Figure 5.17 shows the acoustic analysis program developed in Matlab. The acoustic analysis program presents the waveform of sound in the time domain and frequency domain. Both bandpass filter and bandstop filter are developed in the acoustic analysis program in order to filter out the background noise and to investigate the characteristics of the audio within certain band width. In addition, an audio player is also integrated in the program to give both audible and visual examination of the signal before and after applying filters.

In Figure 5.17, W1 shows the time waveform of the recorded audio by the uni-directional microphone for the roll K3 during the test ShR2_2. It can be seen that there is no clear pattern due to the background noise. W2 shows the frequency plot of the original signal, in which most background noise is located at the band width less than 1 kHz as

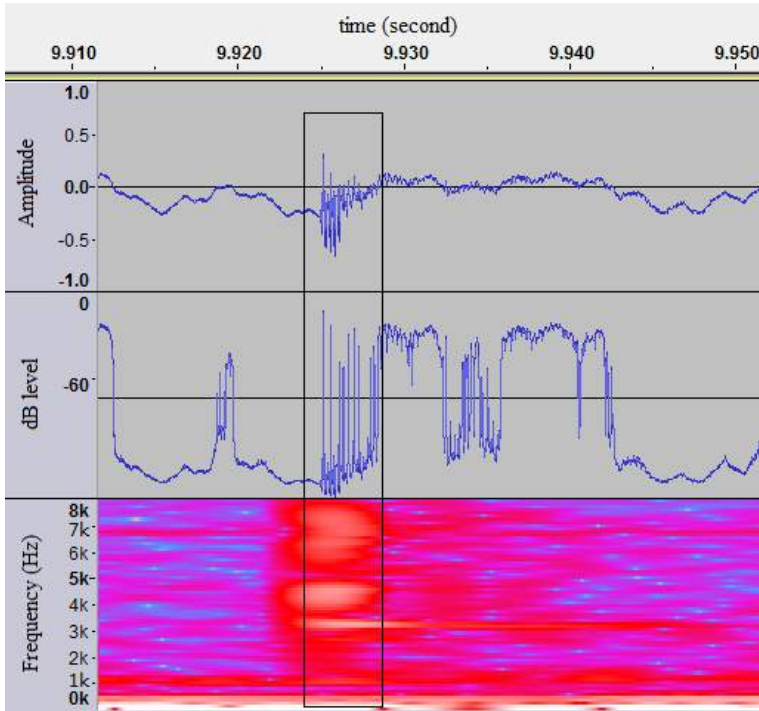


Figure 5.16: Part of recorded audio in Audacity showing abnormal acoustic emission from the damaged bearing of the roll K3, in waveform (the upper plot), dB waveform (the medium plot), and spectrogram (the lower plot).

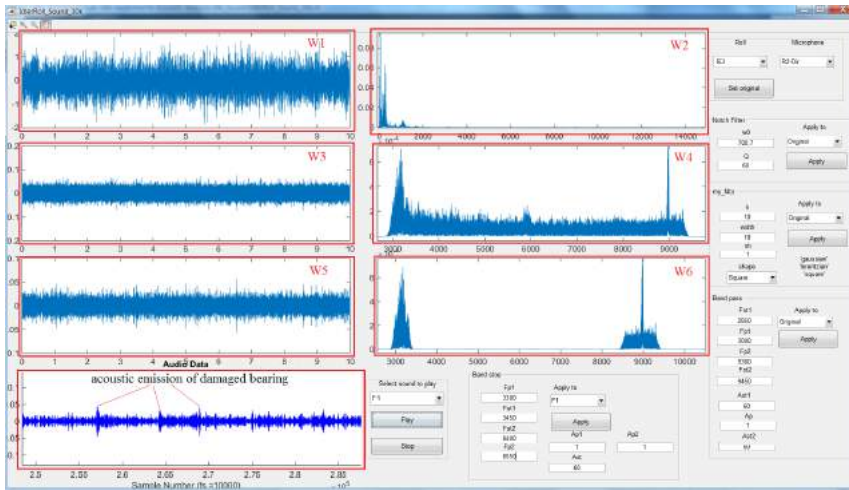


Figure 5.17: The developed acoustic analysis program in Matlab equipped with both band pass filter and band stop filter.

Note: W1 is the waveform of the original signal in time domain, W2 is the FFT plot of the original signal, W3 is the waveform of the signal after the first filter (F1), W4 is the FFT plot of the signal after the first filtering (F1), W5 is the waveform of the signal after the second filter (F2), W6 is the FFT plot of the signal after the second filtering (F2). The window of Audio Data shows the real time signal during play in which the acoustic emission of the damaged bearing is highlighted.

found in Audacity. By applying the bandpass filter (W4), it can be seen that there are two characteristic peaks of sound power, one peak is around 3.1 kHz and the other around 8.9 kHz. Therefore, the band stop filter is further applied which filters out the signal between two peaks (W6). If playing the filtered signal, the acoustic emission from the damaged bearing can be distinguished clearly.

The test Sh_R2 is carried out to compare the detectability and timeliness of the temperature, vibration and acoustic emission measurements for the damaged rolls. From the measurement results (Table 5.10 and 5.11), the detectability of the measured parameters is summarized in Table 5.12. It can be seen that the temperature measurement is able to detect all damaged rolls. The damaged roll K3 only shows a temperature increase of 4 °C because the bearing cover has been removed so the generated heat easily dissipates. The vibration measurement can detect all damaged rolls as the RMS levels of the damaged rolls are higher than that of the intact roll. For the measurement of the acoustic emission, the damaged rolls G3, K1 and K3 are observed distinct audible sound and characteristics in frequency.

To conclude, the temperature, vibration and acoustic emission measurements are capable to detect the damaged rolls at the final failure stage. The measurement results become more apparent for large damages. The selected sensors, including the thermocouples, infrared sensors, infrared camera, accelerometers, and the uni-directional microphone can provide distinct features between the damaged rolls and the intact roll.

Endurance tests

Table 5.12: Summary of detectability of measured parameters for the damaged rolls.

Measurements	Tests		ShL1_G1_1	ShL1_G1_2	ShL1_G1_3	ShL1_G2_1	ShL1_G2_2	ShL1_G3_1	ShL1_G3_2	ShR2
	RMS level of horizontal (X) vibration (g)	Trial 1	-	0.35	0.37	-	0.33	0.37	0.38	G1: 0.3, G2: 0.32, G3: 0.31
Trial 2		-	1.02	1.02	-	1.04	1.04	1.04	K1: 0.31, K2: 0.25, K3: 0.3	
RMS level of horizontal (Y) vibration (g)	Trial 1	-	0.34	0.35	-	0.34	0.35	0.37	G1: 1.06, G2: 1.05, G3: 1.04	
	Trial 2	-	1.02	1.02	-	1.03	1.03	1.04	K1: 1.05, K2: 1.04, K3: 1.05	

Figure 5.18 illustrates the temperature evolution of the intact roll A and the defect roll B over fifteen hours running time. For both rolls, a regressive pattern of temperature evolution can be recognized. After about eight hours, the temperature of the rolls A and B stabilizes at about 28 °C till the end of the test. This reconfirms that there is no distinct difference between the intact roll and the defect rolls in long period of time.

Another endurance test that will be elaborated is the test Endurance_test_G3_A_K2. In this test, the damaged roll G3 is installed on the left wing brackets while the intact roll A is installed on the center roll brackets. Figure 5.19 presents the temperature evolution during the endurance test. From Figure 5.19 (a), it can be seen that the temperature of the shaft end ShL1 (where the damaged bearing locates) increases sharply in the first two hours up to 74 °C. After that, the temperature decreases moderately and stabilizes at around 50 °C. Figure 5.19 (b) shows the temperature evolution of the other shaft end of the roll G3. It can also be seen that the temperature increases quickly in the first three hours up to 37 °C. After that, it maintains at around 35 °C. The temperature of the shaft end ShL2 is much lower than ShL1. Figure 5.19 (c) shows the temperature evolution of the intact roll A. It can be seen that the temperature increases in the first three hours and then maintains at around 30 °C. Comparing the plots (a), (b) and (c), a distinct temperature difference consistently exists during the one hundred hours endurance test. In addition, it is necessary to use two temperature sensors at both shaft ends of an idler roll to ensure reliable detection of either bearing failure. Another conclusion is that the detection of the failed idler rolls can provide sufficient time for arranging roll replacement as the damaged rolls ran at least 100 hours under the test conditions.

5.3 In-situ idler experiments

To further investigate which parameters can represent the technical condition of the on-situ idler rolls, an experimental study is carried out on a bulk terminal belt conveyor.

5.3.1 Experimental setup

The in-situ idler experiments were carried out on a belt conveyor at Rizhao Port, China. The design capacity of the belt conveyor is 7500 t/h, the belt velocity is 3.15 m/s, and the belt width is 1.8 m. Each idler consists of three identical rolls with a roll length of 0.65 m, and the diameter of the roll shell is 0.159 m. The idler spacing is 1 m. The shaft ends of the idlers are painted. An infrared camera and a sound level meter are applied in the in-situ idler experiments to measure the temperature and the acoustic emission of the rolls (Figure 5.20). The distance between the Infrared camera and the roll shaft end is 28 cm, while the distance for the sound level meter is 8 cm.

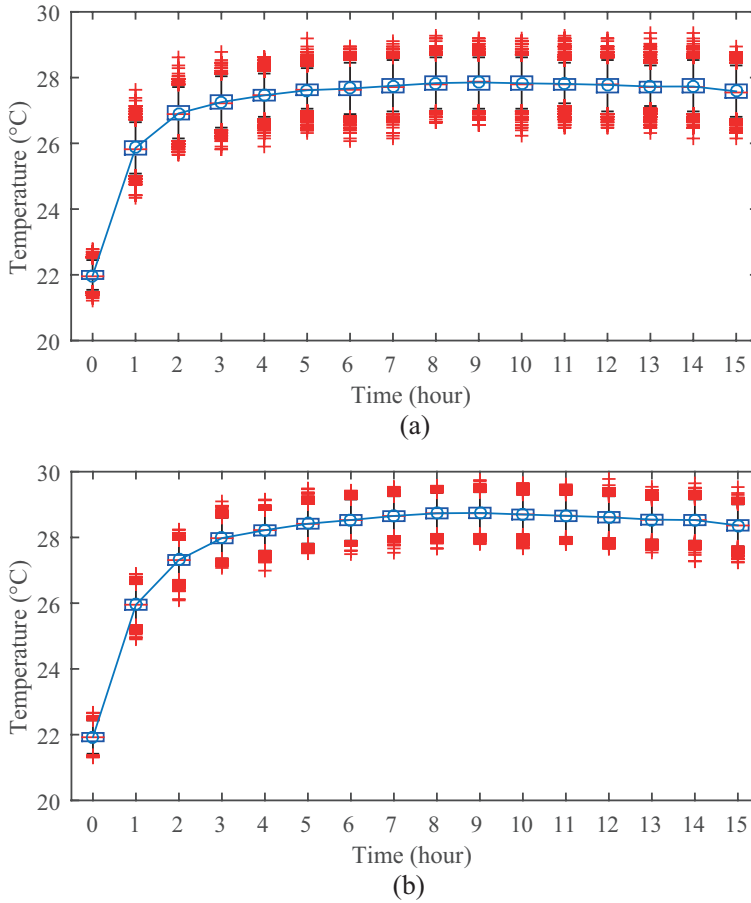


Figure 5.18: The temperature evolution from the test Endurance_test_B_H_A_2, (a) the intact roll A, (b) the defect roll B.

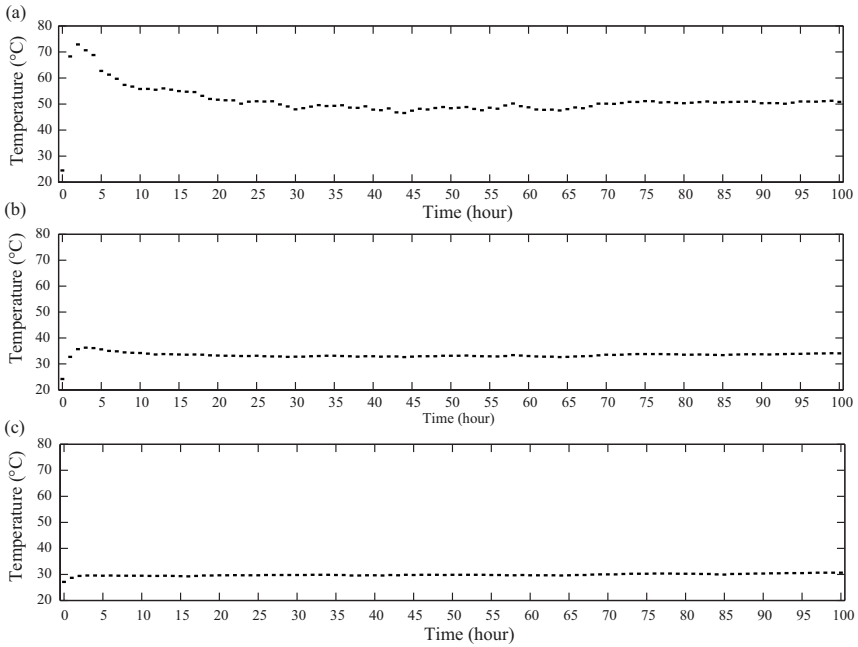


Figure 5.19: Temperature evolution from the test Endurance_test_G3_A_K2, (a) shaft end ShL1, (b) shaft end ShL2, (c) shaft end ShC1.

Note: Shaft end ShL1 is where the damaged bearing of the roll G3 is located, shaft ends ShC1 and ShC2 are of the roll A, shaft end ShR2 is where the damaged bearing of the roll K2 is located.



Figure 5.20: In-situ idler experimental setup.

Ten idler rolls are randomly selected on the belt conveyor to measure the temperature and sound level. The measurements are conducted during the running of the belt with a throughput of 2500 t/h and under constant speed. The ambient temperature is about 25 °C.

After the on-site measurements, the rolls are taken out from the belt conveyor to measure their rotating resistance. Figure 5.21 shows the apparatus for the measurement of the rotating resistance. Each roll is placed on the pivot supports which is constrained from rotating. Two plates are placed on the roll shell to apply a certain radial force and a drive torque to rotate the roll at a given speed. The maximum normal load that the apparatus can apply to the roll is 484 N. The rotational speed of the roll is set to be 600 rpm. For each roll, the running time is 22 minutes. The rotating resistance of the roll is measured by the force to hold the shaft stationary.



Figure 5.21: Idler roll rotating resistance measurement apparatus, figure courtesy of Rizhao Changyun Industry Transport Equipment Co., Ltd.

5.3.2 Results and discussion

Figure 5.22 shows the measurements of the temperature and sound level of the ten random idler rolls. Overall, the temperature varies from 30 °C to 43 °C, and the sound level varies from 81.4 dB to 96.8 dB. By applying the correlation analysis to the ten samples, a coefficient of correlation of 0.76 is derived. The coefficient of correlation S generally varies between -1 and 1. If $S = 1$, a perfect positive correlation between two variables exists while if $S = -1$ it means a perfect negative correlation (Scheaffer and McClave, 1990). Therefore, the coefficient of 0.76 indicates that a positive and strong correlation exists between the temperature and the sound level of the rolls.

Of the ten rolls, the rotating resistance of four rolls is so high that the apparatus cannot provide measurements. Figure 5.23 shows the temperature versus the rotating resistance for the remaining six rolls. A positive correlation between the temperature and the rotating resistance can be observed, with a coefficient of correlation of 0.69. Similarly, a coefficient of correlation of 0.62 is derived between the sound intensity and the rotating resistance for the six idler rolls. Therefore, both the temperature and sound level have positive correlations with the rotating resistance of the rolls.

Furthermore, five rolls of 0, 0.5, 1.5, 2.5, and 4.5 years usage time are selected from the belt conveyor and measured their rotating resistance as in Figure 5.24. It can be seen that the rotating resistance of the new roll is about 5.4 N, while those of the used rolls are around 7 N. In addition, an increasing trend of the rotating resistance along with the

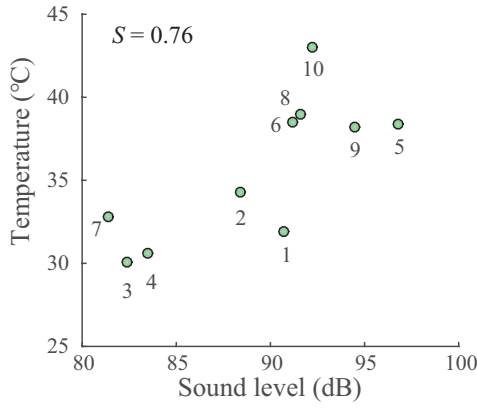


Figure 5.22: Temperature versus acoustic emission for the ten measured rolls.

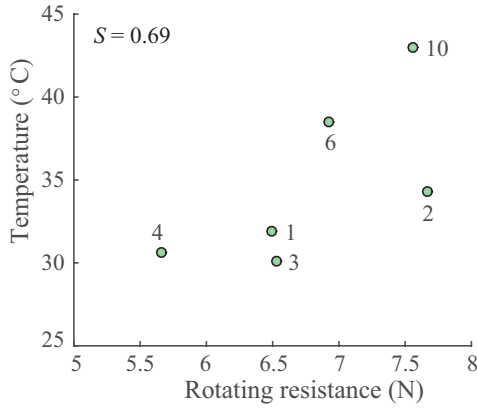


Figure 5.23: Plot of temperature versus rotating resistance for the ten measured rolls.

Note: Markers represent the measurements of the six rolls with numbering after Figure 5.22.

usage age can be observed. Measurements of the rotating resistance of idler rolls over their lifetime were also conducted by Gladysiewicz et al. (2004) on a laboratory idler test rig. From the study it is found that sealing system and grease are two main determinant of the increasing rotating resistance over the lifetime of idler rolls.

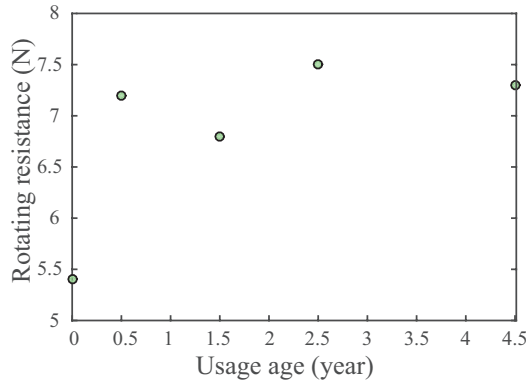


Figure 5.24: The rotating resistance versus the usage age for five idler rolls.

Even though the measured rotating resistance did not show significant increase along with the usage age in this study due to limited loading conditions, one may expect significant increase of the rotating resistance of idler rolls approaching failure in belt conveyors. Gladysiewicz and Kawalec (2010) found that the rotating resistance of idler rolls increases remarkably along with growing radial load on the rolls. Therefore, detection and in time replacement of failed rolls gain benefit of energy saving.

To conclude from the in-situ idler experiments, positive correlations exist between each two of the temperature, sound level and the rotating resistance of the idler rolls. In addition, the rotating resistance of the rolls increases along with the usage time.

5.4 Conclusions

Several conclusions can be drawn from the laboratory and in-situ idler experiments:

- Idler rolls in the final failure stage can be detected. The detection of failed idler rolls can provide sufficient time for arranging roll replacements. However, idler rolls in the incipient failure stage cannot be detected under the laboratory test conditions.
- Measurements of the temperature, vibration and acoustic emission can detect idler rolls in the final failure stage.
- Measurement of the temperature at shaft ends of idler rolls is a straightforward and effective approach to detect idler roll failures.
- The RMS level of the horizontal vibration at the shaft end is an indicator of the final failure of an idler roll.
- The acoustic emission of idler rolls in the final failure stage shows some distinct difference from that of intact rolls within certain band width (between 1.5 kHz and 9 kHz in this case).

- Considering the sensor installation, signal interpretability, and timeliness, the measurement of the temperature is suggested to be the most effective inspection solution.
- Positive correlation exists between the measured temperature, acoustic emission and rotating resistance.

The laboratory idler experiments are limited by the test rig conditions such as the low achievable belt velocity and the load on the idler rolls. Meanwhile, the limited number of measured idler rolls in the in-situ idler experiments can only provide qualitative insight into the relationship among the temperature, acoustic emission, rotating resistance and the usage time of the rolls.

Two recommendations for further research are formulated. The first recommendation is to investigate the threshold value of a certain measurement parameter (i.e. the temperature) for the interpretation on the condition of idler rolls. The second recommendation is to investigate the deterioration rate of idler rolls at different stages and the achievable operating time between the final and catastrophic failure stages.

6

INTEGRATED MAINTENANCE DECISION MAKING

Chapter 2 stated that a theoretical approach to calculate the lifetime or the reliability of a population of idler rolls is available. However, maintenance decision making cannot merely rely on the theoretical calculation because large deviations of the predicted lifetime/reliability exist compared to the reality. Chapter 5 presented experimental studies on the applicable condition monitoring parameters for the idler rolls. Nevertheless, the knowledge for the maintenance decision making is still missing. This chapter aims to explore the option of integrating the theoretical calculation and the condition monitoring for a more accurate maintenance decision making.

6.1 Introduction

Assuming a condition monitoring system is available for the idler rolls within a belt conveyor system, the decisions for the idler maintenance include: the diagnosis on whether a roll has failed, and an answer to the question when to inspect all (or part of the) rolls the next time (the inspection interval). As the monitoring data are always associated with the identities of the idler rolls, the failed rolls can be identified from the diagnoses and be replaced after each inspection assuming that there is a time window for the roll replacement afterwards.

The existing diagnostics techniques for the bearing failures are mostly threshold-based (Heng et al., 2009). A threshold value for the monitoring parameter is presumed to represent a roll bearing failure (Figure 6.1). Diagnosis is conducted in such a way that it is based on whether the value of the monitoring parameter of the roll bearing exceeds the presumed threshold value. In any application, the presumed thresholds are based on empirical experiences or manufacturers' recommendations (Heng et al., 2009). For instance, Owen (1997) claimed a warning threshold for roll bearings can be set at 70 °C, an alarm threshold can be 80 °C, and a failure threshold value of 90 °C. Lodewijks et al. (2007) considered the temperature of a roll bearing reaching 80 to 120 °C is a clear sign of po-

tential failure. In another application, an alarm threshold for the roll bearings is set as 50 °C (Mitteldeutsche Braunkohlengesellschaft mbH, 2015).

In fact, each inspection of the idler rolls provides a sample of the monitoring parameter. From the sample, a relative frequency function (rff) of the monitoring parameter ($f_{t_i}(x)$ in Figure 6.1) can be obtained at each time t_i . From the temporal evolution of the rffs, the process of wear out of the population of bearings can be observed. Assume that the temperature is the monitoring parameter in Figure 6.1, the rff $f_{t_1}(x)$ at time t_1 presents high density in very low temperature region and low density in high temperature region. When it comes to time t_3 , the rff $f_{t_3}(x)$ stretches over low and high temperature regions more evenly. When it approaches the end of the lifetime of the population at time t_i , the rff $f_{t_i}(x)$ is expected to present high density in the higher temperature region.

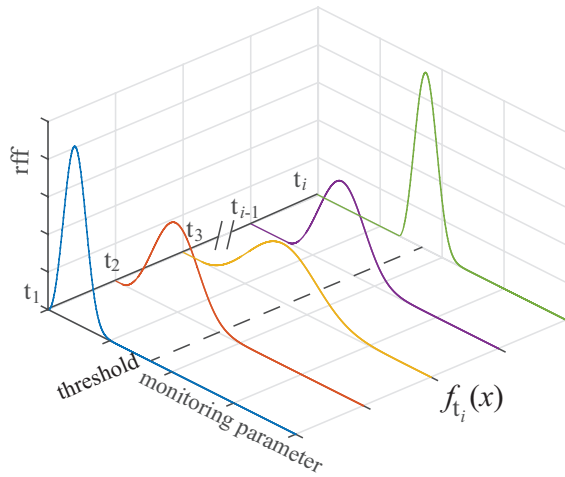


Figure 6.1: Illustration of rffs of a monitoring parameter in temporal sequence.

Facing such an evolution of the monitoring parameter along the aging of the rolls, it is a challenge to determine an appropriate threshold for a given application since it depends on the application (i.e. the load, rotational speed, operational time), the ambient conditions (Lodewijks et al., 2007), and the mode of evolution. In reality, it is often observed that the presumed threshold value is either too high or too low (Goode et al., 2000). If the threshold is set too low, an unacceptable number of false alarms may be triggered which cause a waste of healthy rolls that are replaced too early. On the other hand, roll failures may not be identified in time if the threshold is set too high. So there is a need for the determination of a proper threshold for the sound diagnoses on the roll failures for a given application.

Regarding the determination of the inspection interval, there is no direct method available in literature. The industry empirically sets the idler inspection as daily routine as discovered by Thieme (2014) from a survey of several big conveyor operators. Some idler manufacturers, for instance Douglas Manufacturing Co. Inc. (2011), recommend to listen for unusual sound or vibrations daily while to check wear or stuck rolls weekly.

The L_{10} bearing lifetime theory from Lundberg and Palmgren (1949) is the most widely used to calculate the lifetime or reliability for a population of bearings. However, the theory has not been linked to the determination of the inspection interval due

to the large dispersion from the reality (Tomskey, 1985). Therefore, the question how to improve the accuracy of theoretical calculation of the reliability (or the failure rate) in a given application is of interest. With improved theoretical prediction of the failure rate, the inspection interval can be determined more accurately.

The aim of this chapter is to explore how to achieve accurate maintenance decision making by integrating the theoretical calculation of the failure rate and the real time monitoring data. For this purpose, a framework of integrated maintenance decision making is developed and presented in Section 6.2. Section 6.3 illustrates a case study to present the results of a simulation with the implementation of the framework. Section 6.4 provides some conclusive remarks.

6.2 Framework of integrated maintenance decision making

Figure 6.2 illustrates the framework for the integrated maintenance decision making. The framework takes the real time throughput and belt velocity of the belt conveyor, the properties of the conveyed bulk material, the parameters of the belt conveyor (i.e. the belt width), the operational time, and the acquired condition monitoring data as inputs. The outputs of the framework will be answers to the questions which idler rolls are failed and need to be replaced, as well as when to inspect the idler rolls the next time.

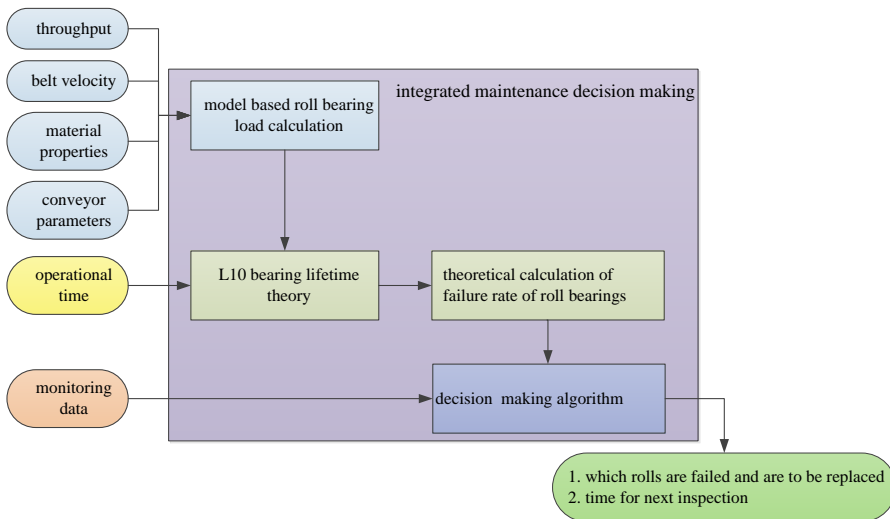


Figure 6.2: Framework of integrated maintenance decision making.

From the top left side of the framework in Figure 6.2, the SD model or the hybrid (SD+KH) model in Chapter 3 can be used to calculate the load on the roll bearings. The load is a critical input for the theoretical calculation of the reliability of the bearings. Following the calculation of the reliability, an estimate of the failure rate of the roll bearings between two consecutive inspections can be calculated.

Meanwhile, from the bottom left side, the condition monitoring can also provide an

estimate of the failure rate of the roll bearings between two consecutive inspections. With a given threshold value, the failure rate can be considered as the percentage of the roll bearings whose values of the monitoring parameter exceeding the threshold.

With the derivation of the failure rates from both the theoretical calculation and the monitoring data, comparisons can be conducted after each inspection. Based on the comparisons of the two failure rates, the theoretical calculation will be amended by introducing an error term, and the threshold value will also be updated. In this way, the integration of the theoretical calculation and the condition monitoring is achieved.

Figure 6.3 shows the algorithm of the decision making in Figure 6.2. It is recognized that the load on the center roll bearings and the wing roll bearings are quite different. The center roll bearings are taken in this chapter to illustrate the algorithm. It is also assumed that there are a number of historical inspections at times t_1, t_2, \dots, t_i available.

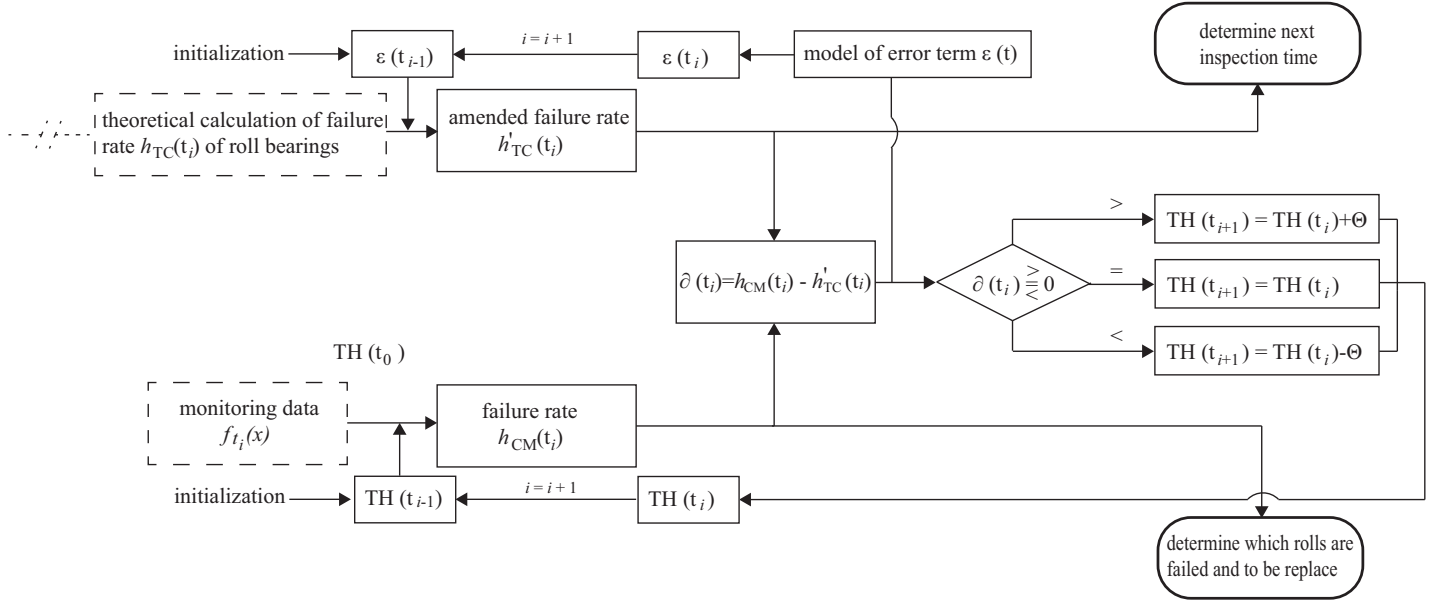


Figure 6.3: Algorithm of the integrated decision making.

To initialize the algorithm, the first step is to calculate the failure rate $h_{TC}(t_i)$ for each inspection. For a population of identical ball bearings under the same working conditions, there is a relationship between the reliability, the rating life L_{10} , and the achieved operational time as shown in Eq. (2.8). Therefore, the cumulative distribution function (cdf) for the failure of the roll bearings is:

$$F_{TC}(t) = 1 - R_B(t) = 1 - \exp\left(-0.1053(L_S(t)/L_{10,m})^{10/9}\right) \quad (6.1)$$

in which $R_B(t)$ is the reliability of roll bearings, $L_{10,m}$ is the L_{10} rating life of the roll bearings according to the design capacity of the conveyor which can be derived from Eq. (2.9), $L_S(t)$ is the achieved operational time and can be calculated as:

$$L_S(t) = \sum_{j=1}^N \left(\frac{P_{NG,j}}{P_m}\right)^3 T_j \quad (6.2)$$

in which $P_{NG,j}$ is the radial force on the center bearing (the axial force is assumed to be zero in straight sections of the conveyor) corresponding to the j th level of the throughput of the conveyor derived from Eq. (3.60), T_j is the corresponding subtotal operational time of the j th level of the throughput and the total achieved operational time $t = \sum_{j=1}^N T_j$, N is the total number of the throughput levels, and P_m is the radial force on the center bearing corresponding to the design capacity of the conveyor derived from Eq. (3.60).

If the throughput and belt velocity of the belt conveyor are kept constant, Eq. (6.2) can be simplified as:

$$L_S(t) = \left(\frac{P_{NG}}{P_m}\right)^3 t \quad (6.3)$$

Being aware that Eq. (2.8) is valid between $R(t) = 0.93$ (correspondingly $L_S(t) = 0.7L_{10}$) and $R(t) = 0.4$ (correspondingly $L_S(t) = 7L_{10}$) as stated by Harris (2001), as well as the deviation between the predicted failure rate and the reality, an error term $\varepsilon(t)$ is introduced into the theoretical calculation of the failure rate between two consecutive inspections at time t_{i-1} and t_i as:

$$h'_{TC}(t_i) = \int_{t_{i-1}}^{t_i} F_{TC}(t) dt + \varepsilon(t_{i-1}) \quad (6.4)$$

With a constant throughput and belt velocity, substituting Eq. (C.1) into Eq. (6.4) generates:

$$h'_{TC}(t_i) = \exp\left(-0.1053\left(\frac{L_S(t_{i-1})}{L_{10,m}}\right)^{10/9}\right) - \exp\left(-0.1053\left(\frac{L_S(t_i)}{L_{10,m}}\right)^{10/9}\right) + \varepsilon(t_{i-1}) \quad (6.5)$$

The next step is to calculate the failure rate $h_{CM}(t_i)$ from the condition monitoring data as:

$$h_{CM}(t_i) = \frac{\text{number of bearings exceeding threshold } TH(t_{i-1}) \text{ at } t_i}{\text{the total number of bearings}} = \int_{TH(t_{i-1})}^{+\infty} f_{t_i}(x) dx \quad (6.6)$$

in which $f_{t_i}(x)$ is the rff of the monitoring parameter at time t_i .

Therefore, the discrepancy $\partial(t_i)$ between $h_{CM}(t_i)$ and $h'_{TC}(t_i)$ can be derived as:

$$\partial(t_i) = h_{CM}(t_i) - h'_{TC}(t_i) \quad (6.7)$$

Given the error terms $\varepsilon(t_0), \varepsilon(t_1), \varepsilon(t_2), \dots, \varepsilon(t_{i-1})$ and the discrepancy $\partial(t_i)$, the error term $\varepsilon(t_i)$ can be calculated. The error terms $\varepsilon(t_0), \varepsilon(t_1), \varepsilon(t_2), \dots, \varepsilon(t_{i-1})$ and the discrepancy $\partial(t_i)$ can be fitted by using an appropriate model (i.e. a linear model, exponential model), depending on the mode of evolution of the deviation between the calculated failure rate and the one from the condition monitoring. With the development of the model, the error term $\varepsilon(t_i)$ can be calculated. The derived $\varepsilon(t_i)$ is further used for the theoretical calculation of the failure rate $h'_{TC}(t_{i+1})$ at time t_{i+1} . It is noted that the parameters of the error term model may be updated after each inspection.

On the other hand, the threshold value $TH(t_i)$ can also be updated by considering the discrepancy $\partial(t_i)$. For instance, if $\partial(t_i) > 0$, then the threshold $TH(t_{i+1})$ can be updated to a higher value for time t_{i+1} (Figure 6.3). On contrary, if $\partial(t_i) < 0$, the threshold $TH(t_{i+1})$ should be updated to a lower value for time t_{i+1} as:

$$TH(t_{i+1}) = TH(t) - \Theta \quad (6.8)$$

in which Θ is the increment of the threshold.

In this framework, the diagnoses on the roll failures is based on the updated threshold. After the inspection at time t_i , the diagnoses are achieved by checking the roll bearings whose values of the monitoring parameter exceed the updated threshold $TH(t_i)$. Either of the two bearings within one roll reaching the threshold value indicates the failure of the roll. The determination of the inspection interval or the time for next inspection is based on the theoretical calculation of the failure rate $h'_{TC}(t_i)$ after introducing the error term (Figure 6.3). A variety of approaches like Fuzzy Logic can be applied (Lodewijks and Ottjes, 2005b; Pang, 2010). The framework considers the inspection of all idler rolls. In fact, the inspection may also be focused on the idler rolls whose values of the monitoring parameter approach the threshold value.

The current framework does not consider the replacement of the rolls. To take the roll replacement into account, one recommended way is to divide the bearings into different groups based on the replacement time. If the amount of roll replacements is big for each time, then each roll replacement event will generate a new group. If the amount of roll replacements is small, then several consecutive roll replacement events produces a new group. For each of these groups, the current framework can still be applied.

6.3 Case study

A simulation case study is conducted to verify the effectiveness of the framework for the integrated maintenance decision making. This case study uses most of the simulation configurations from previous studies by Lodewijks (2003) and Lodewijks et al. (2007). The simulation configurations are summarized in Table 6.1. The simulation is conducted for the whole design lifetime of the belt conveyor. The temperature is selected as the monitoring parameter. The initial threshold value is set as 40 °C at the beginning of the simulation. The center roll bearings are chosen as the object of this simulation study.

Table 6.1: Configurations for the simulation.

Parameters	Values	Parameters	Values
conveyor length (km)	10	idler spacing (m)	2
transported material	coal	number of upper idler frames	5001
design capacity (t/h)	6000	design lifetime of the conveyor (year)	10
throughput (t/h)	5000	operational time (hour/day)	20
belt velocity (m/s)	5	operational days (days/year)	360
belt width (m)	2	roll bearing size	6306
belt weight (kg/m)	93.2	rotational speed of idler rolls (r/min)	600

A belt conveyor with a length of 10 km is chosen for the simulation. The belt conveyor is assumed to transport coal with constant throughput of 5000 t/h. By applying the SD model in Chapter 3, it is obtained that the radial force on each center roll bearing is 2791 N. From the L_{10} bearing lifetime theory, it can be obtained that the L_{10} rating life for the center roll bearings is 33171 hour, which means 10 percent of the roll bearings will fail by this running time.

In order to represent the evolution of the temperature in Figure 6.1, the temperature of the 10002 center roll bearings is randomly assigned in such a way that their rffs present a pattern as illustrated in Figure 6.4. The simulated temperature measurements from each inspection are assumed to follow a normal distribution. When the roll bearings are at their early age (within first 40 months), the mean values of the rffs are in the low temperature region. With the growing age of the roll bearings, the mean value of the rff is increasing while the deviation also becomes slightly larger. During the middle age (41 to 80 months) of the roll bearings, the mean value continues to rise while the variance is kept constant for the simulated temperature measurements. Within the old age (81 to 120 months) of the roll bearings, the mean value of the rff further increases while the deviation becomes smaller. This is to simulate the temperature of old bearings which is concentrated in high temperature region. In this way, the simulated temperature measurements of the inspections represent the hypothetical evolution of the monitoring parameter in Figure 6.1.

For the simulation case study, a constant inspection interval of 1 month is applied. Regarding the error term $\varepsilon(t)$ in the framework in Section 6.2, a linear model ($\varepsilon(t_i) = \alpha_{1,i} + \alpha_{2,i} \cdot t_i$) is considered. A program is developed in Matlab to derive the two parameters $\alpha_{1,i}$ and $\alpha_{2,i}$ based on the error terms $\varepsilon(t_0), \varepsilon(t_1), \varepsilon(t_2), \dots, \varepsilon(t_{i-1})$ and the discrepancy $\partial(t_i)$. The increment of the threshold Θ is set as 0.3 °C during the simulation.

Figure 6.5 illustrates the failure rates from the amended theoretical calculation after introducing the error term, the monitoring data with updated threshold from the framework, and merely applying the L_{10} bearing lifetime theory respectively. From Figure 6.5, it can be seen that the failure rate from the amended theoretical calculation lies between the failure rates from the condition monitoring and the L_{10} theory. In the first 23 months, the failure rate from the L_{10} theory is the highest with a regressively increasing trend. Dur-

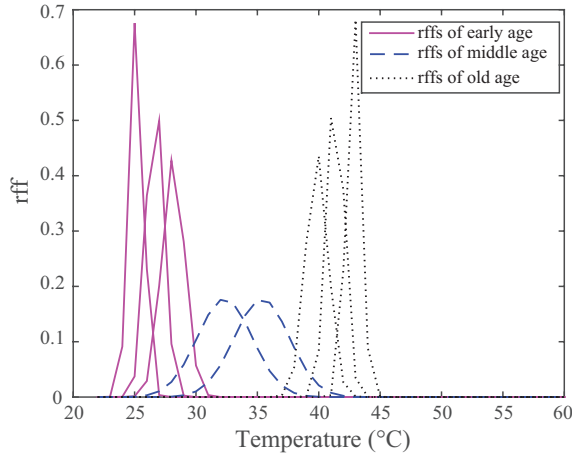


Figure 6.4: Simulation of temperature for a population of bearings at different ages.

ing this period, the rff of the temperature concentrates in the low temperature region (<32 °C in Figure 6.4), which means very few roll bearings’ temperature exceeds the threshold value. Therefore, the failure rate from the condition monitoring is very low. The failure rate from the amended theoretical calculation is roughly the mean of the failure rates from the theoretical calculation and the condition monitoring.

6

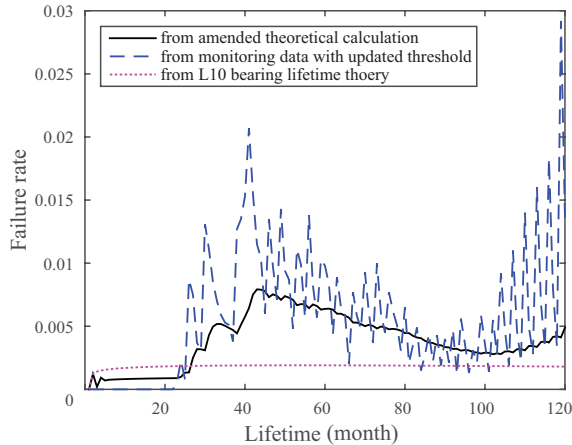


Figure 6.5: Failure rates from the amended theoretical calculation, the condition monitoring with updated threshold and the L_{10} bearing lifetime theory.

After 23 months, the failure rate from the condition monitoring becomes higher than the one from the L_{10} theory. This is because the simulated rff of the temperature shifts to high values which results in more bearings’ temperatures exceeding the threshold. It is also noticed that the failure rate from the condition monitoring may change significantly. This can be attributed to the simultaneous change of both the simulated temperature measurements and the threshold value. The failure rate from the L_{10} theory is almost constant

at 0.2 percent. This is because the inspection interval (600 hours) in the simulation is too small considering the L_{10} rating life (33171 hours) for the results of Eq. (6.5). Meanwhile, the failure rate from the amended theoretical calculation is observed to change more smoothly than the one from the condition monitoring. From Figure 6.5 it can be concluded that the failure rate from the amended theoretical calculation is more accurate than the one from the L_{10} theory because it incorporates the real time condition data.

Figure 6.6 illustrates the updating of the threshold during the simulation. In the first 23 months, the threshold decreases linearly from the initial 40 °C to 31.2 °C. Afterwards, the threshold is observed to increase and ends up at 44.5 °C after 120 months at the end of the simulation. Figure 6.6 shows that it is possible to update the threshold with a given initial value, real time data and the theoretical calculation. Though the variation of the threshold is not big in this case study, considering the large population of the roll bearings, the number of false replacement of idler rolls can still be considerable with a change of the threshold value of just 1 °C.

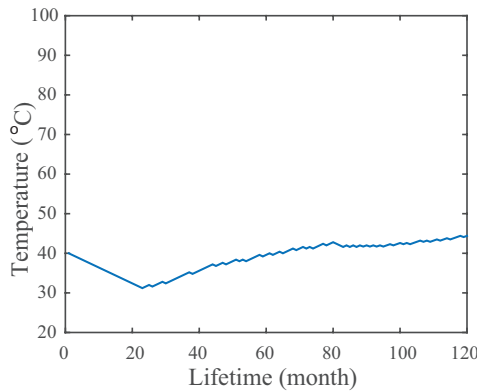


Figure 6.6: Evolution of the threshold during the simulation.

Figure 6.7 presents the cumulative distribution of the roll bearing failures from the framework for the integrated decision making, the conventional approach with a constant threshold (40 °C) and the L_{10} theory respectively. As the failed rolls are assumed to be replaced immediately, the cdfs are equal to the percentage of roll replacement compared to the whole population. In general, the cdf from the L_{10} theory is observed to increase linearly in the 120 months, the one from the framework increases moderately while the one from the conventional approach remains very low during the first 60 months and rises dramatically afterwards before reaching 100 percent of roll replacement. This means that if the threshold value was fixed at 40 °C, all roll bearings should have been replaced before 86 months. On the other hand, the framework suggests the percentage of roll replacement is 45 percent till 86 months. This indicates that the concept of updating the threshold in the framework may save 55 percent of roll bearing replacement compared to the conventional approach.

In Figure 6.7, the cdf from the framework is about 62 percent at 120 months. This means that 62 percent of the roll bearings have been replaced in the ten years. Meanwhile, the L_{10} theory shows that only 22 percent of the roll bearings are replaced till the end of 120 months. Therefore, it is reasonable to claim that for this simulation case study

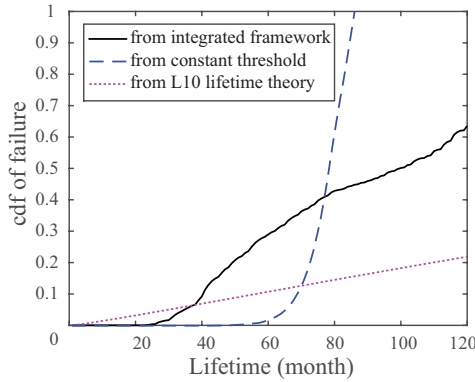


Figure 6.7: Cumulative distribution of roll bearing failures from the integrated maintenance framework, the condition monitoring with a constant threshold value and the L_{10} bearing lifetime theory.

the constant threshold approach overestimates the roll bearing failures while the L_{10} theory underestimates the failures. The framework for the integrated maintenance decision making provides a more accurate estimation of the number of roll bearing failures.

In summary, the simulation case study verifies the effectiveness of the framework for the integrated maintenance decision making. From the simulation, it can be concluded that the amended theoretical calculation of the failure rate is more accurate than the L_{10} theory. In addition, the framework may save a considerable amount of roll replacements compared to the conventional constant threshold approach.

6.4 Conclusions

In this chapter a framework for the integrated decision making of the idler maintenance was developed. The framework incorporates the failure rates from both the theoretical calculation of the reliability and condition monitoring data. In the framework, a conceptual interaction between the two approaches is prompted, which leads to continuous amendment of the theoretical calculation of the failure rate and the update of the threshold value. By implementing the framework, the diagnoses on roll failures and the determination of inspection intervals can be achieved. A simulation case study was also conducted. The case study shows that the framework can improve the predictability of the failure rate of idler roll bearings, and improve the diagnoses on roll failures compared to the conventional constant threshold approach. For further research, it is recommended to investigate how to develop an accurate model for the error term and how to derive appropriate inspection intervals based on the framework.

7

CONCLUSIONS AND RECOMMENDATIONS

This thesis aims to improve the reliability of belt conveyor systems with a focus on idlers. To reflect the research in previous chapters on the goal, this chapter provides conclusions in Section 7.1 corresponding to the research questions in Chapter 1. Recommendations for future research are provided in Section 7.2.

7.1 Conclusions

In this thesis, the following main research question is answered: *How to improve the reliability of belt conveyor systems?* The reliability of a belt conveyor system is the integrated reliability of all components. Considering idler rolls are still a big challenge for the reliable performance of belt conveyors, this thesis investigated how to improve the reliability of idler rolls. The emphasis of this research is on enhancing the predictability of idler roll failures.

In addition, the four sub research questions formulated in Chapter 1 are answered as follows:

- How to predict idler roll failures?

Three approaches are proposed to predict idler roll failures (Chapter 2): theoretical calculation of the reliability of idler rolls, diagnoses on roll failures based on condition monitoring data, and integrated decision making which combines both the theoretical approach and the condition monitoring approach. The three approaches are discussed respectively in different chapters.

- How to calculate the reliability of idler rolls?

From literature it is found that the bearing lifetime theory from Lundberg and Palmgren (1949) is the most widely accepted theoretical approach for the calculation of the

reliability of idler roll bearings (Chapter 2). Considering the determination of the load on roll bearings is very important to apply the bearing lifetime theory, this thesis investigated the determination of the load using both theoretical and experimental approaches.

An analytical approach is developed to determine the load on roll bearings due to the conveyed bulk material, the belt and the roll. For the load from the belt, it is concluded that the effect of belt sagging can be neglected. A new analytical model (the SD model) is developed to provide a lower bound solution for the bulk load. Combining the SD model with an upper bound model (the KH model) from Krause and Hettler (1974), an aggregation model for the bulk load is also developed. Comparisons between the SD model, the KH model and the aggregation model with experimental measurements show that the aggregation model is able to provide more accurate prediction of the bulk load than the SD model or the KH model.

In addition, for the direct measurement of the bulk load, the applicability of a tactile pressure sensor is examined (Chapter 4). The percentage of error for the measurements using the tactile pressure sensor varied from 8.7 percent to 33.7 percent. It is concluded that the tactile pressure sensor is able to provide qualitative insight into the bulk load distribution for scientific purpose. However, the measurements of the tactile pressure sensor provide limited quantitative information on the transverse distribution of the bulk load due to its intrinsic limitations and the belt behavior at idler junctions for the fabric belt used in this study.

- How to detect idler roll failures?

7 From the experimental study it is concluded that idler rolls in the final failure stage can be detected by applying condition monitoring techniques (Chapter 5). Parameters including the temperature, vibration and acoustic emission are applicable for the condition monitoring of idler rolls. Within the three parameters, the measurement of the temperature is suggested to be the most effective inspection solution. Specifically, the measurement of the temperature at shaft ends of idler rolls is a straightforward and effective approach to detect idler roll failures. The RMS level of the horizontal vibration is also an indicator. The acoustic emission of idler rolls in the final failure stage shows some distinct difference from intact rolls between 1.5 kHz and 9 kHz in this study. It is also concluded that positive correlation exists between the measured temperature, acoustic emission and the rotating resistance of idler rolls.

- Is it possible to achieve integrated decision making on idler maintenance?

The decisions regarding the idler maintenance, i.e. the inspection interval and roll replacement scheduling, is important to ensure the reliable performance of idler rolls. The maintenance decision making which is only based on theoretical calculation of the reliability of idler rolls or condition monitoring data is considered to be inadequate. Therefore, A framework for the integrated maintenance decision making is proposed. The proposed framework incorporates the failure rate as the population characteristic from the theoretical calculation of the reliability of roll bearings, and the condition of individual roll from real time data. By implementing the framework, appropriate inspection intervals and roll replacement scheduling can be achieved.

7.2 Recommendations

Recommendations for further investigations in the sub topics are formulated as follows:

- Theoretical determination of the bulk load

It is recommended to further investigate the movement of bulk particles on a belt during conveyance. The understanding of the movement of bulk particles is important to study the interaction between the particles and the belt. During the development of the theoretical model in this research, a new hypothesis of the movement of bulk particles was prompted. However, further investigation is needed to verify the hypothesis.

A second recommendation is to investigate the aggregation factor which controls the level of aggregation between the upper bound model (the KH model) and the lower bound model (the SD model). The aggregation factor is considered to be dependent on the characteristics of bulk materials (i.e. the internal friction and wall friction), the parameters of a belt (i.e. the bending stiffness) and the loading level of a conveyor. Further experimental measurements are needed to achieve the derivation of the aggregation factor.

- Experimental determination of the bulk load

Experimental study on the determination of the bulk load on steel cord conveyor belts by using tactile pressure sensors is recommended. Steel cord conveyor belts have much higher bending stiffness than fabric belts. Therefore, it is expected that the influence of idler junctions will be minimized on the measurement of the bulk load by using tactile pressure sensors. In this way, the assessment of the applicability of tactile pressure sensors can be further improved.

- Experimental condition monitoring of belt conveyor idlers

Two recommendations for further research are formulated. The first recommendation is to investigate the threshold value of a certain measurement parameter (i.e. the temperature) for the interpretation on the condition of idler rolls. The second recommendation is to investigate the deterioration rate of idler rolls at different stages and the achievable operational time between the final and catastrophic failure stages.

- Integrated maintenance decision making framework

This research only proposed a conceptual framework for the integrated maintenance decision making by cooperating the theoretical approach and the condition monitoring approach. Further research is needed to implement the framework for decision making in real applications, including but not limited to an adequate model for the error term in the framework.

BIBLIOGRAPHY

Alles, R. and Wach, T. Method for monitoring a conveyor belt and system therefore, 2000.

Alport, M., Govende, P., Plumb, S., and van der Merwe, L. Identification of conveyor belt splices and damages using Neural Networks. In *Proceedings of the International Materials Handling Conference (Beltcon) 11*, Johannesburg, South Africa, 2001.

Barrios, G.K.P., de Carvalho, R.M., Kwade, A., and Tavares, L.M. Contact parameter estimation for DEM simulation of iron ore pellet handling. *Powder Technology*, 248: 84–93, November 2013. ISSN 00325910. doi: 10.1016/j.powtec.2013.01.063.

Barry, D. A step by step guide to making your materials handling plant ATEX compliant. In *Proceedings of the MHEA 2014 Bulk Conference*, North Lincolnshire, UK, 2014.

Bartelmus, W. Mathematical modelling and computer simulations as an aid to gearbox diagnostics. *Mechanical Systems and Signal Processing*, 15(5):855–871, 2001. doi: 10.1006/mssp.2001.1411.

Bartelmus, W. Diagnostic information on gearbox condition for mechatronic systems. *Transactions of the Institute of Measurement and Control*, 25(5):451–465, 2003. doi: 10.1191/0142331203tm0099oa.

Bartelmus, W. and Sawicki, W. Progress in quality assessment of conveyor idlers. In *Proceedings of the 16th IMEKO World Congress*, Vienna, Austria, 2000.

Bilgili, E., Yepes, J., Stephenson, L., Johanson, K., and Scarlett, B. Stress inhomogeneity in powder specimens tested in the jenike shear cell: myth or fact? *Particle & Particle Systems Characterization*, 21(4):293–302, November 2004. ISSN 09340866. doi: 10.1002/ppsc.200400942.

Brimacombe, J.M., Wilson, D.R., Hodgson, A.J., Ho, K.C.T., and Anglin, C. Effect of calibration method on Tekscan sensor accuracy. *Journal of Biomechanical Engineering*, 131(3):1–4, March 2009. ISSN 0148-0731. doi: 10.1115/1.3005165.

Budhu, M. *Soil mechanics and foundations*. John Wiley and Sons, Inc., Hoboken, 2nd ed. edition, 1999. ISBN 978-0470556849.

- Buis, AWP and Convery, P. Calibration problems encountered while monitoring stump/socket interface pressures with force sensing resistors: techniques adopted to minimise inaccuracies. *Prosthetics and Orthotics International*, 21(3):179–182, 1997. doi: 10.3109/03093649709164552.
- Cazzola, D., Trewartha, G., and Preatoni, E. Time-based calibrations of pressure sensors improve the estimation of force signals containing impulsive events. *Proceedings of the Institution of Mechanical Engineers, Part P: Journal of Sports Engineering and Technology*, 228(2):147–151, September 2013. ISSN 1754-3371. doi: 10.1177/1754337113504397.
- Chaari, F., Bartelmus, W., Zimroz, R., Fakhfakh, T., and Haddar, M. Gearbox vibration signal amplitude and frequency modulation. *Shock and Vibration*, 19(4):635–652, 2012. doi: 10.3233/SAV-2011-0656.
- Chen, J. and Patton, R.J. *Robust model-based fault diagnosis for dynamic systems*. Kluwer Academic, Boston, US, 1999. ISBN 978-1-4615-5149-2.
- CKIT. Mathematical selection criteria with particular reference to the influence of additional loads, 1991. URL http://www.ckit.co.za/secure/conveyor/troughed/idlers/idlers_math_selection_criteria.html.
- CKIT. Troughed belt conveyors, 2012. URL <http://www.ckit.co.za/secure/conveyor/troughed/indextrough.htm>.
- Clayton, C.R.I., Milititsky, J., and Woods, R.I. *Earth pressure and earth-retaining structures*. Thomson Press (India) Limited, New Delhi, 2nd ed. edition, 1993.
- Conveyor Equipment Manufacturers Association. CEMA 502: Bulk material belt conveyor troughing and return idlers - Selection and dimensions, 2004.
- Conveyor Equipment Manufacturers Association. *Belt conveyors for bulk materials*. CEMA, Naples, FL, 7th ed. edition, 2014.
- Cornish, R.J. Pressure on a hopper wall at a stress discontinuity during mass flow. *Powder Technology*, 8(1):1–12, 1973. doi: 10.1016/0032-5910(73)80058-0.
- Douglas Manufacturing Co. Inc. Safety, operation & maintenance manual, 2011. URL http://www.douglasmanufacturing.com/es/somm/SOMM_Idler.pdf.
- Dratt, M., Katterfeld, A., and Wheeler, C.A. Determination of the bulk flexure resistance via coupled FEM-DEM simulation. *Bulk Solids Handling*, 3:50–58, 2015.
- Drewniak, E.I., Crisco, J.J., Spenciner, D.B., and Fleming, B.C. Accuracy of circular contact area measurements with thin-film pressure sensors. *Journal of Biomechanics*, 40(11):2569–2572, 2007. doi: 10.1016/j.jbiomech.2006.12.002.
- Dumbleton, T., Buis, A.W., McFadyen, A., McHugh, B.F., McKay, G., Murray, K.D., and Sexton, S. Dynamic interface pressure distributions of two transtibial prosthetic socket concepts. *Journal of Rehabilitation Research and Development*, 46(3):405–415, 2009. doi: 10.1682/JRRD.2008.01.0015.

- Ebrahimian, B., Noorzad, A., and Alsaleh, M.I. Modeling shear localization along granular soil–structure interfaces using elasto-plastic Cosserat continuum. *International Journal of Solids and Structures*, 49(2):257–278, January 2012. ISSN 00207683. doi: 10.1016/j.ijsolstr.2011.09.005.
- Farmer, D. Understanding conveyor system noise. *The Fortnadvantage*, 1(2), 2000.
- Fauerbach, R. Possible trends in belt conveyor technology. In *Proceedings of the International Materials Handling Conference (Beltcon) 7*, Johannesburg, South Africa, 1993.
- Fernandez, M., Rodriguez, A., Pruchnicka, J., Hoischen, U., Wojtas, P., Gonzalez, J., and Cole, J. Early detection and fighting of fires in belt conveyor. Technical report, European Commission: Luxemburg, 2013.
- Fourie, J.H., Alport, M.J., Basson, J.F., and Padayachee, T. Condition monitoring of fabric reinforced conveyor belting using digital X-RAY imaging. In *Proceedings of the International Materials Handling Conference (Beltcon) 13*, Johannesburg, South Africa, 2005.
- Francart, W.J. Reducing belt entry fires in underground coal mines. In *11th US/North American Mine Ventilation Symposium*, 2006.
- Ganainy, H., Tessari, A., Abdoun, T., and Sasanakul, I. Tactile pressure sensors in centrifuge testing. *Geotechnical Testing Journal*, 37(1):1–13, January 2014. ISSN 01496115. doi: 10.1520/GTJ20120061.
- Gao, Y. and Wang, Y. Calibration of tactile pressure sensors for measuring stress in soils. *Geotechnical Testing Journal*, 36(4):1–7, July 2013. ISSN 01496115. doi: 10.1520/GTJ20120143.
- Gartland, J.J. Conveyor belt with microcoil springwire sensor, 2002.
- Geesmann, F. *Experimentelle und Theoretische Untersuchungen der Bewegungswiderstände von Gurtförderanlagen*. Phd thesis, The University of Hannover, 2001.
- Geesmann, F., Nagy, E., and Bati, J. Design of heavy-duty idlers for the upper run of belt conveyors Part I: Idler requirements. *Aufbereitungs Technik*, 49(11-12):30–45, 2008.
- Geesmann, F., Nagy, E., and Bati, J. Design of heavy-duty idlers for the upper run of belt conveyors Part II: Engineering design of idlers. *Aufbereitungs Technik*, 50(3):4–24, 2009a.
- Geesmann, F., Nagy, E., and Bati, J. Design of heavy-duty idlers for the upper run of belt conveyors Part III: Operational design of an idler. *Aufbereitungs Technik*, 50(4):35–45, 2009b.
- German Institute for Standardization. DIN 22101: Continuous conveyors - Belt conveyors for loose bulk materials - Basis for calculation and dimensioning, 2002.
- Gładysiewicz, L. and Kawalec, W. Carrying idler spacing with regard to distribution of the conveyed bulk material stream. In *Bulk Solids EUROpe 2010*, 2010.

- Gladysiewicz, L., Hardygora, M., and Kawalec, W. Belt conveying in the polish mining industry - Selected topics. *Bulk Solids Handling*, 24(4):236–242, 2004.
- Goode, K.B., Moore, J., and Roylance, B.J. Plant machinery working life prediction method utilizing reliability and condition-monitoring data. *Proceedings of the Institution of Mechanical Engineers, Part E: Journal of Process Mechanical Engineering*, 214:109–122, 2000. doi: 10.1243/0954408001530146.
- Grabner, K., Grimmer, K.J., and Kessler, F. Research into normal forces between belt and idlers at critical locations on the belt conveyor track. *Bulk Solids Handling*, 13(4): 727–734, 1993.
- Granig, R. High quality idlers at the Henderson mine. *Bulk Solids Handling*, 20(3): 325–328, 2000.
- Grzybek, H. Früherkennung von bränden und rollenheißläufern an gurtförderanlagen. In *Fachtagung Schüttgutförderertechnik 2011 "Anlagen - Bauteile - Computersimulationen"*, 2011.
- Gurjar, R.S. Failure analysis of belt conveyor system by Pareto Chart. *International Journal of Engineering and Social Science*, 2(10):60–71, 2012. ISSN 2249- 9482.
- Haines, M. *Development of a conveyor belt idler roller for light weight and low noise*. Master thesis, The University of New South Wales, 2007.
- Harris, T.A. *Rolling bearing analysis*. John Wiley & Sons, INC., New York, US, 4th ed. edition, 2001.
- Harrison, A. *Dynamic measurement and analysis of steel cord conveyor belts*. Phd thesis, The University of Newcastle, 1984.
- Harrison, A. Belt vibration and its influence on conveyor reliability. *Bulk Solids Handling*, 14(4):723–727, 1994.
- Harrison, A. and Brown, B.C. Monitoring system for steel-reinforced conveyor belts. *Journal of Engineering for Industry*, 108(2):148–153, 1986. doi: DOI:10.1115/1.3187050.
- Harrison, A. and Roberts, A.W. Trends in the application of troughed conveyor belts. In *Proceedings of the International Materials Handling Conference (Beltcon) 2*, Johannesburg, South Africa, 1983.
- Hawksworth, S.J., Gummer, J., Davidson, J., and Williams, M. Ignition from conveyor idler rollers. In *Proceedings of the 30th International Conference of Safety in Mines Research Institutes*, Johannesburg, South Africa, 2003.
- He, Y., Roberts, A.W., Prigge, J.-D., and Jones, M.G. Pressures on the support columns buried in iron ore stockpiles. *Powder Technology*, 258:358–369, May 2014. ISSN 00325910. doi: 10.1016/j.powtec.2014.03.044.
- Health and Safety Executive. Safety and health in mines research advisory board - Annual review 2004, 2004. URL <http://www.hse.gov.uk/aboutus/meetings/committees/shmrab/shmrab04b.htm>.

- Heemskerk, R.S. Rolling bearings in bulk conveyors. In *Proceedings of the International Materials Handling Conference (Beltcon) 4*, Johannesburg, South Africa, 1987.
- Heng, A., Zhang, S., Tan, A.C.C., and Mathew, J. Rotating machinery prognostics: State of the art, challenges and opportunities. *Mechanical Systems and Signal Processing*, 23 (3):724–739, 2009. doi: 10.1016/j.ymssp.2008.06.009.
- Hills, P.W. Condition monitoring keeps conveyors conveying. In *Proceedings of the International Materials Handling Conference (Beltcon) 15*, Johannesburg, South Africa, 2009.
- Ilic, D. *Bulk solid interactions in belt conveying systems*. Phd thesis, The University of Newcastle, 2013.
- International Organization for Standardization. ISO 15236-1: Steel cord conveyor belts Part 1: Design, dimensions and mechanical requirements for conveyor belts for general use, 2005.
- International Organization for Standardization. ISO 703: Conveyor belts - Transverse flexibility (troughability) - Test method, 2007.
- Intium Solutions. Roller condition monitoring system, 2014. URL <http://intiumsolutions.com>.
- Jayaswal, P., Verma, S.N., and Wadhvani, A.K. Development of EBP-artificial neural network expert system for rolling element bearing fault diagnosis. *Journal of Vibration and Control*, 17(8):1131–1148, 2011. doi: 10.1177/1077546310361858.
- Jeansch, T., Sader, M., Noack, R., Barber, K., Ding, S., Zang, P., and Zhong, M. A robust model-based information system for monitoring and fault detection of large scale belt conveyor systems. In *Proceedings of the 4th World Congress on Intelligent Control and Automation*, pages 3283–3287, 2002. ISBN 0780372689.
- Johanson, K. and Bucklin, R. Measurement of K-values in diamondback hoppers using pressure sensitive pads. *Powder Technology*, 140(1-2):122–130, February 2004. ISSN 00325910. doi: 10.1016/j.powtec.2004.01.002. URL <http://linkinghub.elsevier.com/retrieve/pii/S0032591004000191>.
- Katterfeld, A., Dratt, M., and Wheeler, C.A. Prediction of conveyor belt deflection by coupling of FEM and DEM simulations. *Bulk Solids Handling*, 30(7):380–384, 2010.
- King, T.J. Belt conveyor pulley design - Why the failures. In *Proceedings of the International Materials Handling Conference (Beltcon) 2*, Johannesburg, South Africa, 1983.
- König, J. and Burkhard, O. Girlandenprüfstand zur Zustandsdiagnose gebrauchter Tragrollen. In *Proceedings of the Fachtagung Schüttgutförderertechnik "Treffpunkt für Forschung & Praxis"*, Magdeburg, Germany, 2013.
- Krause, F. and Hettler, W. Die Belastung der Tragrollen von Gurtbandförderern mit dreiteiligen Tragrollenstationen infolge Fördergut unter Beachtung des Fördervorganges und der Schüttguteigenschaften. *Wissenschaftliche Zeitschrift der Technischen Hochschule Otto von Guericke*, 18(6/7):667–674, 1974.

- Król, R. and Kisielewski, W. Research of loading carrying idlers used in belt conveyor - Practical applications. *Diagnostyka*, 15(1):67–73, 2014.
- Kruse, D. Data acquisition techniques and measurement equipment for belt conveyors. *Bulk Solids Handling*, 26(2):116–122, 2006.
- Leonida, C. Conveyor: The future of material handling? *Mining Magazine*, pages 62–75, 2013.
- Li, Y., Billington, S., Zhang, C., Kurfess, T., Danyluk, S., and Liang, S. Dynamic prognostic prediction of defect propagation on rolling element bearings. *Tribology Transactions*, 42(2):385–392, January 1999. ISSN 1040-2004. doi: 10.1080/10402009908982232. URL <http://www.tandfonline.com/doi/abs/10.1080/10402009908982232>.
- Liu, X., Lodewijks, G., and Pang, Y. Intelligent maintenance of large-scale belt conveyor idler rolls: State-of-the-art and opportunities. In *Proceedings of the 1st Symposium on Automated Systems and Technologies*, pages 95–103, Hannover, Germany, 2014a.
- Liu, X., Pang, Y., and Lodewijks, G. A new analytical model of load calculation for trough idler rolls stress discontinuity model for conveyor idler roll load calculation. In *Proceedings of the MHEA 2014 Bulk Conference*, North Lincolnshire, UK, 2014b.
- Liu, X., Pang, Y., and Lodewijks, G. A stress discontinuity approach to model the stress profile on a loaded conveyor belt. *Powder Technology*, 273:102–110, 2015a. doi: 10.1016/j.powtec.2014.12.040.
- Liu, X., Pang, Y., Lodewijks, G., Wheeler, C.A., and Beh, B. Quantification of the pressure distribution on a loaded conveyor belt using a tactile pressure sensor. In *Proceedings of the XXI International Conference on Material Handling, Constructions and Logistics (MHCL)*, Vienna, Austria, 2015b.
- Liu, X., Pang, Y., Lodewijks, G., Wheeler, C.A., and Beh, B. Assessment of the dynamic pressure measurement on a loaded conveyor belt using a tactile pressure sensor. In *Proceedings of the XXI International Conference on Material Handling, Constructions and Logistics (MHCL)*, Vienna, Austria, 2015c.
- Liu, X., Pang, Y., and Lodewijks, G. Theoretical and experimental determination of the pressure distribution on a loaded conveyor belt. *Measurement*, 77:307–316, 2016. doi: 10.1016/j.measurement.2015.08.041.
- Lodewijks, G. The rolling resistance of conveyor belts. *Bulk Solids Handling*, 15(1): 15–22, 1995.
- Lodewijks, G. *Dynamics of belt systems*. Phd thesis, Delft University of Technology, 1996.
- Lodewijks, G. Strategies for automated maintenance of belt conveyor systems. In *Proceedings of the International Materials Handling Conference (Beltcon) 12*, Johannesburg, South Africa, 2003.

- Lodewijks, G. Two decades dynamics of belt conveyor systems. In *Proceedings of the International Materials Handling Conference (Beltcon) 11*, Johannesburg, South Africa, 2011.
- Lodewijks, G. Personal interview, 2015.
- Lodewijks, G. and Ottjes, J.A. Intelligent belt conveyor monitoring and control: Theory and applications. In *Proceedings of the International Materials Handling Conference (Beltcon) 13*, Johannesburg, South Africa, 2005a.
- Lodewijks, G. and Ottjes, J.A. Application of Fuzzy Logic in belt conveyor monitoring and control. In *Proceedings of the International Materials Handling Conference (Beltcon) 13*, Johannesburg, South Africa, 2005b.
- Lodewijks, G., Duinkerken, M.B., Cruz, A. M. L., and Veeke, H.P.M. The application of RFID technology in belt conveyor systems. In *Proceedings of the International Materials Handling Conference (Beltcon) 14*, Johannesburg, South Africa, 2007.
- Lommen, S., Schott, D., and Lodewijks, G. DEM speedup: Stiffness effects on behavior of bulk material. *Particuology*, 12:107–112, February 2014. ISSN 16742001. doi: 10.1016/j.partic.2013.03.006.
- Lundberg, G. and Palmgren, A. Dynamic capacity of rolling bearings. *Journal of Applied Mechanics*, 16(2):165–172, 1949.
- Madden, W.F. An investigation into idler seals and the effect on rim drag. In *Proceedings of the International Materials Handling Conference (Beltcon) 9*, Johannesburg, South Africa, 1997.
- Martin Engineering. Martin plus walk the belt program, 2014. URL <https://www.martin-eng.com/press-release/martinplus-walk-belt-program>.
- Mitteldeutsche Braunkohlengesellschaft mbH. Mobile thermographic monitoring of belt conveyors helps avoid fires, 2015. URL http://www.flirimedia.com/MMC/THG/Brochures/AUT_033/AUT_033_EN.pdf.
- Nicholas, J.W., Corvese, R.J., Woolley, C., and Armstrong, T.J. Quantification of hand grasp force using a pressure mapping system. *Work*, 41:605–12, 2012. doi: 10.3233/WOR-2012-0217-605.
- Niebel, B.W. *Engineering maintenance management*. Marcel Dekker, Inc., New York, US, 2nd ed. edition, 1994.
- Nordell, L.K. Overland conveyors designed for efficient cost and performance. In *Proceedings of the International Materials Handling Conference (Beltcon) 12*, Johannesburg, South Africa, 2003. ISBN 3606712200.
- O'Connor, P.D.T. *Practical reliability engineering*. John Wiley & Sons Ltd., Chichester, 3rd ed. edition, 1991. ISBN 0471926965.
- Owen, P. Condition monitoring for conveyors. In *Proceedings of the International Materials Handling Conference (Beltcon) 9*, Johannesburg, South Africa, 1997.

- Paikowsky, S.G. and Hajduk, E.L. Calibration and use of grid-based tactile pressure sensors in granular material. *geotechnical testing journal*, 20(2):218–241, 1997. doi: 10.1520/GTJ10741J.
- Palmer, M.C., O'Rourke, T.D., Olson, N.A., Abdoun, T., Ha, D., and O'Rourke, M.J. Tactile pressure sensors for soil-structure interaction assessment. *Journal of Geotechnical & Geoenvironmental Engineering*, 135(11):1638–1645, 2009. doi: 10.1061/ASCEGT.1943-5606.0000143.
- Pang, Y. *Intelligent belt conveyor monitoring and control*. Phd thesis, Delft University of Technology, 2010.
- Pang, Y. and Lodewijks, G. The application of RFID technology in large-scale dry bulk material transport system monitoring. In *Proceedings of the IEEE Workshop on Environmental Energy and Structural Monitoring Systems*, pages 5–9, Milan, 2011.
- Pang, Y. and Lodewijks, G. Agent-based intelligent monitoring in large-scale continuous material transport. In *Proceedings of the 9th IEEE International Conference on Networking, Sensing and Control*, pages 79–84, Beijing, China, 2012. Ieee. ISBN 978-1-4673-0390-3. doi: 10.1109/ICNSC.2012.6204895.
- Pang, Y. and Lodewijks, G. A remote intelligent belt conveyor inspection tool. In *Proceedings of the 11th International Congress on Bulk Materials Storage, Handling and Transportation*, Newcastle, UK, 2013.
- Paton, C.G., Bland, S.B., and Melley, R.E. Lubricants in conveyor applications. *Lubrication Engineering*, 51(1):6–15, 1995.
- Paul, J. and Shortt, G. Investigation of maximum belt speed of idlers. In *Proceedings of the International Materials Handling Conference (Beltcon) 14*, Johannesburg, South Africa, 2007.
- Powrie, William. *Soil mechanics: Concepts and applications*. Taylor & Francis, New York, US, 2nd ed. edition, 2004.
- Pytlik, Andrzej. Durability testing of idlers for belt conveyors. *Journal of Sustainable Mining*, 12(3):1–7, 2013. doi: 10.7424/jsm130301.
- Qiu, H., Lee, J., Lin, J., and Yu, G. Robust performance degradation assessment methods for enhanced rolling element bearing prognostics. *Advanced Engineering Informatics*, 17(3–4):127–140, 2003. doi: 10.1016/j.aei.2004.08.001.
- Raytek Corporation. Emissivity of most common materials, 1999. URL <http://www.raytek.com/Raytek/en-r0/IREducation/Emissivity.htm>.
- Relicks, A.V. Belt conveyor idler roll behaviors. In Alsbaugh, M.A., editor, *Bulk Material Handling By Conveyor Belt 7*, pages 35–40. Society for Mining, Metallurgy, and Exploration, Littleton, Colo., 2008. ISBN 0873352602.
- Riley, J.R. Infra-red condition monitoring applications. In *Proceedings of the '94 International Conference on Condition Monitoring*, pages 635–643, Swansea, UK, 1994.

- Roberts, A.W. Economic analysis in the optimization of belt conveyor systems. In *Proceedings of the International Materials Handling Conference (Beltcon) 1*, Johannesburg, South Africa, 1981.
- Roberts, A.W. Bulk solid and conveyor belt interactions for efficient transportation without spillage. *Bulk Solids Handling*, 18(1):49–57, 1998.
- Roberts, A.W. and Harrison, A. Recent research developments in belt conveyor technology. In *Proceedings of the International Materials Handling Conference (Beltcon) 4*, Johannesburg, South Africa, 1987.
- Roscoe, KH. The influence of strains in soil mechanics. *Geotechnique*, (2):129–170, 1970.
- Rose, J.G. and Stith, J.C. Pressure measurements in railroad trackbeds at the rail/tie interface using Tekscan sensors. In *Proceedings of the American Railway Engineering and Maintenance of Way Assoc. 2004 Annual Conference*, Nashville, US, 2004.
- Rozentals, J. J. and Msaima, B. E. The design of troughing idlers. In *Proceedings of the International Materials Handling Conference (Beltcon) 1*, Johannesburg, South Africa, 1981.
- Rulmeca Holding S.p.A. Rollers and components for bulk handling, 2003. URL http://www.rulmeca.com/en/products_bulk/catalogue/1/trasporto_a_nastro/1/rollers.
- Sawicki, Mateusz, Zimroz, Radoslaw, Wyłomańsk, Agnieszka, Obuchowski, Jakub, Stefaniak, Pawel, and Żak, Grzegorz. An automatic procedure for multidimensional temperature signal analysis of a SCADA system with application to belt conveyor components. *Procedia Earth and Planetary Science*, 15:781–790, 2015. ISSN 18785220. doi: 10.1016/j.proeps.2015.08.126. URL <http://linkinghub.elsevier.com/retrieve/pii/S1878522015003896>.
- Scheaffer, R.L. and McClave, J.T. *Probability and statistics for engineers*. PWS-KENT Publishing Company, Boston, US, 3rd ed. edition, 1990.
- Schofield, Andrew and Wroth, Peter. *Critical state soil mechanics*. London: McGraw Hill, 1968.
- Scott Automation & Robotics. Robotic Idler Prediction System, 2014. URL <http://www.machineryautomation.com.au/>.
- Sharpe, V. and Leaney, D. Condition monitoring techniques for optimisation of wind farm performance. *International Journal of Condition Monitoring and Diagnostic Engineering Management*, 2:5–13, 1999.
- Sikkes, V. Laboratory experimental research on multi-sensor monitoring of belt conveyor idlers-Phase Two. Technical report, Delft University of Technology, 2016.
- SKF. Selecting conveyor idler roller bearings. *The South African Mechanical Engineer*, 36:251–255, 1986.

- SKF. SKF idler sound monitor kit, 2012. URL <http://www.skf.com/caribbean/industry-solutions/metals/Processes/upstream-steel-making/conveyors/SKF-idler-sound-monitor-kit.html>.
- Smith, W.A.C. and Spriggs, G.H. Long overland conveyors. In *Proceedings of the International Materials Handling Conference (Beltcon) 1*, Johannesburg, South Africa, 1981.
- Sokolovski, V V. *Statics of granular media*. Pergamon Press, Moscow, Russia, 1st ed. edition, 1965. ISBN 9780080136240.
- Spaans, C. The calculation of the main resistance of belt conveyors. *Bulk Solids Handling*, 11(4):809–826, 1991.
- Steinberg, P.W. Overview and current state of the art in belt conveying in South Africa, 1983.
- Stewart-Lord, M. Rolling bearing characteristics for maximising the life of conveyor idler rolls. In *Proceedings of the International Materials Handling Conference (Beltcon) 6*, Johannesburg, South Africa, 1991.
- Surtees, A.J. Conveyor system commissioning, maintenance and failure analysis using black box techniques. In *International Materials Handling Conference (Beltcon) 8*, Johannesburg, South Africa, 1995.
- Tekscan Inc. Tekscan sensor model 5315, 2014. URL <http://www.tekscan.com/5315-pressure-sensor>.
- Terzaghi, K. *Theoretical soil mechanics*. John Wiley and Sons, Inc., New York, US, 1943.
- Terzaghi, K. and Peck, R. *Soil mechanics in engineering practice*. McGraw-Hill, New York, US, 2nd ed. edition, 1967.
- Thieme, K.R. Economic justification of automated idler roll maintenance applications in large-scale belt conveyor systems. Technical report, Delft University of Technology, 2014.
- Tomsky, Eilis H. How to evaluate belt conveyor idlers. *Coal Mining*, 22(11):43–46, 1985.
- Tooker, G. E. The economics of idler load rating and spacing. *Bulk Solids Handling*, 8(6):89–96, 1988.
- Tuckey, K., Womach, R., and Stolz, H. Maintenance on belt conveyors - A practical approach to this vital link in continuous production. In *Proceedings of the International Materials Handling Conference (Beltcon) 3*, Johannesburg, South Africa, 1985.
- Vayeron Pty Ltd. Smart-Idler, 2013. URL <http://www.vayeron.com.au/>.
- Vogel, B. Tragrollenheiläufer – möglichen der faseroptischen temperaturmessung. In *Fachtagung Schüttgutfördertechnik 2011 "Anlagen - Bauteile - Computersimulationen"*, 2011.

- von Bodegom, E.W.L.A. Laboratory experimental research on multi-sensor monitoring of belt conveyor idlers. Technical report, Delft University of Technology, 2015.
- Watson, D.R. and Niekerk, J.V. High speed conveyor idlers. In *Proceedings of the International Materials Handling Conference (Beltcon) 4*, Johannesburg, South Africa, 1989.
- Wheeler, C.A. Predicting the main resistance of belt conveyors. In *International Materials Handling Conference (Beltcon) 12*, Johannesburg, South Africa, 2003a.
- Wheeler, C.A. *Analysis of the main resistances of belt conveyors*. Phd thesis, The University of Newcastle, 2003b.
- Wheeler, C.A. and Ausling, D. Evolutionary belt conveyor design. In *Proceedings of the International Materials Handling Conference (Beltcon) 14*, Johannesburg, South Africa, 2007.
- Yang, B. *Fibre optic conveyor monitoring system*. Msc. thesis, The University of Queensland, 2014.
- Zhang, Y. Conveyor belt bottom cover failure from idlers and pulleys. In *Proceedings of the International Materials Handling Conference (Beltcon) 18*, Johannesburg, South Africa, 2015.
- Zimroz, R. and Bartelmus, W. Application of adaptive filtering for weak impulsive signal recovery for bearings local damage detection in complex mining mechanical systems working under condition of varying load. *Solid State Phenomena*, 180:250–257, 2012. ISSN 1662-9779. doi: 10.4028/www.scientific.net/SSP.180.250.
- Zimroz, R. and Krol, R. Failure analysis of belt conveyor systems for condition monitoring purposes. *Prace Naukowe Instytutu Górnictwa Politechniki Wrocławskiej*, 128(36): 255–270, 2009.
- Zimroz, R., Król, R., and Jurdziak, L. The application of GISs to support belt conveyor maintenance management. *Prace Naukowe Instytutu Górnictwa Politechniki Wrocławskiej*, 128(36):271–284, 2009.

APPENDIX

Appendix A: Idler roll load sharing optimization program

The SD model can be applied to enable a balanced load sharing between the center roll and the wing rolls by searching for an optimal combination of a trough angle and a ratio between the length of the center roll and the wing roll. For this purpose, a program is developed in Matlab (version 2011b, The Mathworks Inc.), which can be seen in Figure A.1. The program is object oriented and has a user friendly interface, it can be easily applied in the design phase of belt conveyor idlers.

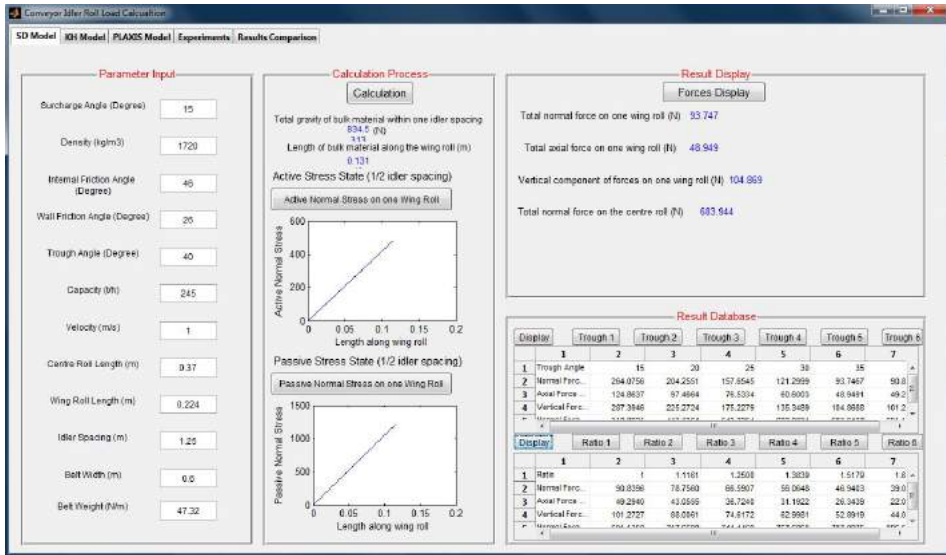


Figure A.1: Idler roll load sharing optimization program.

In order to use the program, the parameters of the conveyed bulk material (including the surcharge angle, density, internal friction angle and wall friction angle), and the parameters of the belt conveyor (including the trough angle, wing roll length, center roll length, capacity, belt velocity, idler spacing, belt width, and belt weight) are required. With these inputs, the tool can produce intermedia results such as the weight of the bulk

material within one idler spacing, and the useful length of loaded wing belt. In addition, two plots will be produced to present the pressure distribution in cases of active and passive stress states. For the final result of single calculation, the total normal and axial forces on each wing roll, as well as the total normal force on the center roll can be calculated and printed on the screen. It has to be mentioned that for the belt load only the weight of the conveyor belt is considered.

In addition, the program can accept multi inputs of trough angles and ratios between the length of the center roll and the wing roll. With the multi inputs of these two variables, a database of the normal and axial forces on the wing rolls, as well as the normal force on the center roll can be produced. The user can find an optimum solution with respect to a balanced load sharing between the wing rolls and the center roll.

In order to explain how the program works, a case study is presented. The inputs for the program are summarized in Table A.1. A belt conveyor with a design capacity of 6000 t/h which will be used for transport of coal is chosen. The parameters regarding the belt conveyor are determined based on industrial experience. The parameters of coal are decided with consultation of the values that Ilic derived from experimental tests [Table 4-2 in (Ilic, 2013)].

Table A.1: Summary of input parameters.

Material parameters	value	Conveyor parameters	value
material	coal	belt speed (v)	5
capacity (t/h)	6000	idler spacing (m)	3
density (ρ)	850	belt width (m)	2
surcharge angle ($^\circ$)	36	belt line load (N/m)	530
wall friction angle ($^\circ$)	33	gravity acceleration (m/s^2)	9.81
internal friction angle ($^\circ$)	55		

Figure A.2 shows the evolution of the percentage of the load on each wing roll and the center roll due to the bulk material and the belt with varying trough angle. The results are achieved with a roll length of 0.75 m for both the center and wing rolls. It can be seen that with growing trough angle, higher percentage of the load is exerted on the center roll and the opposite trend is observed regarding the wing rolls. With a trough angle of 20° , 46.8 percent of the load from the bulk material and the belt is loaded on the center roll, and 26.6 percent of the load is on each wing roll. In comparison, if the trough angle is 45° , 77 percent of the load from the bulk material and the belt is loaded on the center roll, while 11.5 percent of the load is on each wing roll. With increasing trough angle, the depth of the bulk material on the CBS is larger. As a result, more bulk material is loaded on the CBS.

Figure A.3 shows the percentage of the load on the center roll and each wing roll with varying ratio of the roll length. The ratio is calculated as the length of the center roll divided by that of the wing roll. The results in Figure A.3 are achieved with a trough angle of 35° . Higher percentage of the load is on the center roll with larger ratio of the roll length while the opposite trend can be observed for the wing roll. For example, 24.4 percent of the load due to the bulk material and the belt is considered to be exerted on the center roll and 37.8 percent of the load on each wing roll for a ratio of 0.3. If the ratio

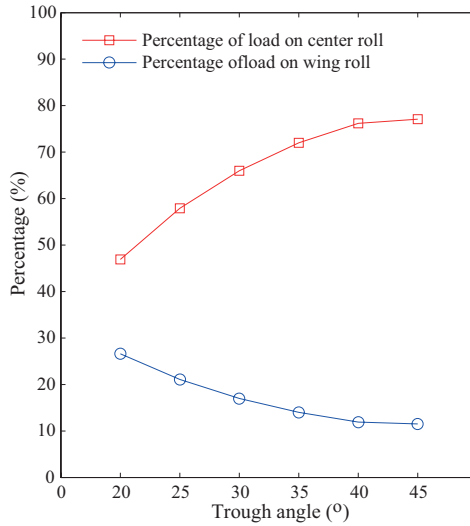


Figure A.2: Percentage of the load on each wing roll and the center roll with varying trough angle.

goes up to 1.0, which means an equal length of the wing roll and the center roll, it can be seen that 72 percent of the load is on the center roll while only 14 percent of the load on one wing roll. The load sharing can be balanced at a ratio around 0.4, for which the length of the wing roll is 0.9 m and the length of the center roll is 0.4 m. The difference between the wing roll length and the center roll length is a bit big. However, by setting a smaller trough angle, the difference in the roll length is expected to be smaller to achieve a balanced load sharing between the wing rolls and the center roll.

From the case study, it can be seen that the program enables an analysis of the resultant idler roll load with many design parameters of the belt conveyor given the characteristics of the bulk material to be transported. The program can also improve the design of belt conveyor idlers with an aim to achieve balanced load sharing and therefore close to equal lifetime of the center and wing rolls.

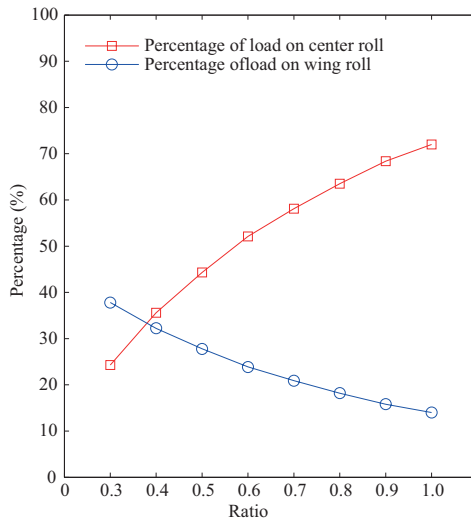


Figure A.3: Percentage of the load on each wing roll and the center roll with varying ratio of roll length. The ratio is calculated as the length of the center roll divided by the length of the wing roll while maintaining the total length of three rolls as 2.25 m.

Appendix B: Datasheets of the sensors

B.1. Datasheet of the thermocouple



RS Stock No. 236-4255

Data sheet

Button Magnet Thermocouple, Type K

1 metre Teflon® insulated cable with type K miniature plug



- Button magnet thermocouple
- Ideal for ferrous metal surface measurement
- Spring loaded junction to ensure good contact
- 1 metre long Teflon® insulated twin-twisted wires
- Fitted miniature plug (200°C)
- Sensor range to 250°C

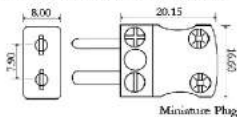
Specifications

Sensor type:	Type K thermocouple to IEC 584
Construction:	Thermo-element located in 1/2" diameter magnet
Cable/Termination:	1 metre PFA Teflon® insulated with miniature plug termination
Thermocouple junction:	Grounded at tip
Magnet:	1/2" diameter button type
Temperature range:	-50°C to +250°C

Product code
BMS-K-1-C70-MP

RS order code
236-4255

Fitted miniature plug dimensions

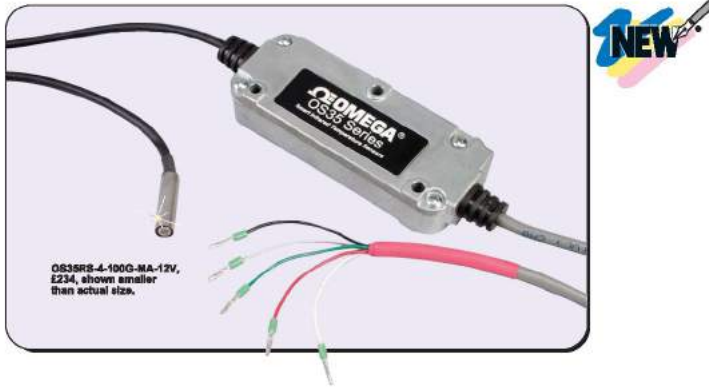


RS018/0912LAB



Note: This datasheet is derived from nl.rs-online.com.

B.2. Datasheet of the infrared sensor



Temperature Range Table (Table 1)

Temperature Code	Temperature Range
100°C	0 to 100°C
250°C	0 to 250°C
70°C	-30 to 70°C
500°C (*)	0 to 500°C

(*) This temperature range is only available with models of 4:1 FOV.

Output Options Table (Table 2)

Output Suffix	Output Type
MA	4 to 20 mA
V10	0 to 10 Volt
V5	0 to 5 Volt
RS2	RS232 communications port

Power Supply Table (Table 3)

Power Supply Suffix	Power
12V	12 Vdc power supply
24V	24 Vdc power supply

MOST POPULAR MODEL HIGHLIGHTED!

To Order (Specify Model Number)		
Model No.	Price	Description
OS35RS-(1)-(2)-(3)	£167	Smart-microIR/c, 1:2 FOV
OS35RS-4-(1)-(2)-(3)	234	Smart-microIR/c.4, 4:1 FOV
OS35RS-SV-(1)-(2)-(3)	218	Smart-microIR/c.SV 1:2, side view
OS35RS-4SV-(1)-(2)-(3)	291	Smart-microIR/c.4SV 4:1, side view

Comes with complete operator's manual

Specify temperature code from Temperature Range Table 1.

Specify output suffix from Output Options Table 2.

Specify power supply suffix from Power Supply Table 3.

Ordering Example: OS35RS-100C-MA-12V, OS35-R3 with a FOV 1:2, temperature range of 0 to 100°C, 4 to 20 mA output and 12 Vdc power supply, £167. OGW-3, OMEGACARE™ extends standard 1-year warranty to a total of 4 years (£42), £167 + 42 = £209.

Note: This datasheet is derived from omega.nl.

B.3. Datasheet of the infrared camera

Imaging Specifications

Imaging & Optical Data	AX8
IR resolution	80 x 60 pixels
Thermal sensitivity (NETD)	< 0.10°C @ +30°C (1.80°F)/100 mK
Field of view (FOV)	48° x 37°
Focus	Fixed
Detector data	
Detector type	Focal Plane Array (FPA), uncooled microbolometer
Spectral range	7.5-12 µm
Visual camera	
Built-in digital camera	640 x 480
Digital camera FOV	Max 66° Adapts to the IR lens
Sensibler	Minimum 10 Lux without illuminator
Measurement	
Object temperature range	-10°C to +150°C (14°F to 302°F)
Accuracy	±2°C (±3.5°F) or ±2% of reading (±10 to +1000 @ ±10 to +35 amb)
Measurement analysis	
Spotmeter	6
Area	6 boxes with max 1/min. Average position
Automatic hot/cold detection	Max/Min temp. value and position shown within box
Isoterm	1 with above/below internal
Measurement presets	Yes
Measurement option	Schedule response, File sending (Tftp, email (SMTP))
Diffusion temperature	Delta temp. use between measurement functions or reference temperature
Reference temperature	Manually set or captured from any measurement function
Atmospheric transmission correction	Automatic, based on inputs for distance, atmospheric temperature and relative humidity
Optics transmission correction	Automatic, based on signals from internal sensors
Emissivity correction	Variable from 0.01 to 1.0
Reflected apparent temperature correction	Automatic, based on input of reflected temperature
External optics/window correction	Automatic, based on input of optics/window transmission and temperature
Measurement corrections	Global and individual object parameters
Alarm	
Alarm functions	6 automatic alarms on any selected measurement function, Digital In, Camera temperature, timer
Alarm output	Digital Out, log, store image, file sending (Tftp, email (SMTP), notification
Set-up	
Color palettes	Color palettes (BW, BW inv, Iron, Rain)
Set-up commands	Data/Time, Temperature °C/°F
Web interface	Yes
Storage of images	
Storage media	Built-in memory for image storage
Image storage mode	IR-visual images, simultaneous storage of IR and visual images, Visual and IR image automatically grouped together
Periodic image storage	Yes
File formats	(JPEG, JPEG+FFF, PNG+JPEG, FFF, FFF+PNG)

Image streaming	AX8
Image streaming formats	Motion JPEG, MPEG stream, H.264 Stream format, MPEG-4 (ISO/IEC 14496-2)
Image streaming resolution	640 x 480
Image modes	Thermal, Visual, MSX (IR image with enhanced detail presentation)
Automatic image adjustment	Contrast/Manual, Linear or histogram based, possible to lock max. min. exposure temperature
Manual image adjustment	Levels/Contrast/Min
Power system	
External power operation	12/24VDC, 2 W continuously/3.1 W absolute max
External power connector	M12 B-pin A-coded (Shared with digital I/O)
Voltage Allowed range	10-30VDC
Environmental data	
Operating temp. range	-30°C to +50°C (32°F to +122°F)
Storage temp. range	-40°C to +70°C (-40°F to +158°F) IAW IEC 68-2-1 and IEC 68-2-2
Humidity (operating and storage)	IEC 60068-2-30/34 95% relative humidity ±25°C to ±40°C (±77°F to ±104°F) 2 cycles
EMC	EN 61000-6-2 2000 (Immunity) EN 61000-6-3 2001 (Emission) FCC 47 CFR Part 15 Class B (Emission)
Encapsulation	IP67 IEC 60529
Bump	25 g IEC 60068-2-201
Vibration	2 g IEC 60068-2-61
Physical data	
Camera size (L x W x H)	54 x 25 x 78 mm with connectors 54 x 25 x 85 mm w/o connectors
Shipping information	
Packaging	Infrared camera with lens, Cardboard box, Ethernet cable, FLIR Tools download card, Mains cable, Power cable, pig-tailed, Power supply, Printed documentation, User documentation

<p>PORTLAND Corporate Headquarters FLIR Systems, Inc. 27700 SW Parkway Ave. Wilsonville, OR 97070 USA PH: +1 866 477 3687</p>	<p>NASHUA FLIR Systems, Inc. 8 Townsend West Nashua, NH 08803 USA PH: +1 803 324 7811</p>
<p>BELGIUM FLIR Systems, Ltd. Luxemburgstraat 2 B-2521 Neer Belgium PH: +32 (0) 3 865 51 00</p>	<p>SANTA BARBARA FLIR Systems, Inc. 70 Castellon Drive Goleta, CA 93117 USA PH: +1 805.680.5097</p>

www.flir.com
NASDAQ: FLIR

Copyright © 2014 FLIR Systems, Inc. All rights reserved. (Dated 03/14)



Note: This datasheet is derived from flir.com.

B.4. Datasheet of the omni-directional microphone

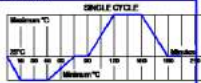
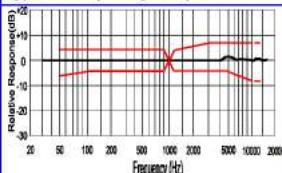
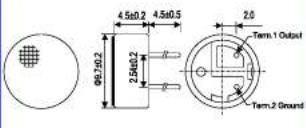


Challenge Electronics
95 East Jeffryn Boulevard
Deer Park, NY 11729
EMAIL: SALES@CHALLELEC.COM

Tel: 1-800-722-8197
1-631-595-2217
Fax: 1-631-586-5899
WEB: WWW.CHALLEEELECTRONICS.COM

- ISO 9001:2000
- ISO 14001:2004
- ISO/TS 16949:2002



PRODUCT INFORMATION																														
PART #	CEM-C9745JAD462P2.54R		Revision																											
			0-2010																											
Omni-Directional Foil Electret Condenser Microphone																														
DESCRIPTION																														
Omni-Directional Foil Electret Microphone, 9.7 mm diameter and 4.5 mm high, Power Supply 5.0 V max, External Resistance Loading of 680 Ω, and sensitivity of -44 dB. Terminated with 2 solder points, Lead Free RoHS Compliant.																														
SPECIFICATIONS:																														
Direction	Omni Directional Foil Electret		Minimum Direction sensitivity																											
Operating Voltage Range	Vs= 1.0 Vdc ~ 10.0 Vdc		Power Supply (Vs)																											
Frequency Range	100 ~ 10,000 Hz.		Maximum Current																											
Sensitivity	-46 ± 2.0, (0 dB = 1V / Pa) at 1K Hz.		Minimum Sensitivity to Noise Ratio																											
Sensitivity Reduction	3.0 V to 2.0 V -3 dB		Maximum Input S.P.L.																											
Operating Temperature	-20°C to + 60°C		Storage Temperature																											
Loading Resistance (RL)	External, 680 Ω at Vs = 1.5 V, Max. 2,200 Ω		Built in Capacitors																											
Termination	PC Pins, 4.5 mm Long, 0.6 mm ø, 2.54 mm Spacing																													
Dimensions	Length / Diameter	Height	Housing Material																											
	9.7 mm ø	4.5 mm	Al-Mg Alloy.																											
Approximate Weight	0.7 grams	Options	Color																											
			RoHS, Lead Free																											
Reliability																														
Thermal Operating Cycle Test	250 hours continuous operation at Rated Power, at Maximum Rated Operating Temperature *																													
	250 hours continuous operation at Rated Power, at Minimum Rated Operating Temperature *																													
Thermal Storage Cycle Test	Parts are subjected to 250 hours storage at Maximum Rated Storage Temperatures *																													
	Parts are subjected to 250 hours storage at Minimum Rated Storage Temperatures *																													
Thermal Shock Test:	Parts are subjected to five (5) cycles of Minimum and Maximum Operating Temperature. Each cycle shall be set per diagram below and is three (3) hours long. *																													
Humidity Test	Parts are subjected to 240 Hours at +40°C±2°C, 90-95% RH *																													
Vibration Test	Parts are subjected to 2 Hours of at 1.5 mm with 10 to 55 Hz, vibration frequency to each of 3 perpendicular directions. *																													
Drop Test	Parts are dropped naturally from 1 meter height onto the surface of 40 mm wooden board, 2 axes (X,Y) directions, 3 times (8 times total). *																													
Reliability Test Performance *	Parts should conform to original performance within ±5 dB tested with Rated Power, after 3 hours of recovery period.																													
Termination Strength	Terminals should withstand a 1.0 Kg. pull test for up to 1 minute.																													
Life Test	At rated voltage in room temperature continuously for 1,000 hours																													
Warranty	For a period of one (1) year from date of shipping under normal operations conditions																													
Typical Frequency Response		Dimensions																												
																														
		<table border="1" style="font-size: small;"> <thead> <tr> <th>Frequency (Hz)</th> <th>Lower Limit (dB)</th> <th>Upper Limit (dB)</th> </tr> </thead> <tbody> <tr><td>50</td><td>-6</td><td>+3</td></tr> <tr><td>100</td><td>-3</td><td>+3</td></tr> <tr><td>800</td><td>-3</td><td>+3</td></tr> <tr><td>1000</td><td>0</td><td>0</td></tr> <tr><td>1200</td><td>-3</td><td>+3</td></tr> <tr><td>3000</td><td>-3</td><td>+6</td></tr> <tr><td>5000</td><td>-3</td><td>+6</td></tr> <tr><td>10000</td><td>-8</td><td>+6</td></tr> </tbody> </table>		Frequency (Hz)	Lower Limit (dB)	Upper Limit (dB)	50	-6	+3	100	-3	+3	800	-3	+3	1000	0	0	1200	-3	+3	3000	-3	+6	5000	-3	+6	10000	-8	+6
Frequency (Hz)	Lower Limit (dB)	Upper Limit (dB)																												
50	-6	+3																												
100	-3	+3																												
800	-3	+3																												
1000	0	0																												
1200	-3	+3																												
3000	-3	+6																												
5000	-3	+6																												
10000	-8	+6																												
		<p style="font-size: x-small;">Microphone Response Tolerance Window</p> <p style="font-size: x-small;">Units in: mm. Tolerance: ±0.3 mm</p>																												

The information contained herein is believed to be correct, but no guarantee or warranty, express or implied, with respect to accuracy, completeness or results is extended and no liability is assumed. Challenge Electronics reserves the right to make changes in any specification, data or material contained herein.

Copyright © 2010 Challenge Electronics

Note: This datasheet is derived from challengeelectronics.com.

B.5. Datasheet of the uni-directional microphone

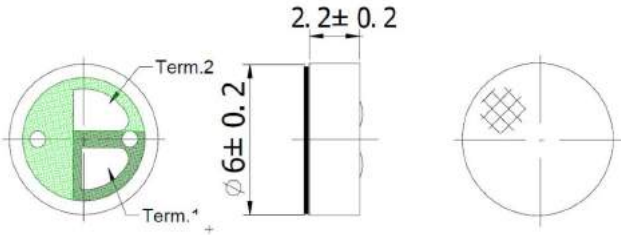


Professionally approved products.

**Datasheet
Condenser Microphone**

RS Stock number [724-3138](#)

Dimensions(mm):



SPECIFICATIONS	Electret Condenser Mircophone
Directivity	Uni directional
Standard Operating Voltage	2 V
Maximum Operating Voltage	10V
Maximum Current Consumption	0.5mA
Output Impedance (F=1KHz 1Pa)	< 2.2K Ohms
Frequency	50~16000Hz
Sensitivity (@F=1KHz, 0dB=1V/Pa)	-47±3dB
Signal to Noise Ratio (F=1KHz 1Pa) A weighted	>58dB
Positive Terminal	Term 1

Features:

- Uni-directional
- 6mm diameter
- Solder pads

RS, Professionally Approved Products, gives you professional quality parts across all products categories. Our range has been testified by engineers as giving comparable quality to that of the leading brands without paying a premium price.

Note: This datasheet is derived from nl.rs-online.com.

B.6. Datasheet of the sound level meter

Parameter	Value	Parameter	Value
Model	SLM 52N	Microphone model	MC-21
Main processing functions	weighing A & weighing C	Sensitivity	-37 dB
Total range (dB)	30 ~ 130	Frequency response (Hz)	31.5 ~ 8000
Warm-up time (min)	≤ 2	Max. input sound level (dB)	131
Output	AC output & DC output	Operating temperature (°C)	-10 ~ 50
Power	9V battery	Preamplifier model	AP-21

Note: This datasheet is extracted from the manual of sound level meter SLM 52N.

B.7. Datasheet of the accelerometer

ADXL337

SPECIFICATIONS

T_A = 25°C, V_S = 3 V, C_X = C_Y = C_Z = 0.1 μF, acceleration = 0 g, unless otherwise noted. All minimum and maximum specifications are guaranteed. Typical specifications are not guaranteed.

Table 1.

Parameter	Test Conditions/Comments	Min	Typ	Max	Unit
SENSOR INPUT					
Measurement Range	Each axis	±3	±3.6		g
Nonlinearity	% of full scale		±0.3		%
Package Alignment Error			±1		Degrees
Interaxis Alignment Error			±0.1		Degrees
Cross-Axis Sensitivity ¹			±1		%
SENSITIVITY (RATIOMETRIC)²					
Sensitivity at X _{OUT} , Y _{OUT} , Z _{OUT}	V _S = 3 V	270	300	330	mV/g
Sensitivity Change Due to Temperature ³	V _S = 3 V		±0.01		%/°C
0 g BIAS LEVEL (RATIOMETRIC)					
0 g Voltage at X _{OUT} , Y _{OUT}	V _S = 3 V	1.35	1.5	1.65	V
0 g Voltage at Z _{OUT}	V _S = 3 V	1.2	1.5	1.8	V
0 g Offset vs. Temperature X _{OUT} , Y _{OUT}			±1.1		mg/°C
0 g Offset vs. Temperature Z _{OUT}			±1.6		mg/°C
NOISE PERFORMANCE					
Noise Density X _{OUT} , Y _{OUT}			175		μg/√Hz rms
Noise Density Z _{OUT}			300		μg/√Hz rms
FREQUENCY RESPONSE⁴					
Bandwidth X _{OUT} , Y _{OUT} ⁵	No external filter		1600		Hz
Bandwidth Z _{OUT} ⁵	No external filter		550		Hz
R _{FILT} Tolerance			32 ± 15%		kΩ
Sensor Resonant Frequency			5.5		kHz
SELF TEST⁶					
Logic Input Low			0.6		V
Logic Input High			2.4		V
ST Actuation Current			60		μA
Output Change at X _{OUT}	Self test 0 to 1	-150	-325	-600	mV
Output Change at Y _{OUT}	Self test 0 to 1	+150	+325	+600	mV
Output Change at Z _{OUT}	Self test 0 to 1	+150	+550	+1000	mV
OUTPUT AMPLIFIER					
Output Swing Low	No load		0.1		V
Output Swing High	No load		2.8		V
POWER SUPPLY					
Operating Voltage Range ⁷		1.8	3.0	3.6	V
Supply Current	V _S = 3 V		300		μA
Turn-On Time ⁸	No external filter		1		ms
TEMPERATURE					
Operating Temperature Range		-40		+85	°C

¹ Defined as coupling between any two axes.

² Sensitivity is essentially ratiometric to V_S.

³ Defined as the output change from ambient-to-maximum temperature or ambient-to-minimum temperature.

⁴ Actual frequency response controlled by user-supplied external filter capacitors (C_S, C_Y, C_Z).

⁵ Bandwidth with external capacitors = 1/(2 × π × 32 kΩ × C). For C_S, C_Y = 0.003 μF, bandwidth = 1.6 kHz. For C_Z = 0.01 μF, bandwidth = 500 Hz. For C_X, C_Y, C_Z = 10 μF, bandwidth = 0.5 Hz.

⁶ Self test response changes cubically with V_S.

⁷ Tested at 3.0 V and guaranteed by design only (not tested) to work over the full range from 1.8 V to 3.6 V.

⁸ Turn-on time is dependent on C_S, C_Y, C_Z and is approximately 160 × (C_S or C_Y or C_Z) + 1, where C_S, C_Y, and C_Z are in μF and the resulting turn-on time is in ms.

Note: This datasheet is derived from sparkfun.com.

Appendix C: The verification test

For the verification test, an idler roll is prepared by gluing a rubber strip (thickness of 5 mm) on the shell. After that it is installed on the test rig (Figure C.1). The rubber strip will cause significant vibration when it contacts the belt during the roll's running. The verification test is conducted with a belt velocity of 1.8 m/s, and the load on the roll is 108 N. The data acquisition is conducted with a sampling frequency of 100 Hz and a duration of 10 seconds.

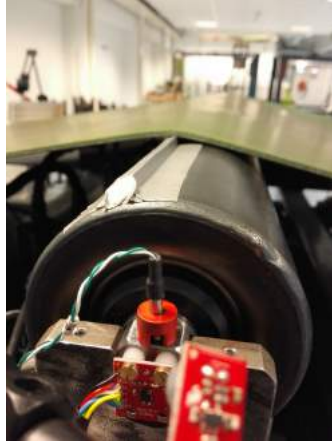


Figure C.1: The verification test for the FFT program.

The verification of the FFT program is achieved by comparing the peak frequencies found in the frequency plots from the FFT program (data acquired from the accelerometer at ShL1) with the induced vibration frequency by the rubber strip. With the given belt velocity, the induced vibration frequency f_{rot} can be calculated as:

$$f_{rot} = \frac{v}{\pi d_0} = 5.3 \text{ Hz} \quad (\text{C.1})$$

in which v is the belt velocity, d_0 is the outer diameter of the shell (108 mm in this case).

In addition, the harmonics of the induced vibration frequency less than 50 Hz are as follows: 10.6 Hz, 15.9 Hz, 21.2 Hz, 26.5 Hz, 31.8 Hz, 37.1 Hz, 42.4 Hz, 47.7 Hz.

Figure C.2 shows the energy spectra of the vibration in the frequency domain after applying the FFT program. Figure C.2 (a) is the spectrum of the horizontal vibration, while (b) is the spectrum of the vertical vibration. From the energy spectra, it can be clearly observed that high peaks of energy is located at the induced vibration frequency (5.3 Hz) and its harmonics.

In addition, it can be seen that the energy at 37.1 Hz in Figure C.3 (a) is much higher than the energy at the induced vibration frequency of 5.3 Hz. To clarify the reason, the eigenfrequency of the roll and the idler frame as an aggregate structure is explored. Figure C.3 (a) and (b) show the frequency response of the roll in the horizontal and vertical direction respectively. While Figure C.3 (c) is a typical energy plot of the vibration in the horizontal direction at the shaft end ShL2 during the defect roll tests with a belt velocity of 1.8 m/s. From Figure C.3 (a) and (b), the eigenfrequency of the aggregate structure is considered

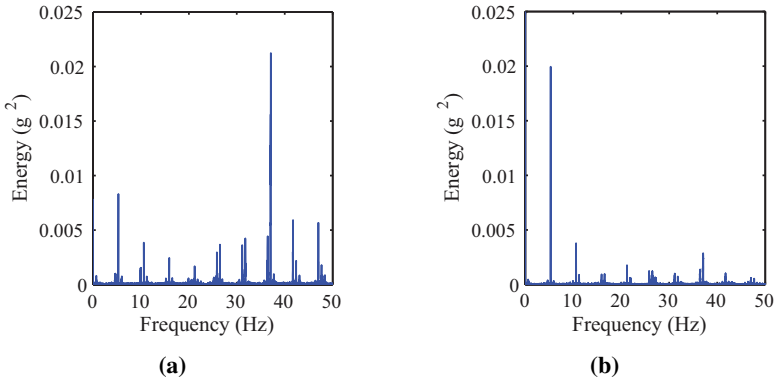


Figure C.2: Energy spectra of the vibration in frequency domain, a) spectrum of the horizontal (X) vibration, and b) spectrum of the vertical (Y) vibration.

to be 39.2 Hz as shown the peaks in the two plots. This explains why the energy at 37.1 Hz is even higher than the energy at 5.3 Hz in Figure C.3 (a), as well as the peak at 37 Hz in Figure B.3 (c), which are caused by the resonance. The difference between the 37 Hz and 39 Hz can be attributed to the influence of the running conveyor belt.

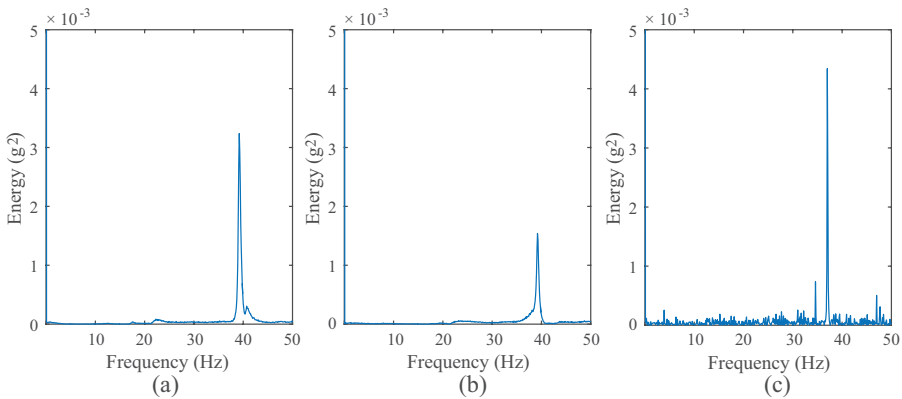


Figure C.3: Energy spectra of the vibration in frequency domain, a) spectrum of the vibration in the horizontal direction at the shaft end ShL2 after a shock hit on the middle of the roll in the horizontal direction, b) spectrum of the vibration in the horizontal direction at the shaft end ShL2 after a shock hit on the middle of the roll in the vertical direction, and c) typical spectrum of the vibration in the horizontal direction at the shaft end ShL2 during defect roll tests while the roll without the rubber strip.

Appendix D: The emissivity test

To investigate the influence of the emissivity of the shaft end on the measurements of different sensors, tests are conducted to measure the temperature of purposely heated shaft ends (Figure D.1). The shaft is heated up using a heat gun (model Steinel HL 1800E) for 120 minutes to reach a stable temperature. There are three treatments of the shaft ends, the first one is untreated which is commonly seen polished shaft end in new idler rolls, the second one is painted with black heat resistant matte finish paint, the third one is immersed into salty water (5 percent salt) for five days and is then exposed in air for another five days to grow rust on the surface.

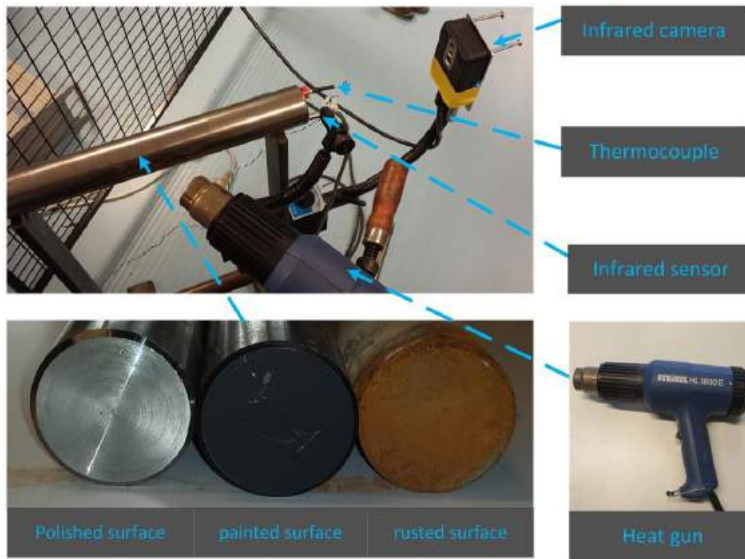
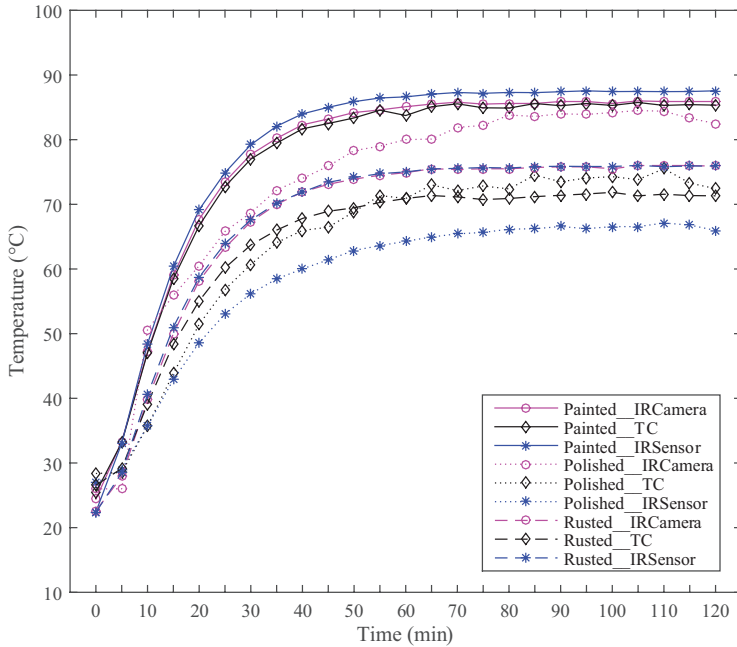


Figure D.1: Test setup. The top picture shows the overview of the test setup, the lower left picture shows the treatment of the shaft ends, and the lower right picture shows the heat gun used in the tests.

Figure D.2 illustrates the temperature evolutions of the painted, polished and rusted shaft ends which are derived from the measurements of the infrared sensor, the infrared camera, and the thermocouple. It can be seen that all shaft ends present a regressive pattern of temperature evolution. Furthermore, for the infrared sensor, the measured temperature of the painted shaft end is the highest, while the temperature of the polished shaft end is the lowest. The reason can be attributed to the emissivity. The painted shaft end has the highest emissivity (around 1) while the polished shaft end has the lowest emissivity (about 0.1 to 0.35). The rusted shaft end is considered to an emissivity between 0.7 and 0.9 (Raytek Corporation, 1999). The emissivity factor for the applied infrared sensor is fixed as 0.9. Therefore, the measurements of the polished shaft end have big error.

For the infrared camera, the measurements of the painted shaft end have very good results. On the other hand, the measurements of the polished shaft end overestimate the temperature even though the emissivity factor is set as 0.3. During the experiments, it is recognized that a challenge exists to find a proper emissivity factor for the measurements of the infrared camera because the emissivity factor is not only surface finish dependent



Appendix D.2: The temperature evolution of the painted, polished and rusted shaft ends under heating for 120 minutes, derived from the measurements of the infrared sensor (IRSensor), the infrared camera (IRCamera), and the thermocouple (TC).

but temperature dependent.

For the thermocouple, the measured temperature of the painted and polished shaft ends is considered quite good while that of the rusted shaft end is lower than the true value. The reason may be attributed to the fact that the thermocouple cannot contact the surface tightly due to the rust on the surface.

Table D.1: Summary of applicability of temperature sensors.

	Painted shaft end	Polished shaft end	Rusted shaft end
thermocouple	√	√	
infrared sensor	√		√
infrared camera	√	√	√

Table D.1 summarizes the applicability of the three types of temperature sensors for different shaft ends. It can be seen that the three sensors are all applicable to measure the painted shaft end.

GLOSSARY

List of symbols and notations.

a	distance between a roll bearing and a shaft bracket [m]
a_1, a_2, a_3	factors used to calculate the lifetime of bearings
b	loaded belt length [m]
c	distance between two roll bearings [m]
d	diameter of the shaft of an idler roll [m]
d_0	diameter of the shell of an idler roll [m]
f_{bi}	inner race defect frequency [Hz]
f_{bo}	outer race defect frequency [Hz]
f_d	dynamic factor [-]
f_{er}	rolling element defect frequency [Hz]
f_{rot}	rotating frequency of bearing [Hz]
g	acceleration of gravity [m/s^2]
l	idler spacing [m]
l_1	length of bulk material along the wing belt section [m]
l_M	length of the shell of the center roll [m]
l_{sag}	belt sag [m]
m	belt width [m]
m'_{belt}	mass of belt per unit length [kg/m]
m'_{bulk}	mass of bulk material per unit length [kg/m]
n	rotational speed of a bearing [rpm]
P	principle stress [N/m^2]
q	load on the shell of an idler roll [N/m]
q_a	active principle stress [N/m^2]
r	radii of Mohr circles [N/m^2]
s	thickness of the shell of an idler roll [m]
v	belt velocity [m/s]
y_{shell}, y_{shaft}	angular deflections of the shell and shaft [-]
z	depth of bulk material element from surface [m]

A_s, A_{th}	theoretical area of the filling cross section according to CEMA and DIN 22101 [m^2]
BD	diameter of bearing rolling element [m]
C	dynamic load rating of bearings [N]
E	Young's modulus [GPa]
F_{bulk}	bulk load [N]
$F_{G,belt}, F_{G,cbelt}$	weight of wing belt section and center belt section [N]
$F_{max,a}, F_{max,p}$	maximum active and passive thrust force on a retaining structure [N]
$F_{NG,bulk,a}, F_{NG,bulk,p}$	normal forces on the belt in active and passive stress states [N]
$F_{NA,bulk,a}, F_{NA,bulk,p}$	shear forces on the belt in active and passive stress states [N]
F_{NG}, F'_{NG}	radial force on an idler roll [N]
$F_{NG,c}$	radial force on the centre roll [N]
$F_{NG,w}$	radial force on the wing belt section [N]
$F_{NA,w}$	axial force on the wing belt section [N]
I_y	moment of inertia with respect to y-axis [m^4]
L	achieved service time of bearings [hour]
L_{10}	rating lifetime of a population of bearings [hour]
K_a, K_p	coefficients in active and passive stress states [-]
K_s	belt sag ratio [-]
K_1	lump adjustment factor [-]
H	height of a soil mass [m]
P	equivalent load on a bearing [N]
PD	diameter of the center of bearing cage [m]
P_{design}	load on roll bearings corresponding to design capacity of a conveyor [N]
P_i	load on roll bearings corresponding to i th level of throughput [N]
P_m	load on roll bearings corresponding to design capacity of a conveyor [N]
$P_{NA,L1}$	axial force on the wing roll [N]
$P_{NG,L1}, P_{NG,L2}$	radial forces on the wing roll bearings [N]
$P_{NG,c}$	radial force on the center roll bearing [N]
Q_i	i th level of throughput [t/h]
Q_{design}	design capacity of a belt conveyor [t/h]
R	the reliability [-]
T	belt tension [N]
T_i	operational time of the conveyor corresponding to i th level of throughput [hour]
X_{RMS}	RMS level [g]
α	trough angle of the idler configuration or the retaining wall [$^\circ$]
α_1, α_2	parameters
β	conveyor surcharge angle of bulk material or surface slope angle of soil [$^\circ$]
γ	aggregation factor [-]

γ_1	aggregation factor [-]
δ	strength mobilized on the stress discontinuity [-]
θ, θ_o	rotations of the major principal stress [°]
θ_a, θ_p	rotations of major principal stresses in active and passive stress states [°]
ρ	density of bulk material [kg/m ³]
$\sigma, \sigma_{b,a}$	normal stress on bulk element [N/m ²]
$\sigma_{oc1}, \sigma_{oc2}$	average effective stresses in active stress state [N/m ²]
$\sigma_{w,a}, \sigma_{w,p}$	normal stresses in active and passive stress states in zone 2 [N/m ²]
τ	shear stress on bulk element [N/m ²]
$\tau_{w,a}$	shear stress in active stress state in zone 2 [N/m ²]
φ	angle between the horizon and the tangent to the belt [°]
φ_B	idler roll service factor [-]
φ_{Betr}	factor [-]
$\varphi_{filling}$	effective filling ratio [-]
φ_i	internal friction angle of bulk material [°]
φ_{St}	Factor [-]
φ_w	wall friction angle between the belt and bulk material [°]
ω	angle of slope [°]
$\omega_{a,crit}, \omega_{p,crit}$	critical inclination angle for active and passive failure planes [°]
ψ	idler roll service factor [-]
$\Delta, \Delta_1, \Delta_2, \Delta_3, \Delta_4$	angles in Mohr circle [-]
$\varepsilon, \varepsilon_1$	error [-]

List of abbreviations.

CBS	center belt section
CEMA	Conveyor Equipment Manufacturers Association
FFT	fast Fourier transform
KH model	the model developed by Krause and Hettler (1974)
SD model	the model developed in this research
WBS	wing belt section
LWBS	left wing belt section
RWBS	right wing belt section

SUMMARY

Belt conveyor systems are widely utilized for the continuous transport of bulk materials over varying distances. The reliability of belt conveyor systems is of major concern for the operators. The financial loss due to the downtime of belt conveyor systems can be very high, considering the loss of revenue from material conveying and shutdowns of subsequent material processing facilities. The reliability of a belt conveyor can be considered as an integrated reliability of its main components, including a belt, pulleys, a drive unit, and idler rolls etc.

This thesis focuses on how to improve the reliability of belt conveyor systems with respect to idler rolls. The performance of idler rolls has a large impact on the reliable operation of belt conveyor systems. The malfunction of idler rolls may lead to extra energy consumption and noise pollution. More seriously, idler roll failures can induce serious damages to conveyor belts, which builds up downtime and maintenance cost of belt conveyor systems.

In order to tackle the problem, this research aims to improve the predictability of idler roll failures. The prediction of idler roll failures will enable the implementation of predictive maintenance for idler rolls, which can largely prevent idler rolls from running into catastrophic failures. Theoretical and experimental research are conducted to improve the predictability of idler roll bearing failures.

Theoretical approaches to predict the reliability of bearings are available. To apply such an approach, it is essential to determine the load on roll bearings accurately. With a consideration that an adequate method to calculate the load on idler roll bearings due to conveyed bulk material and the belt is still missing, this research develops an analytical approach for this purpose. Within the approach, a new lower bound model for the calculation of the load on a conveyor belt due to bulk materials is developed and verified. By aggregating the developed lower bound model with a widely recognized upper bound model, the analytical approach is considered to determine the load on idler roll bearings more accurately.

Experimental study is also conducted to advance the measurement of the load on a conveyor belt due to bulk materials by using a tactile pressure sensor. Compared to conventional load cells or strain gauges, tactile pressure sensors enable direct measurements of the pressure distribution on a conveyor belt, which is important for the verification of theoretical models and in-depth understanding of the interaction between bulk materials and a belt. From the experimental study, it is recognized that the tactile pressure sensor can provide qualitative insight into the bulk load distribution for scientific purpose.

However, it is still a challenge to provide very accurate measurement of the pressure on a conveyor belt in running state.

In addition, experimental study is carried out to investigate how to detect idler roll failures by applying condition monitoring techniques. For this purpose, a test rig based on a full scale belt conveyor is designed. Different types of defects and damages are induced to idler rolls to simulate different levels of failure. A variety of sensors, including temperature sensors, acoustic sensors and accelerometers are applied during the experiments to monitor the idler rolls. It is found that it is possible to detect idler roll failures by monitoring parameters such as the temperature, vibration and acoustic emission with certain features.

With a consideration of limitations of the theoretical approach and the condition monitoring techniques, an integrated maintenance decision making framework which combines the two approaches is also proposed in this research. The framework incorporates the failure rates of idler rolls derived from both the theoretical approach and condition monitoring data. In this way, a more accurate decision making algorithm is introduced into predictive maintenance for idler rolls.

In summary, the predictability of idler roll failures is largely enhanced through this research.

SAMENVATTING

Bandtransporteurs worden veel gebruikt in het continue transport van bulkgoed. Het betrouwbaar functioneren van een bandtransportsysteem is van groot belang voor de gebruiker. De financiële gevolgen van het uitvallen van een transportsysteem kunnen erg groot zijn door het verlies van inkomsten uit het transport en de kosten van het uitvallen van faciliteiten die door op het transportsysteem zijn aangesloten. De betrouwbaarheid van een bandtransportsysteem kan worden beschouwd als de overall betrouwbaarheid van de onderdelen, zoals de band, de trommels, de aandrijving, de rollen, enz.

Doel van dit onderzoek is het verhogen van de betrouwbaarheid van bandtransportsystemen, met de nadruk op de draagrollen. Het functioneren van de rollen heeft grote invloed op het betrouwbaar functioneren van het gehele systeem. Defecten aan de rollen kunnen een verhoogd energiegebruik of een verhoogde geluidsproductie tot gevolg hebben. In ernstige gevallen kan er schade ontstaan aan de band zelf, en daardoor stilstand van de band en reparatiekosten.

Dit onderzoek is gericht op een verbetering van de voorspelbaarheid van de defecten aan draagrollen. Door een betere voorspelling van de defecten aan rollen kan voorspellend preventief onderhoud aan de rollen worden gerealiseerd. Fatale fouten aan de rollen kunnen daarmee worden voorkomen en het gehele bandtransportsysteem kan betrouwbaar blijven functioneren. Er is theoretisch en experimenteel onderzoek uitgevoerd ter verbetering van de voorspelbaarheid van fouten aan de lagers van de rollen.

Er zijn theoretische modellen beschikbaar voor de voorspelling van de resterende gebruiksduur van lagers. Voor het toepassen van die modellen is het nodig om de belasting van de rol nauwkeurig te bepalen. Omdat er een geschikte methode ontbrak voor de berekening van de belasting van de lagers door het getransporteerde materiaal en de band, is in dit onderzoek hiervoor een analytische methode ontwikkeld. Als onderdeel van deze methode is een nieuw model voor de berekening van een ondergrens van de belasting van de transportband ten gevolge van het getransporteerde materiaal ontwikkeld en geverifieerd. Door combinatie van het ontwikkelde model voor de berekening van een ondergrens met een algemeen erkend model voor de berekening van de bovengrens kan de belasting op de lagers nauwkeurig worden bepaald.

Er is experimenteel onderzoek gedaan ter verbetering van de bepaling van de belasting van de transportband ten gevolge van het getransporteerde materiaal met behulp van druksensoren. Vergeleken met conventionele load cells of rekstrookjes, is het met druksensoren mogelijk om directe metingen te doen aan de drukverdeling op de band. Dit is belangrijk voor de verificatie van theoretische modellen en voor een goed begrip van

de interactie tussen het getransporteerde materiaal en de band. Uit het experimentele onderzoek blijkt dat de druksensoren een goed inzicht kunnen geven voor het theoretisch onderzoek naar de belasting van de band. Maar het blijft een uitdaging om nauwkeurige metingen te doen aan de belasting van een bewegende band.

Er is tevens experimenteel onderzoek gedaan hoe defecten aan rollen kunnen worden gesignaleerd met behulp van condition monitoring technieken. Hiervoor is een testopstelling op ware grootte gemaakt. Er zijn aan de rollen verschillende soorten beschadigingen aangebracht voor het nabootsen van zowel aanloopdefecten als fatale defecten. Bij het experiment zijn verschillende soorten sensoren, zoals tempertuursensoren, akoestische sensoren en versnellingsmeters, gebruikt om metingen aan de rollen te doen. Het blijkt mogelijk om defecten aan rollen te signaleren door het meten van grootheden zoals de temperatuur, trillingen en geproduceerd geluid.

Omdat zowel de theoretische benadering als de condition monitoring technieken beperkingen hebben, wordt in dit onderzoek een geïntegreerd onderhoudskader voorgesteld waarin de beide benaderingen worden gecombineerd. In deze geïntegreerde benadering worden de faalsnelheden van de rollen uit de theoretische benadering gecombineerd met de gegevens van de condition monitoring. Hiermee wordt een nauwkeuriger beslissingsmethode geïntroduceerd voor het voorspellend preventief onderhoud van de rollen.

Samenvattend: de voorspelbaarheid van defecten aan de rollen is door dit onderzoek belangrijk verbeterd.

CURRICULUM VITAE

Xiangwei LIU

Xiangwei Liu was born on August 2nd, 1985 in Rizhao, P.R. China. In 2008 he received his BSc degree in Mechanical Engineering at Wuhan University of Technology, Wuhan, P.R. China. From 2008 to 2010, he worked at Wuhan University of Technology as a teacher. In 2012, he obtained his MSc degree in Mechanical Engineering at Wuhan University of Technology.

In 2012 Xiangwei started his Ph.D. at Section of Transport Engineering & Logistics at Delft University of Technology, the Netherlands. His research project is about intelligent monitoring, diagnosis and maintenance of large-scale material conveying systems. In this project he focused on belt conveyor systems and particularly idler rolls. His research interest includes belt conveyor technology, bulk material modeling and engineering.

Publications

1. X. Liu, Y. Pang, and G. Lodewijks. Theoretical and experimental determination of the pressure distribution on a loaded conveyor belt. *Measurement*, 77:307–316, 2016. doi: 10.1016/j.measurement.2015.08.041.
2. X. Liu, Y. Pang, and G. Lodewijks. A stress discontinuity approach to model the stress profile on a loaded conveyor belt. *Powder Technology*, 273:102–110, 2015. doi: 10.1016/j.powtec.2014.12.040.
3. X. Liu, Y. Pang, G. Lodewijks, C.A. Wheeler, and B. Beh. Quantification of the pressure distribution on a loaded conveyor belt using a tactile pressure sensor. In *Proceedings of the XXI International Conference on Material Handling, Constructions and Logistics (MHCL)*, Vienna, Austria, 2015.
4. X. Liu, Y. Pang, G. Lodewijks, C.A. Wheeler, and B. Beh. Assessment of the dynamic pressure measurement on a loaded conveyor belt using a tactile pressure sensor. In *Proceedings of the XXI International Conference on Material Handling, Constructions and Logistics (MHCL)*, Vienna, Austria, 2015.

5. X. Liu, G. Lodewijks, and Y. Pang. Intelligent maintenance of large-scale belt conveyor idler rolls: State-of-the-art and opportunities. In Proceedings of the 1st Symposium on Automated Systems and Technologies, pages 95–103, Hannover, Germany, 2014.
6. X. Liu, Y. Pang, and G. Lodewijks. A new analytical model of load calculation for trough idler rolls stress discontinuity model for conveyor idler roll load calculation. In Proceedings of the MHEA 2014 Bulk Conference, North Lincolnshire, UK, 2014.

TRAIL Thesis Series

The following list contains the most recent dissertations in the TRAIL Thesis Series. For a complete overview of more than 150 titles see the TRAIL website: www.rsTRAIL.nl.

The TRAIL Thesis Series is a series of the Netherlands TRAIL Research School on transport, infrastructure and logistics.

Liu, X., *Prediction of Belt Conveyor Idler Performance*, T2016/14, September 2016, TRAIL Thesis Series, the Netherlands

Gaast, J.P. van der, *Stochastic Models for Order Picking Systems*, T2016/13, September 2016, TRAIL Thesis Series, the Netherlands

Wagenaar, J.C., *Practice Oriented Algorithmic Disruption Management in Passenger Railways*, T2016/12, September 2016, TRAIL Thesis Series, the Netherlands

Psarra, I., *A Bounded Rationality Model of Short and Long-Term Dynamics of Activity-Travel Behavior*, T2016/11, June 2016, TRAIL Thesis Series, the Netherlands

Ma, Y., *The Use of Advanced Transportation Monitoring Data for Official Statistics*, T2016/10, June 2016, TRAIL Thesis Series, the Netherlands

Li, L., *Coordinated Model Predictive Control of Synchromodal Freight Transport Systems*, T2016/9, June 2016, TRAIL Thesis Series, the Netherlands

Vonk Noordegraaf, D.M., *Road Pricing Policy Implementation*, T2016/8, June 2016, TRAIL Thesis Series, the Netherlands

Liu, S., *Modeling, Robust and Distributed Model Predictive Control for Freeway Networks*, T2016/7, May 2016, TRAIL Thesis Series, the Netherlands

Calvert, S.C., *Stochastic Macroscopic Analysis and Modelling for Traffic Management*, T2016/6, May 2016, TRAIL Thesis Series, the Netherlands

Sparing, D., *Reliable Timetable Design for Railways and Connecting Public Transport Services*, T2016/5, May 2016, TRAIL Thesis Series, the Netherlands

Rasouli, S., *Uncertainty in Modeling Activity-Travel Demand in Complex Urban Systems*, T2016/4, March 2016, TRAIL Thesis Series, the Netherlands

Vries, J. de, *Behavioral Operations in Logistics*, T2016/3, February 2016, TRAIL Thesis Series, the Netherlands

Goñi-Ros, B., *Traffic Flow at Sags: Theory, Modeling and Control*, T2016/2, March 2016, TRAIL Thesis Series, the Netherlands

Khademi, E., *Effects of Pricing Strategies on Dynamic Repertoires of Activity-Travel Behaviour*, T2016/1, February 2016, TRAIL Thesis Series, the Netherlands

Cong, Z., *Efficient Optimization Methods for Freeway Management and Control*, T2015/17, November 2015, TRAIL Thesis Series, the Netherlands

Kersbergen, B., *Modeling and Control of Switching Max-Plus-Linear Systems: Rescheduling of railway traffic and changing gaits in legged locomotion*, T2015/16, October 2015, TRAIL Thesis Series, the Netherlands

Brands, T., *Multi-Objective Optimisation of Multimodal Passenger Transportation Networks*, T2015/15, October 2015, TRAIL Thesis Series, the Netherlands

Ardıç, Ö., *Road Pricing Policy Process: The interplay between policy actors, the media and public*, T2015/14, September 2015, TRAIL Thesis Series, the Netherlands

Xin, J., *Control and Coordination for Automated Container Terminals*, T2015/13, September 2015, TRAIL Thesis Series, the Netherlands

Anand, N., *An Agent Based Modelling Approach for Multi-Stakeholder Analysis of City Logistics Solutions*, T2015/12, September 2015, TRAIL Thesis Series, the Netherlands

Hurk, E. van der, *Passengers, Information, and Disruptions*, T2015/11, June 2015, TRAIL Thesis Series, the Netherlands

Davydenko, I., *Logistics Chains in Freight Transport Modelling*, T2015/10, May 2015, TRAIL Thesis Series, the Netherlands

Schakel, W., *Development, Simulation and Evaluation of In-car Advice on Headway, Speed and Lane*, T2015/9, May 2015, TRAIL Thesis Series, the Netherlands

Dorsser, J.C.M. van, *Very Long Term Development of the Dutch Inland Waterway Transport System: Policy analysis, transport projections, shipping scenarios, and a new perspective on economic growth and future discounting*, T2015/8, May 2015, TRAIL Thesis Series, the Netherlands

Hajiahmadi, M., *Optimal and Robust Switching Control Strategies: Theory, and applications in traffic management*, T2015/7, April 2015, TRAIL Thesis Series, the Netherlands

Wang, Y., *On-line Distributed Prediction and Control for a Large-scale Traffic Network*, T2015/6, March 2015, TRAIL Thesis Series, the Netherlands

Vreeswijk, J.D., *The Dynamics of User Perception, Decision Making and Route Choice*, T2015/5, February 2015, TRAIL Thesis Series, the Netherlands

Lu, R., *The Effects of Information and Communication Technologies on Accessibility*, T2015/4, February 2015, TRAIL Thesis Series, the Netherlands

Ramos, G. de, *Dynamic Route Choice Modelling of the Effects of Travel Information using RP Data*, T2015/3, February 2015, TRAIL Thesis Series, the Netherlands